ABSTRACT

Title of Dissertation:	VISUALIZING DYNAMICS DURING CHEMICAL REACTION DRIVEN NON – EQUILIBRIUM COLLOIDAL AND NANOPARTICLE ASSEMBLY
	Thilini Dissanayake Appuhamillage Doctor of Philosophy, 2023
Dissertation directed by:	Professor Taylor J. Woehl Department of Chemical and Biomolecular Engineering.

Biological nano and microstructures exist far from thermodynamic equilibrium by continuous consumption of energy that allows them to reconfigure or adapt to changes in the local environment. Utilization of these non-equilibrium structure formation processes in synthetic colloidal particle and nanoparticle (NP) systems is expected to enable unprecedented control over the dynamics of synthetic active soft materials and systems that are beyond the reach of equilibrium self – assembly. In this work we adapted two non – equilibrium structure formation processes observed in biological systems, dissipative assembly and reaction diffusion instability, to generate dynamic colloidal assemblies and self-organized patterns of nanoparticles.

First, we investigated how the surface chemistry and interparticle interactions between colloids changed during chemical reaction driven dissipative assembly of polystyrene colloids.

A key result was the first, time dependent measurements of the dynamic colloid surface chemistry (surface charge and hydrophobicity) during dissipative assembly. Importantly, we demonstrated that thermodynamic interparticle interaction models typically used for equilibrium self-assembly are effective in describing fuel driven colloid assembly far from equilibrium. The interparticle interaction models demonstrated that electrostatic interactions controlled the concentration of particle aggregates while the strength of hydrophobic interactions determined whether colloids underwent irreversible aggregation or dissipative assembly.

Next, using a correlative fluorescence microscopy and liquid phase transmission electron microscopy (LPTEM) method, we demonstrated that aminated polymer capping ligands on metal NPs undergo crosslinking and chain scission reactions as a result of formation of hydroxyl and hydrogen radicals due to electron beam induced radiolysis of water. We demonstrated that a hydroxyl radical scavenger can minimize the electron beam induced reactions in the polymers. Based on this fundamental knowledge, we introduced an instability to an initially homogenous gold NP decorated aminopolysiloxane thin film immersed in water by scanning TEM beam. Radiolysis driven polymer radical reactions of polysiloxane coupled with diffusion of radicals, polymers, and NPs caused the polymer and NP to self-organize into repeating spatial patterns, *i.e.*, Turing patterns, with no template or specific interparticle interactions. Spots, strings and labyrinth patterns that closely resembled Turing skin pigmentation patterns on various animals were obtained by tuning the chemistry of the system. A series of systematic experiments identified that hydroxyl radicals and NPs as critical species driving the formation of the NP patterns. We expect this work could be used as a model system in establishing design rules for nanoscale pattern formation by reaction – diffusion instability.

VISUALIZING DYNAMICS DURING CHEMICAL REACTION DRIVEN NON – EQUILIBRIUM COLLOIDAL AND NANOPARTICLE ASSEMBLY

by

Thilini Umesha Dissanayake Appuhamillage

Dissertation submitted to the Faculty of the Graduate School of the
University of Maryland, College Park, in partial fulfillment
of the requirements for the degree of
Doctor of Philosophy
2023

Advisory Committee:
Professor Taylor J Woehl, Chair
Professor Lourdes Salamanca-Riba
Professor Po-Yen Chen
Professor Gregg Duncan
Professor Juan Carlos Vega-Vila

Dedication

To my family,

who wished I would become a medical doctor.

Sorry, this is the only doctor you will ever get from me.

and

To all the graduate students who keep going when feeling like giving up

many times over.

Acknowledgements

I would like to thank several people who have supported me in my PhD journey. First, I would like to thank my PhD advisor Professor Taylor Woehl for his guidance throughout my PhD and introducing me to the microscopy world. I would like to thank all my present and past lab group members for their help working in the lab. I thank Dr. Mei Wang for showing me how to use the liquid cell holder and the help with troubleshooting problems. I fondly remember the support given by Dr. Shakiba Nifarjam and Medha Rath and thank them for being there for me in some of the hardest times. I would like to express my gratitude to Dr. Sz-Chian Liou for helping me at the AIM lab during TEM experiments. The best teacher I have met in a classroom in UMD, Professor Lourdes Salamanca-Riba, thank you for the in – depth knowledge into microscopy and for excellent training in how to use the TEM. My sincere gratitude goes to my dissertation committee members, Professor Po-Yen Chen, Professor Gregg Duncan and Professor Juan Carlos Vega-Vila. I fondly remember my friends here at UMD Nadee, Anuththara, Sajani, Lasitha, Dilhara, Rishvi, Dushyanthi and Yashish and thank you for making it easier living so far away from home. I would like to thank my cousin Vindya for inspiring me to pursue a PhD and for all the long talks and insights. Finally, I would like to thank my amma and thaththa for providing me with a quality education without which I would not be here and also for all the love, all the support even from thousands of miles away.

Table of Contents

List of Figures

List of Abbreviations

DLVO	Derjaguin, Landau, Verwey and Overbeek
RDI	Reaction Diffusion Instability
LPTEM	Liquid Phase Transmission Electron Microscopy
TEM	Transmission Electron Microscopy
STEM	Scanning Transmission Electron Microscopy
EDC	1-Ethyl-3-(3-dimethylaminopropyl)carbodiimide
NHS	N–Hydroxysuccinimide
MES	2–(N–morpholino)ethanesulfonic acid
DI	Deionized
BPEI	Branched Polyethylenimine
FM	Fluorescence Microscopy
APTES	(3-Aminopropyl)triethoxysilane

Chapter 1. Introduction

1.1 Assembly of colloidal particles

Hierarchical assembly of particles in microscale and nanoscale has decades expanding history in bottom – up approach to fabrication. Particles of different shapes and sizes made with various materials having different surface chemistries have been manipulated to form larger entities.[1] Assembly of colloidal particles has enabled synthesizing nanoscale structures which are smaller than the lowest resolution that could be reached by top – down fabrication methods.[2] While top – down fabrication requires expensive instruments and clean room facilities, the spontaneous assembly of colloidal particles requires minimal resources most of the time. The serial nature of top – down fabrication methods is avoided in colloidal assembly where large number of components are handled at the same time.[2] Also, complex materials could be realized by hierarchical assembly of colloidal particles. In the top – down approach bulk material is reconfigured into desired structures. But colloidal assemblies present unique magnetic, photonic and electric properties that is not available to their discrete units or in bulk material phase due to plasmon coupling, exciton coupling and magnetic coupling in their assembled state.[3] The plasmonic, electrical and magnetic properties could be tuned by simply varying the spatial distance between particles in the structure. Also, the ability to manipulate oriented attachment between anisotropic colloidal particles has been useful in modulating the optical properties of the ensembles.[4] Based on different properties and functions, colloidal particles assembly has been applied in a diverse range of fields including nanoelectronics,[5,6] optics,[7,8] sensors,[9,10] catalysis,[11,12] nanomedicine and drug delivery.[13,14]

Self-assembly and directed assembly are the widely used strategies for constructing structures from colloidal particles. Colloidal particles spontaneously associate into structures during self-assembly through local specific interparticle interactions. In directed assembly, colloidal particles are arranged into ordered structures by assistance of an external stimulus, such as light, electric field, magnetic field, and solvent evaporation, thereby guiding the process to achieve the desired results.[15] The goal of self – assembly is to engineer the interparticle interactions between particles as well as the assembly kinetics to allow the system to minimize the free energy and reach thermodynamic equilibrium to produce the desired static structures.[16] In directed assembly, external fields induced forces on colloids that modify the energy landscape and direct particles to assemble into a desired configuration.[17] Equilibrium self-assembly is reversible, with particles dynamically transitioning between an assembled and discrete state due to thermal fluctuations. At equilibrium, the concentration, size, and structure of the assembled material does not change with time unless the local environment (e.g., temperature, pH, ionic strength) is changed. However, in living systems such as cells most of the structures and undergo continuous spatial and temporal dynamics and can reconfigure their structure in response to changes in their environment through an intricate system of reaction networks.[18] To achieve this purpose, these structures exist far from thermodynamic equilibrium and can change their position in the free energy landscape by continuous supply of chemical energy and matter.[17]

1.2 Non – equilibrium structure formation processes

Non – equilibrium structure formation processes could be separated into two classes, dynamic self – assembly (also known as out – of equilibrium self – assembly or

dissipative assembly) and self – organization. In dynamic self – assembly, primary building blocks are coupled to a chemical reaction cycle that consumes energy, leading to spontaneous assembly of the building blocks.[19] In self – organization, spatial – temporal order or temporally stable patterns arise in a reacting system due to interconnected feedback loops between different types of components in the system. Dynamic self – assembly is the most basic type of non – equilibrium structure formation process and could be transformed into a self – organization by adding a feedback network.[20] Self – organization processes are diverse and can expand from simple elementary levels to hierarchical levels and can be seen in a vast range of systems from biological cells to galaxies in the universe.[21,22] Spatial/temporal pattern formation in reaction diffusion systems could be categorized under self – organization as a non – equilibrium structure formation process, where Turing pattern formation is one example.

1.3 Dissipative assembly

The inspiration to create synthetic dissipative assembly reaction cycles was drawn from the dynamics of microtubules and actin filaments in biological cells. Microtubules and actin filaments are part of the scaffold a cell is built on and define the shape, structure, and mechanical properties of the cell.[23,24] Microtubules assist in various cellular functions, such as cell division, intracellular transport, and cell motion, which requires them to rapidly reconfigure their structure to execute a given task.[23] Microtubules achieve the necessary structural change, growing or shrinking, by undergoing a dissipative assembly cycle (**Figure 1.1a**).[25]

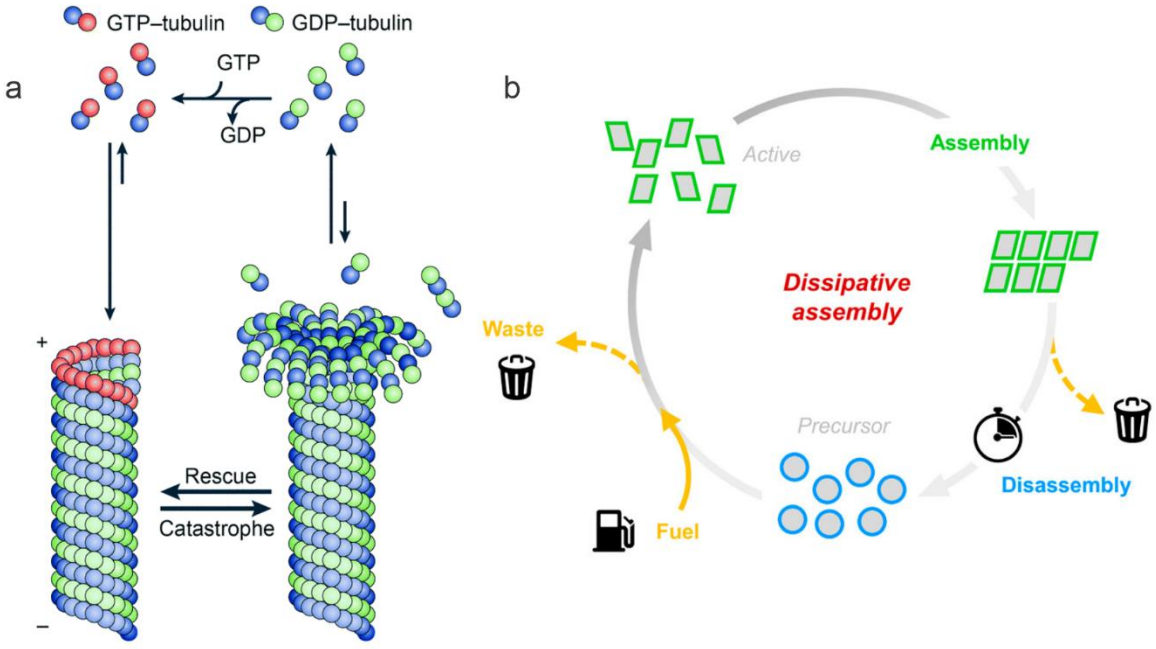

Figure 1.1. (a) Dynamic instability of microtubule. Figure adapted with permission from reference.[18] (b) Dissipative assembly cycle. Figure adapted with permission from reference.[26]

A generic dissipative assembly cycle where the primary building blocks directly participate in the reaction cycle can be described as follows. Here building blocks could be proteins, peptides, colloids, nanoparticles, polymers, or small organic molecules dissolved in a solvent. The primary building blocks in their initial state are at thermodynamic equilibrium and sit at the global energy minimum. When a 'chemical fuel' is supplied to the system (another molecule or direct energy source), the building blocks transform from a 'passive' state to an 'activated' state through a chemical reaction that changes the building block chemical structure. Building blocks in their activate state readily undergo assembly (**Figure 1.1b**).[26] The active building blocks are no longer in thermodynamic equilibrium and reduce the free energy by assembling through covalent or non – covalent bonds. Simultaneously, a back reaction reverses the 'activated' state to original 'passive' state, in

other words deactivates the building blocks. The deactivation takes place on both discrete activated building blocks in the dispersion as well as the activated building blocks in the assembled structures. Once losing the active state the building blocks start to disassemble from the assembled structures and regenerate the discrete building blocks. Both assembly and disassembly take place at the same time and the rate of each reaction determines whether the structures would grow or diminish. A continuous supply of chemical fuel is required to maintain an assembled structure. In most synthetic reaction cycles a continuous supply of energy is not used and a limited amount of fuel is supplied at the beginning. Here the deactivation reaction rate is designed to be much lower compared to the activation reaction immediately after chemical fuel addition. When the fuel is consumed by the activation reaction the assembly rate decreases and the deactivation reaction rate takes over. In the end, once all the fuel is depleted, the original state is restored. The assembly cycle could be restarted by injecting the chemical fuel again. The building blocks could take the form of molecules or colloidal particles. In molecular dissipative assembly different type of structures were observed such as transient hydrogels made by small organic molecules,[27] peptides[28,29] and proteins,[30] transient micelles made by assembly of surfactants and block – copolymers,[31,32] vesicles made by assembly of surfactant – ATP complexes,[33] transient organic colloid formation by aggregation of hydrophobic anhydrides,[34] transient emulsion droplets in aqueous media[35] and coacervation with RNA.[36] These various out – of – equilibrium structures of molecular dissipative assembly occurred through polymerization by covalent bonds, association by non – covalent bonds or phase separation.

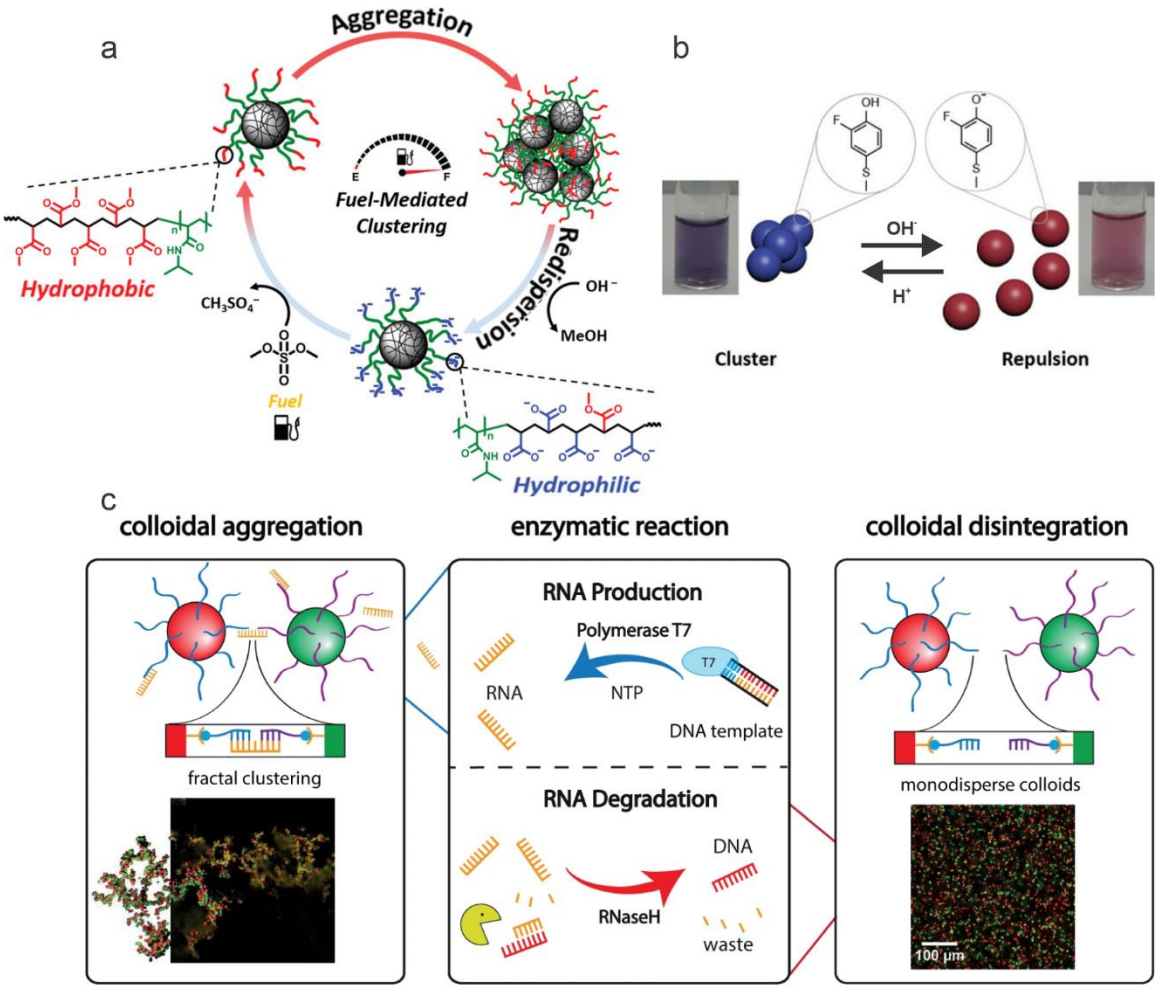

Figure 1.2. Chemically fueled dissipative assembly of colloids. (a) Nanoparticles directly involved in energy dissipation during dissipative assembly. The hydrophilic terminal groups of the surface ligands react with the chemical fuel and are converted to a hydrophobic terminal group leading to aggregation of nanoparticles. Hydrolysis of hydrophobic terminal groups back to hydrophilic groups causes disassembly. Figure adapted with permission from reference.[37] (b) Temporal variation in solution pH induced transient assembly of nanoparticles. Figure adapted with permission from reference.[38] (c) Linker molecule mediated transient nanoparticles assembly. Figure adapted with permission from reference.[39]

In colloidal dissipative assembly, transient assemblies are formed through direct or indirect means. In the first approach, the colloidal particles directly participate in the dissipative reaction network *via* reactions between colloidal particle surface ligands and chemical fuel. The surface ligands go through activation and deactivation reactions that change the attractive and repulsive forces between the particles.[37,40,41] During activation, an increase in the magnitude of attractive forces leads to colloidal assembly and deactivation reactions restore the initial ligand and disassemble the colloids. In the work by van Ravensteijn *et al.*, a methylating agent, dimethyl sulfate increased the hydrophobicity of polymer coated colloids by converting carboxylic acid terminated surface ligands to methoxy groups, which caused particle clustering within 2 hours (**Figure 1.2a**).[37] The methoxy groups on the surface ligands are metastable in water and hydrolyzed back to hydrophilic carboxylic acids over 24 hours, causing the clusters to fall apart. In the second approach, colloidal particles do not directly participate in the reaction network, but the activation and deactivation reactions of other components in the colloidal dispersion modulate the interactions between colloids.[26] For example, Heuser et al. devised a system where time dependent pH changes in the solution protonated and deprotonated surface ligands of nanoparticles, which regulated the electrostatic repulsion between nanoparticles (**Figure 1.2b**).[38] In another method, Ouyang et al.[42] and Dehne et al.[39] (**Figure 1.2c**) exploited bridging between particles through specific binding of a linker molecule to the surface ligands of the particles. The concentration of the linker molecule was controlled by a dissipative reaction cycle and production of linker molecule led to bridging between particles, hence assembly of colloids. Chemical degradation of the linker molecules led to disruption of the bridging between particles and caused disassembly. In another method

Bian et al. exploited assembly of colloids through oppositely charged ions in solution by tuning the ion valence with a dissipation cycle, where multivalence resulted in nanoparticle aggregation and mono – valence resulted in nanoparticle disassembly.[43] Waste molecular products are produced during reaction of chemical fuels during dissipative assembly; accumulation of these byproducts in the system with subsequent dissipative assembly cycles can ultimately lead to irreversible aggregation.[37] This drawback of chemical fuels can be avoided by using light as the energy source for dissipative assembly.

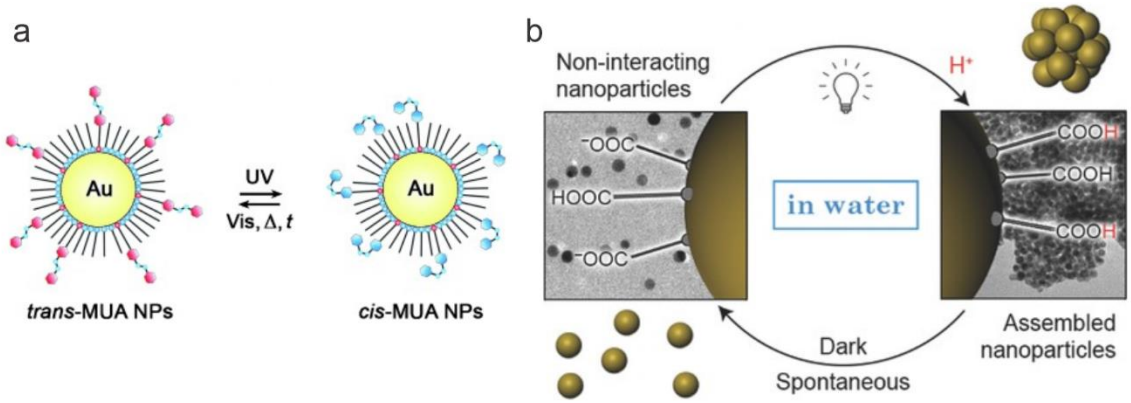

Figure 1.3. Dissipative assembly energized by light. (a) Trans – cis conformational change of azobenzene based surface ligands manipulated for dissipative assembly of gold nanoparticles. Figure adapted with permission from reference.[44] (b) Solution pH mediated by illumination of photoacids for transient cluster formation. Figure adapted with permission from reference.[45]

UV and light irradiation were used in both direct and indirect means for colloidal particle dissipative assembly.[44,46–49] Azobenzenes are commonly used in dissipative assembly cycles by exploitation of the light induced trans – cis conversion. Klajn et al. coated nanoparticles with an azobenzene ligand in its stable trans conformation and used UV illumination to convert the ligands to the unstable cis conformation and clustering of

the nanoparticles. Clustering was reversed by removing the UV irradiation (**Figure 1.3a**).[44] Light induced ring – closure of a spiropyran based photoacid was utilized to temporarily vary pH in solution, controlling protonation/deprotonation of charged surface ligands of nanoparticles (**Figure 1.3b**). Time dependent electrostatic interactions between nanoparticles controlled clustering and disassembly.[45]

1.4 Interparticle interactions mediating colloidal assembly.

Prediction of the outcome of molecules based dissipative assembly systems is possible through modelling reaction kinetics. Whereas, both reaction kinetics and aggregation kinetics should be considered for colloidal systems as energy dissipation is controlled by reaction kinetics while aggregation kinetics preside over colloidal assembly. This makes it harder to determine the right experimental conditions for dissipative assembly in a colloidal system and to discover new colloidal systems exhibiting dissipative assembly. During colloidal dissipative assembly, the particles assemble or disassemble through mediation of interparticle interactions, irrespective of their direct or indirect involvement in the energy dissipation reactions. Therefore, keen interest should be given to interparticle interactions mediating aggregation kinetics during dissipative assembly.

1.4.1 Pairwise interaction potential

The characteristics and magnitude of the interactions between colloids can be expressed by the energy of the interactions. Pairwise interaction potential function represents the energy between two interacting colloids arising due to different physical and chemical phenomena. A negative potential indicates a net attractive interaction while a positive potential indicates a net repulsive interaction. Earlier interpretations of colloidal

interactions accounted for attractive van der Waals interactions and repulsive electrostatic interactions in the famous Derjaguin, Landau, Verwey and Overbeek (DLVO) theory. DLVO theory presents pairwise interaction potential (Φ_{Total}) as the summation of electrostatic potential (Φ_{elect}) and van del Waals potential (Φ_{vdw}) as follows.[50]

$$\Phi_{Total} = \Phi_{elect} + \Phi_{vdw}. \quad (1.1)$$

Additional non-DLVO interactions between particles in addition to these two interactions were identified and included in the interaction potential to explain colloidal stability. Some of these interactions include steric interactions (Φ_{steric}) and hydrophobic/hydrophilic interactions (Φ_{hyd}).

$$\Phi_{Total} = \Phi_{elect} + \Phi_{vdw} + \Phi_{steric} + \Phi_{hyd}. \quad (1.2)$$

Physically, interactions between two colloids manifest as repulsive or attractive forces between the colloids in a solution. The interaction potential (Φ) relates to the interaction force (F) across the distance of closest approach (h) as follows.

$$\Phi = -\int F\, dh \quad (1.3)$$

While the interaction force indicate the magnitude of the net attractive/repulsive interaction between particles, the interaction potential represents more informative metric to assess the colloidal stability and aggregation kinetics.[51] A colloidal dispersion will not necessarily undergo aggregation when experiencing attractive forces between particles due to existence of energy barriers that cannot be overcome by thermal energy. Expression of interaction between two colloids as a potential allows comparison of interparticle interactions with the thermal energy of particles, which has a characteristic scale of $k_B T$, where k_B is Boltzmann's constant. Also, interaction potential gives useful information

about stability of the dispersion and whether the dispersion is more prone to reversible assembly or irreversible assembly.

The thermodynamic modelling of interaction potential between two colloidal particles with separation distance results in a potential energy curve that typically shows a primary energy minimum and a primary energy maximum. The primary minimum is located at the point of particle contact and represents irreversible aggregation of the colloidal solution due to strong attractive Van der Waals forces between particles. The primary maximum represents the energy barrier preventing aggregation of the colloids and in system with only DLVO forces is due to the balance between electrostatic repulsion and Van der Waals attraction. The height of the primary maximum compared to the characteristic thermal energy of the colloids defines whether the colloids are kinetically stable or unstable. In other words, if the primary maximum height is much greater than $k_B T$ the colloids will be stable against aggregation. In some cases, the interaction potential curve shows a shallow secondary minimum at particle separations greater than primary maximum, which can result in reversible clustering in the solution when particles get trapped in the secondary minimum (**Figure 1.4**). Here, irreversible aggregation occurs in a two-step process where first a reversible cluster forms in the secondary minimum would transform into an irreversible aggregate after gaining enough thermal energy to cross the energy barrier.[52] The reversible aggregation associated with the secondary minimum presents the possibility of using equilibrium colloidal interaction models to interpret colloidal assembly during dissipative assembly cycle. In the following section we discuss some common interparticle interactions between colloids that is necessary to explain particle assembly behavior.

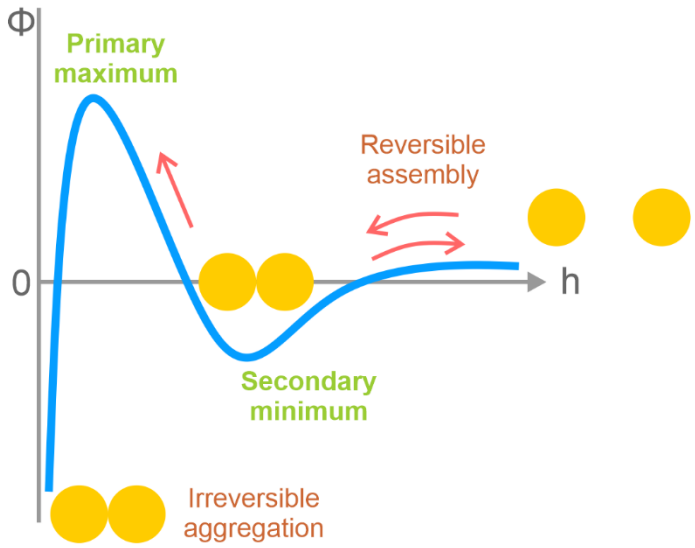

Figure 1.4. Pairwise interaction potential of two colloidal particles.

1.4.2 van der Waals interactions.

Earlier works into deviation of gaseous systems from ideal gas laws paved path to first identifying van der Waals attraction forces between molecules and atoms. The strong attraction forces between colloids during colloidal aggregation made the researchers identify a similar force acting between macroscopic bodies as well. van der Waals forces are also behind several physical phenomena such as condensed phase separation, wettability of surfaces, capillarity due to surface tension and surface adsorption.[53] Van der Waals forces are a type of forces acting between neutrally charged atoms and molecules due to polarity of the electron clouds. There are three types of van der Waal's forces, namely Keesom forces, Debye forces and London dispersion forces. Dipole – dipole interactions between molecules with permanent polarized electron clouds such as water molecules give rise to Keesom forces, forces acting between a permanent polarized molecule inducing a dipole in another non - polar molecule refers to Debye forces and induced dipole - induced dipole forces acting due to charge fluctuations in electron clouds of two non - polar

molecules are London dispersion forces.[50,54] Not only in between atoms and small molecules, van der Waals forces acts between larger molecules such as biomacromolecules and polymers, particles (colloids and nanoparticles), surfaces and even in bulk materials.

When the size scale becomes larger from simple atoms or molecules to a cluster of atoms or molecules such as colloids, the contribution from the first two van der Waals forces become less important and London dispersion forces becomes the most important force. Therefore, in most texts the van der Waals forces in colloidal systems are referred to as London dispersion forces..[50,51,54] Even though non - polar molecules have a zero net dipole, the instantaneous charge distribution fluctuates due to electron orbital motion and the resulting dipole fields fluctuate. At a given time locations of orbital electrons may give rise to a momentary polarity in a molecule, and the arising electric field will interact with another non - polar molecule in close proximity. The charge distribution of the other molecule changes in response and gives rise to this electrodynamic attractive force.[50,51,55]

Using pair wise additivity approximation to atomic/molecular systems Hamaker estimated the van der Waals' interaction energy for two macroscopic bodies and this force was found to be longer range than molecular van der Waals forces. The van der Waals interaction energy varies depending on the geometry of the two bodies, the material properties of the interacting bodies as well as the distance between the two bodies. For a simple colloidal system consisting of equally sized spheres the van der Waals interaction potential is given by,

$$\Phi_{vdw} = -\frac{A}{6} * \left[\frac{2r^2}{h^2+2rh} + \frac{2r^2}{(h+r)^2} + ln\left(\frac{h(h+4r)}{(h+2r)^2}\right)\right]. \quad (1.4)$$

Here A is the Hamaker constant, h is the distance of closest approach between the spheres, and r is the sphere radius. The Hamaker constant encompasses the material

properties that decide the magnitude of the van der Waals interactions, including primarily the dielectric constant of the colloids. In colloidal assembly, particles interact through a solvent and particle – solvent interactions should be accounted for in addition to inter – particle interactions. Particle interactions with the intervening solvent decrease the Van der Waals interactions and can be represented by an effective Hamaker constant, which is not only a property of the particles but depends on solvent properties as well.[56] The presence of electrolytes and other molecules in the medium between two bodies can have a considerable effect on the van der Waals attraction forces as well.[55] But estimating these deviations is not simple and requires time consuming experiments. Therefore, in the studies of colloidal assembly in aqueous solutions, the Hamaker constants of colloids materials with water as the intervening medium are assumed. While most of the time van der Waals interactions are attractive, in some cases it can take a repulsive form which would be included in the Hamaker constant as a negative value. Particles composed of the same material interacting through a solvent or vacuum always give rise to attractive van der Waals forces, which is the case for the scope of this thesis.

In the context of dispersion forces, at longer separation distances there is a significant time delay between the point of emission of electromagnetic waves from an induced dipole to the point of receival of response electromagnetic field from the second body, during which the electromagnetic field from the first body/dipole induces a dipole in the second body with favorable configuration for attractive forces. During this time delay, the orientation of the dipole in the first body changes and is no longer in line with the second body, which weakens the attractive forces between two bodies. This is called retardation effects and a correction factor should be included in the interaction potential to

account for the reduction of van der Waals attraction at larger separations.[50,51] The correction factor for two interacting spheres is as follows,

$$f(h) = 1 - 0.0532\, h \times 10^9 \ln\left(1 + \frac{18.80}{h \times 10^9}\right). \quad (1.5)$$

The resulting equation after including the correction factor in equation (1.4) is used for estimation of van der Waals contribution to the interaction potential between two colloids.

$$\Phi_{vdw} = f(h) \times -\frac{A}{6}\left[\frac{2r^2}{h^2+2rh} + \frac{2r^2}{(h+r)^2} + ln\left(\frac{h(h+4r)}{(h+2r)^2}\right)\right]. \quad (1.6)$$

1.4.3 Electrostatic interactions

To maintain a stable dispersion without aggregation, there should be a repulsive force arising between particles that balances attractive van der Waal's forces. As described by the DLVO theory this repulsive force is electrostatic in nature and originates due to particles acquiring a surface charge. There are several ways for particles to gain a surface charge, such as loss/gain of electrons from crystal lattice, adsorption of charged molecules on the surface, and ionization of surface functional groups. The commonly used method to stabilize particles in a solution is coating the surface with organic ligands to introduce a surface charge and repel similarly charged particles from coming together.

In an aqueous particle dispersion, positively and negatively charged free ions exist in addition to particles and water molecules. When a particle carrying a surface charge is suspended in solution, the surface repels free ions with similar charge, 'co – ions', and attracts oppositely charged ions, 'counterions', from solution, which creates a distribution of ions in the vicinity of the particle that is different from that of homogenous bulk solution. Counterions tightly pack in a few nanometer region near the surface of the particle due to

attractive Coulombic forces and this region is called the Stern layer. Between stern layer and bulk solution there exists another region depleted in co – ions and enriched in counterions. This 'diffuse layer' is dynamic as ions at equilibrium freely move in and out of this region. As counterions in stern layer are not sufficient to neutralize the surface charge, more counterions feels drawn to the surface, but also get repelled by the similar charges in the Stern layer, which creates a distribution of counterions with a high concentration near the Stern layer that gradually reduces in concentration with increasing separation from the surface. In contrast, the concentration of co – ions start to grow from lowest concentration near the surface to the bulk solution concentration at the end of the diffuse layer. This charge distribution profile around a particle consisting of a Stern layer and a diffuse layer is called electric double layer. The thickness of this electric double layer is characterized by the 'Debye length,' which depends on the properties of the solution and the temperature. The Debye length is calculated from the ionic strength and dielectric constant of the solvent. The standard expression for the Debye length for a 1:1 electrolyte is as follows.

$$\kappa^{-1} = \sqrt{\frac{\epsilon\epsilon_0 RT}{2000e^2 {N_A}^2 I}}. \tag{1.7}$$

Here N_A is Avogadro's number, R is the universal gas constant, T is the absolute temperature, $\epsilon\epsilon_0$ is the absolute permittivity of the solution, e is the elementary charge, I is the ionic strength of the solution in molar units and κ is the Debye parameter.

When the particle freely moves through the solution a layer of liquid fixed around the particle moves with it as a single entity. The edge of this layer is called the 'slipping plane' as it the any fluid flow velocity goes to zero at this plane. The location of the slipping plane is within electric double layer and most of the time coincides with the edge of Stern

layer. The potential energy at slipping plane is called the 'zeta potential,' which is a measure of the electrochemical potential at the surface and is related to the colloid surface charge density. The zeta potential is important because it can be experimentally measured using light scattering, while the true surface potential of the colloids is difficult to directly measure. At higher surface charge density, the zeta potential is also higher, which reflects a stable particle dispersion. Dissociation and protonation of surface functional groups is affected by solution conditions, e.g. pH, which alters the surface charge density.

When two particles approach each other the electric double layers around the particles overlap and create a repulsive force. The electrostatic repulsive potential depends on both surface potential and Debye length, and exponentially decreases with increased particle separation. The interaction potential arising from electric double layer overlap between two charged spheres with identical size and surface charge is calculated as follows:[57]

$$\Phi_{elect} = \frac{32\pi\epsilon\epsilon_0 r {k_B}^2 T^2}{z^2 e^2} tanh^2\left(\frac{ze\psi_s}{4k_B T}\right) e^{-\kappa h}, \quad (1.8)$$

where k_B is the Boltzman constant, z is the valence of the charged groups and ψ_s is surface potential. The surface potential was approximated by the experimentally measured zeta potential, ζ_p.

1.4.4 Steric interactions

Electrostatic stabilization is not effective at high salt concentrations due to a small Debye lengths, which allows attractive Van der Waals forces to cause aggregation.[57] Also lack of free ions in organic solvents prevent development of a double layer around particles which results in weak repulsive electrostatic forces.[56] Particles in these instances can be

stabilized by introducing polymer brushes on particle surfaces. Here the spatial interference by these bulky molecules on two approaching surfaces gives rise to a repulsive force and prevents particles from aggregating, hence called Steric interactions. Colloids could be stabilized in a solution solely depending on steric forces by using neutral polymers (e.g., polyethylene glycol) or with both electrostatic forces and steric forces by using charged polymers (e.g., polyelectrolytes).

Polymers are attached to surfaces in three different ways. Adsorption of polymers onto the surface of particles is one method of stabilizing particles in a solution. Here some segments of the polymer chain are physisorbed on the particles surface while the rest is suspended in the solvent.[58] The layer of adsorbed molecules is dynamic and reversible depending on the solution chemistry as molecules are not permanently attached to the surface. Another way of achieving polymer attachment to colloids is to utilize polymers with two chemically different segments. One end of the polymer is poorly soluble in the solvent and/or has a strong affinity towards the particles surface while the rest of the molecule is soluble.[58] These molecules assemble on particles with the segment soluble in the solvent stretching out into the surrounding media, while the other end anchors onto the particle surface. Here the attachment of the molecules to particles is much stronger than in adsorption. Surfactants and block co-polymers to decorate particle surfaces are examples of this method. The third method is tethering a polymer chain onto the particle surface by a functional group at one end of the chain, which is covalently bound to the surface.[58]

When two particles approach each other, the polymers on both particle surfaces are crowded together. When polymers are not permanently attached to the surface, there is the possibility of polymers moving away from the area of interaction or desorption and

solubilization in the bulk solution.[56] Also when two particles approach closer, a polymer chain adsorbed on one particle might feel attraction to the other particle and would latch onto the other particle surface as well. This bridging between two particles leads to flocculation in the dispersion which is the reverse of steric stabilization.[55,56] In chemically anchored polymers, the grafting density remain constant and polymer ligands do not desorb depending on the solution conditions. In the scope of this thesis, we have used both polymeric and metallic particles with polymer ligands chemically grafted on the surfaces and steric interaction for this scenario was considered when estimating interaction potential between particles.

Polymer – solvent interactions are important in steric stabilization as polymer chains collapse on the surface in a poor solvent due to unfavorable polymer – solvent interactions. Therefore, polymer ligands will not be a good stabilizer in a poor solvent. When one terminal of the polymer is chemically attached to a surface, the rest of the chain stretches out and assumes an equilibrium length decided by the grafting density and polymer – solvent interactions. This equilibrium length is the thickness of the ligand shell on the surface. When the distance at closest approach between two particles goes below twice the length of ligand layer, the polymer brushes of two particles start interacting and get pushed together. Due to the high concentration of polymer in this region, osmotic pressure increases and contributes to an increase in repulsive force between surfaces. At the same time stretched out polymer coils are restored; elastic energy of polymer coils is reduced which prefer decrease of the distance between surfaces and contributes to lower the repulsive forces.[51,58]

The Alexander – de Gennes equation for two flat surfaces in a good solvent sums up the two contributions to steric interaction, increase in osmotic pressure and decrease in elastic energy as follows.[58]

$$F_{Steric} = \frac{kT}{s^3}\left[\left(\frac{2L}{h}\right)^{9/4} - \left(\frac{h}{2L}\right)^{3/4}\right] \; for \; h < 2L \tag{1.9}$$

Where F_{Steric} is the force per area, L is the length of a polymer brush, h is the distance between two surfaces at closest approach and s is the parking diameter of an individual polymer brush. A simple exponential equation as an approximation to the Alexander – de Gennes equation was proposed by Israelachvili, which is commonly used for steric interaction between two approaching polymer covered surfaces.[51]

$$F_{Steric} = \frac{kT}{s^3} kT e^{-\pi h/L} \; for \; 0.2 < h < 0.1 \tag{1.10}$$

Later studies discovered that steric interactions exist beyond the distance of $h = 2L$ and above exponential estimation of steric interactions to be more applicable.[51] From equation (1.10) the steric interaction for two spheres is derived and given below.[59]

$$\Phi_{\text{Steric}} = \frac{200 r L^2 k_B T}{\pi s^3} e^{-\pi h/L} \tag{1.11}$$

where r is radius of the two spheres.

1.4.5 Hydrophobic / Hydrophilic interactions

Interactions between solvent molecules and surface ligands must be considered in addition to electrostatic, steric, and Van der Waals interactions. Interactions between solvent molecules and structure of solvent molecules are perturbed by introduction of a foreign species to the solution. For water this is specifically true since there exists strong short ranged hydrogen bond networks between water molecules with spatial directionality due to its polar nature and tetrahedral structure.[60] When the solute species has affinity

towards water or in other words can form polar bonds with water molecules it is called a hydrophilic species. Hydrophilic species tend to be dissolved in water and instead of disrupting hydrogen bond network in water it forms hydrogen bonds or electrostatic charge – dipole bonds with water molecules. A surface covered with hydrophilic groups can form strong bonds with water molecules and could be called a hydrophilic surface. The wettability of hydrophilic surface is higher and a water droplet spreads over a large area maximizing the contact with the hydrophilic surface. Even without surface charge, which gives rise to electrostatic repulsion forces, some particles are soluble in aqueous solutions due to hydration shells that give rise to effective repulsive forces between neighboring particles. When a hydrophilic surface is submerged in an aqueous solution, water molecules form bonds with the surface and structure into layers of water molecules spreading from the surface into bulk solution providing a hydration shell around the surface. When two such hydrophilic surfaces approach closer, reluctance of hydration shells on the surfaces to be disturbed and displace the water molecules in the intervening region increases osmotic pressure in the region and results in repulsion between the surfaces.[60]

Alternatively, when non – polar species are submerged in water, inability to form hydrogen bonds or charged – polar bonds with water makes them partially or completely immiscible in water, giving rise to hydrophobic effects. Surfaces decorated with hydrophobic groups have a very low wettability where water does not spread and minimizes the contact area with the surface giving droplets with high contact angles. A hydrophobic molecule in water disturbs the highly directional short – range order of water and water molecules rearrange around like a cage that optimizes the number of hydrogen

bonds, which is entropically unfavorable. Therefore, to reduce the high free energy in the system attractive forces arise between nearby hydrophobic species in water.[61,62] Self – assembly of different macromolecules, such as formation of lipid bilayers, vesicles, and micelles are examples of hydrophobic attraction forces. Proteins folding where hydrophobic groups are enclosed inside could be attributed to hydrophobic attraction forces as well. These biomacromolecules in water are stabilized by repulsive interactions between hydrophilic groups exposed to solvent.

When hydrophobic surfaces or hydrophobic colloidal particles are submerged in water, water molecules adjacent to the surface cannot form bonds with the surface and introduce an adjoining depletion zone.[63] The attraction between two hydrophobic surfaces was experimentally found to be greater in both magnitude and range compared to the van der Waals attractions in some cases, but there are diverse reports of magnitude and range for hydrophobic interaction.[64] How hydrophobic attraction originate in these instances was explained with different theories including expulsion of water molecules from the intervening region due to entropically unfavorable ordering of water molecules (disruptions to hydrogen bond network) or formation of cavities by highly fluctuating water molecules (vapor – liquid phase transition) or coalescence of nanobubbles.[64,65] The difficulty in deriving a physical mechanism for hydrophobic interaction including all the different variables is the reason for lack of a thermodynamic model for hydrophobic interactions despite having well established models for other DLVO and non – DLVO interactions.[61,64]

There is a lack of a single theory that can be used to explain both hydrophobic and hydrophilic interactions. According to experimental observations, both hydrophobic and

hydrophilic interactions between two surfaces showed an exponential decay with increasing separation distance, with similar decay lengths of 0.3 – 2 nm.[63] Based on this fact, Israelachvili *et al*. developed an empirical DLVO type interaction potential model for hydrophobic and hydrophilic interactions.[63] To represent the degree of hydrophobicity (net hydrophobic area) of surfaces, a non – dimensional factor, the hydra parameter, H_y, was introduced into the interaction potential.

$$H_y = 1 - \frac{a_{Hydrophilic}}{a_{Hydrophobic}} \tag{1.12}$$

Here, $a_{Hydrophilic}$ is the hydrophilic surface area and $a_{Hydrophobic}$ is the hydrophobic area of two interacting surfaces. The Hydra parameter can range from $-\infty$ to 1 and determines whether the interaction would be hydrophobic or hydrophilic, where $H_y < 0$ represents repulsive hydrophilic interactions and $0 < H_y \leq 1$ represents attractive hydrophobic interactions.[63,66] The empirical formula for hydrophobic / hydrophilic interaction energy per unit area, Φ_{hyd}, is as follows.

$$\Phi_{hyd} = -2\gamma H_y e^{-(h/D_0)}. \tag{1.13}$$

Here γ is the polystyrene – water interfacial tension and D_0 is the hydrophobic interaction decay length.

1.5 Pattern formation in reaction – diffusion systems

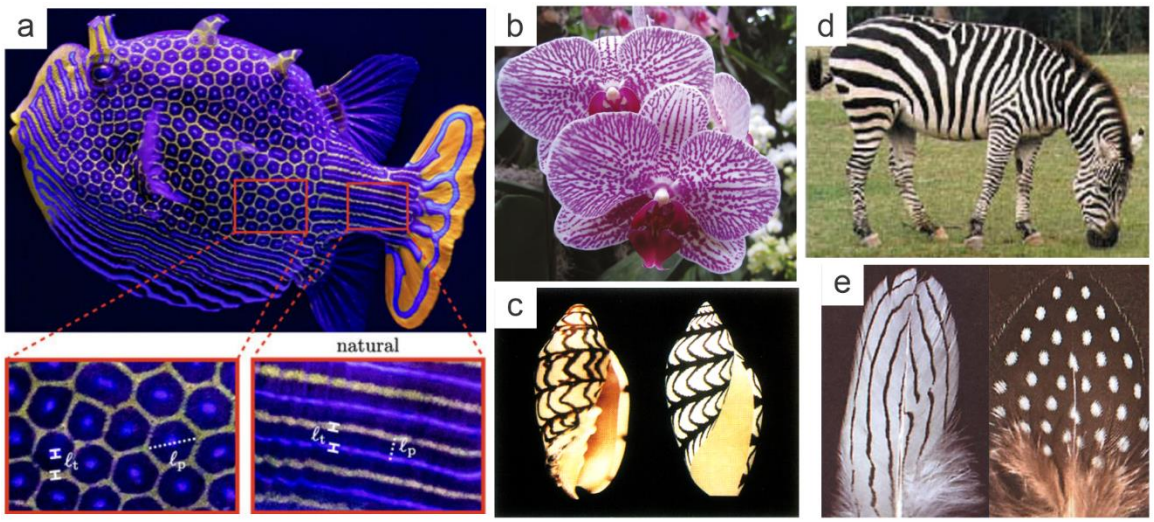

Figure 1.5. Patterns emerging in nature by reaction – diffusion. (a) Hexagon and stripe patterns of an Ornate Boxfish. Figure adapted with permission from reference.[67] (b) Pigment patterns in flower petals of orchid flowers. Figure adapted with permission from reference.[68] (c) Pigmentation patterns on seashells surfaces. Figure adapted with permission from reference.[69] (d) Black and white stripes on a zebra. Figure adapted with permission from reference.[70] (e) Stripe and spot pigmentation patterns within feathers. Figure adapted with permission from reference.[71]

Reaction – diffusion systems are an essential part of nature in the self – organization of living systems from small molecules to large structures as well as in facilitating different functions.[72,73] The idea of spatial patterns emerging in reaction – diffusion systems was first proposed by mathematician Alan Turing in 1952.[74] He proposed that concentration patterns emerge in space when initially uniformly distributed substances react and diffuse at different rates. He postulated that reaction – diffusion instability is the mechanism by which homogenous spherical embryos break spatial symmetry to develop digits during

morphogenesis. In 1972, Gierer and Meinhart came up with constraints under which these spatial patterns could be generated by introducing autocatalysis and inhibition reactions to the reaction – diffusion model by presenting the concept of 'local activation and lateral inhibition'.[75] Living cells and tissues employ reaction diffusion mechanisms to form spatial patterns during development, which are called Turing patterns. Examples of Turing patterns manifesting in nature (**Figure 1.5**) are skin pigmentation patterns in different organism such as fish,[76–78] octopus,[79] flowers,[68] sea shells,[80] coloration of birds,[81] skeletal patterning of fish,[82] feather branching of birds,[83] vascular patterns in plant stems,[84] limb digitation[85] and spacing between hair follicles growth.[86] Despite the literal meanings of reaction – diffusion, the versatility of the basic concept of Turing model, activation and inhibition could be applied to explain spatial patterns across many systems including non – living systems. The ripples on sand dunes,[87] geographic population dynamics,[88] bacteria colonies,[89,90] and cloud patterns in the sky[91] can be explained by reaction – diffusion instability.

The simplest reaction model for Turing pattern formation includes two chemical species, an activator molecule and an inhibitor molecule. The activator catalyzes its own production (autocatalysis) as well as the production of inhibitor molecule. Meanwhile, the inhibitor obstructs further production of the activator. The inhibitor has a higher diffusion coefficient relative to the smaller diffusion coefficient of activator. Random fluctuations in an initially homogenous distribution causes autocatalysis of activator and buildup of the activator leading to a local concentration peak (**Figure 1.6**). Simultaneously, the inhibitor is also produced, and concentration of inhibitor increases. The inhibitor diffuses out faster than the activator and suppresses the concentration of activator in the vicinity. The faster

diffusion rate of inhibitor leads to local enhancement of activator and decrease of its own concentration at the activation site, which helps maintaining the local concentration peak of activator. Initiation of the production of activator in other places in the space leads to appearance of more peaks and as the inhibitor – rich regions overlap between these peaks a periodic pattern is created.

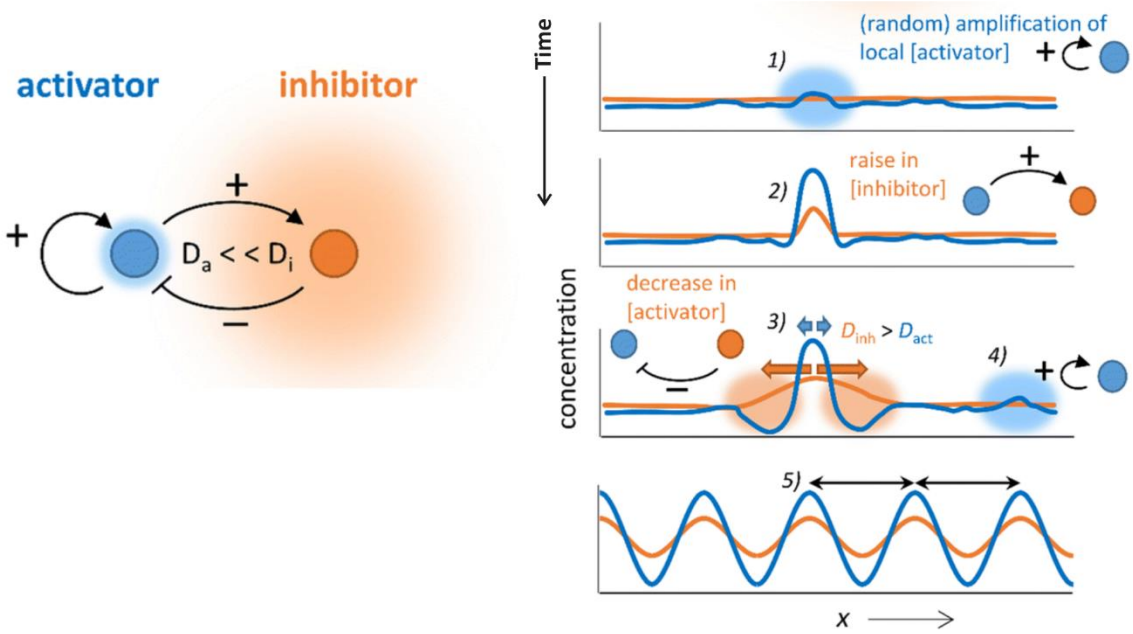

Figure 1.6. Mechanism of reaction – diffusion instability and Turing pattern formation. Figure adapted with permission from reference.[92]

There is a vast library of theoretical reaction – diffusion models explored that generate spatial patterns,[93–95] the most basic and popular models being Gierer-Meinhardt model and Gray – Scott model. Also various types of spatial patterns beyond simple spot and stripe patterns were generated through mathematical modelling.[96] Despite the decades long development of theoretical side of Turing patterns in reaction – diffusion, there is a lack of experimental discovery of synthetic systems exhibiting Turing patterns, which might be due to lack of synthetic autocatalytic reactions.

Castets et al. produced the first experimental evidence of Turing patterns in a synthetic chemical system.[97] They utilized an open gel strip reactor to demonstrate Turing patterns in the chlorite – iodide – malonic acid (CIMA) chemical system in the presence of starch. The iodide ion acted as the activator while the chlorate ion acted as inhibitor where the diffusion coefficient of iodide was reduced by binding with starch molecules. Later different methods were developed to reduce the diffusivity of iodide ions to regenerate Turing patterns in CIMA reaction.[98–100] Belousov – Zhabotinsky (BZ) reaction,[101] ferrocyanide – iodate – sulphite reaction[102] and thiourea – iodate – sulfite (TulS) reaction[103] are some other examples for chemical systems that were reported to manifest Turing patterns.

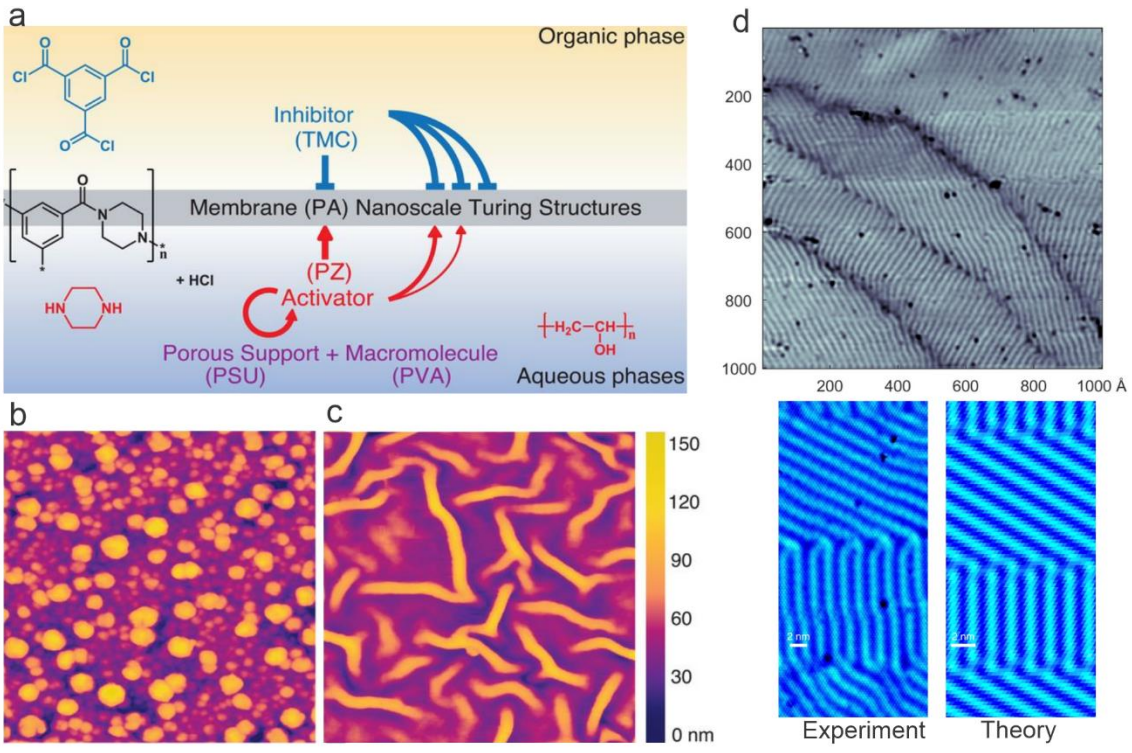

Figure 1.7. Nanoscale Turing patterns. Turing patterns in a polyamide membrane, (a) reaction – diffusion mechanism during interfacial polymerization. AFM images of (b) spot patterns and (c) stripe patterns in the polyamide membrane. Figure adapted with permission

from reference.[104] (d) Stripe patterns in a bismuth monolayer. Figures adapted with permission from references.[105,106]

So far there are only a few nanoscale systems exhibiting Turing patterns.[104,106,107] The most studied experimental system generating nanoscale Turing patterns in recent years is the interfacial polymerization of polyamide membranes that are commonly used for filtration and reverse osmosis applications. In interfacial polymerization of polyamide membranes, an organic solution phase acyl chloride monomer reacts with an aqueous phase amine at the liquid – liquid interface. Tan et al. realized that this interfacial polymerization could be manipulated to generate a reaction – diffusion based Turing pattern and they demonstrated spot and stripe like nanoscale patterns in the membrane at different reaction conditions (**Figure 1.7a-c**).[104] Here, amine molecule acts as the activator molecule and acyl chloride which has a low solubility in water acts as the inhibitor. Amine molecule in aqueous phase promotes polymerization diffusing into organic phase while acyl chloride molecule in organic phase reacts with the amine and make the polymer which prevents further penetration of amine into organic phase, thus effectively controlling the growth of the membrane. The disparity of diffusion coefficients between activator and inhibitor was achieved by facilitating binding of the activator to a large molecule, in this case PVA and restricting activator motion by confining it to a porous support. Following this study several other groups also were successful in revealing Turing structures in polyamide membranes.[108–110] Different strategies were used to slow the diffusion of activator amine molecule by facilitating its binding to larger entities like cucurbituril and metal organic frameworks.[109,110] A fascinating synthetic nanoscale Turing pattern system occurs in a bismuth monolayer grown on a niobium diselenide ($NbSe_2$).[106] The remarkable similarity

between ripples observed on the bismuth monolayer and zebra stripes, led the way to the discovery that these ripples emerge from a Turing type mechanism (**Figure 1.7d**).[105] The mismatch between lattice constants between bulk bismuth and $NbSe_2$ is believed to be the cause of these ripples. Here, Fuseya et al. modelled formation of stripes in bismuth monolayer using a mathematical model adapted from Turing reaction – diffusion model where reactants were replaced by displacement of atoms. Vertical displacements, which give rise to stripes, were postulated as the activator while in plane lateral displacements were postulated as inhibitor. The reaction – diffusion mechanism is underexplored as a method for patterning nanoscale systems to this date, despite its desirable traits. Coupling nanoparticle assembly with a reaction – diffusion system presents great potential for template free nanopatterning.

1.6 Liquid phase transmission electron microscopy for visualizing nanoscale dynamics

Liquid phase transmission electron microscopy (LPTEM) has advanced over the past two decades as a means of nanoscale imaging of hydrated species and chemical or physical processes occurring in natural or synthetic systems in liquid medium. To observe a species or process in liquid inside a transmission electron microscope, there should be a liquid layer that would be thin enough to be penetrated by the electron beam. Also the liquid layer should be sealed inside a cell made by a material that is transparent to electrons as well as that could be stabilized inside the high vacuum of the microscope.[111,112] Several strategies have been developed up to this date to enable this task either by fashioning the sample cell using silicon chips or by simply repurposing conventional TEM grids or by utilization of 2D materials in various settings. The commonly used and commercially

available setup for LPTEM is comprised of a specially made TEM holder (**Figure 1.8a**) where the tip of the holder is fabricated in such a way that a vacuum sealed sample cell could be made by assembling two silicon chips with windows in the middle, separated by use of thin spacers (**Figure 1.8b**). A thin silicon nitride layer (SiN_X) ~50 nm deposited on the insides of silicon chips is transparent to high energy electrons and facilitates observing the species and processes inside the liquid cell through the window. These silicon chip based liquid cells can be assembled in either static mode or flow mode according to the experiment and liquid cell holders have multiple microfluidic lines incorporated for facilitating liquid flow into the cell. The flow setting could be utilized either for replenishing chemicals consumed in different processes during imaging or for in – situ mixing of several chemicals.[113,114] Also integrating electrodes on the silicon chips has enabled heating of the samples to observe temperature dependent processes[115–118] and applying voltage bias for electrochemistry experiments.[119–121]

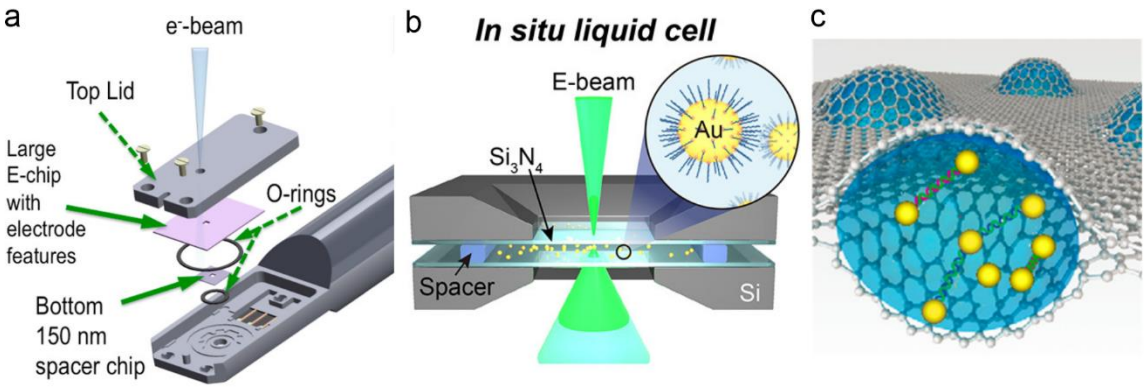

Figure 1.8. Different strategies for LPTEM (a) Liquid cell TEM holder. Figure reproduced with permission from reference.[119] (b) Liquid cell made out of Si chips with SiN_X membrane window. Figure reproduced with permission from reference.[122] (c) Graphene liquid cell. Figure reproduced with permission from reference.[123]

The liquid thickness inside the liquid cell can range from hundreds of nanometers to several micrometers. When the liquid cell is inside the TEM, due to the pressure difference between the liquid inside and outside vacuum, the SiN_X membrane would bow out and this bulging increases the liquid thickness at the window. The energy loss of electrons travelling through a thick sample and beam broadening due to scattered electrons reduces the imaging resolution significantly. The thickness of the SiN_X membrane can also contribute to these effects.[124,125] Liquid cells prepared by incorporating 2D materials such as graphene alleviate this problem as here the electron transparent membrane is only a few atomic layers thick, and the liquid layer is ~100 nm in thickness. These liquid cells were made by entrapping the liquid containing sample between two graphene sheets by manipulation of strong van der Waals attraction between graphene (**Figure 1.8c**). This results in small nanosized liquid pockets between two sheets.[126,127] These liquid cells made of 2D sheets are often supported on conventional TEM grids. Other 2D materials such as boron nitride (BN) and molybdenum sulfide (MoS_2) have also found their way in to fabrication of liquid cells for TEM.[128,129] To avoid random sized liquid samples with varying thickness and volume, graphene liquid cells were improved by integrating graphene sheets over a patterned silicon support with wells.[130–132] Recently a sophisticated graphene liquid flow cells were made by introducing graphene sheets over holey silicon nitride membranes of custom made silicon chips.[133] Myriad of nanoscale processes in liquid medium such as nucleation and growth,[116,126] etching,[134] nanoparticle assembly,[135–139] oriented attachment,[140] superlattice formation,[141] electrochemical deposition,[142] electrochemical degradation, corrosion, bubble dynamics, nanodroplet dynamics,[143] biomineralization,[114,144] soft material dynamics,[117,118,145] small molecular dynamics,[146,147]

biological structure dynamics[148,149] have been observed by implementation of LPTEM techniques.

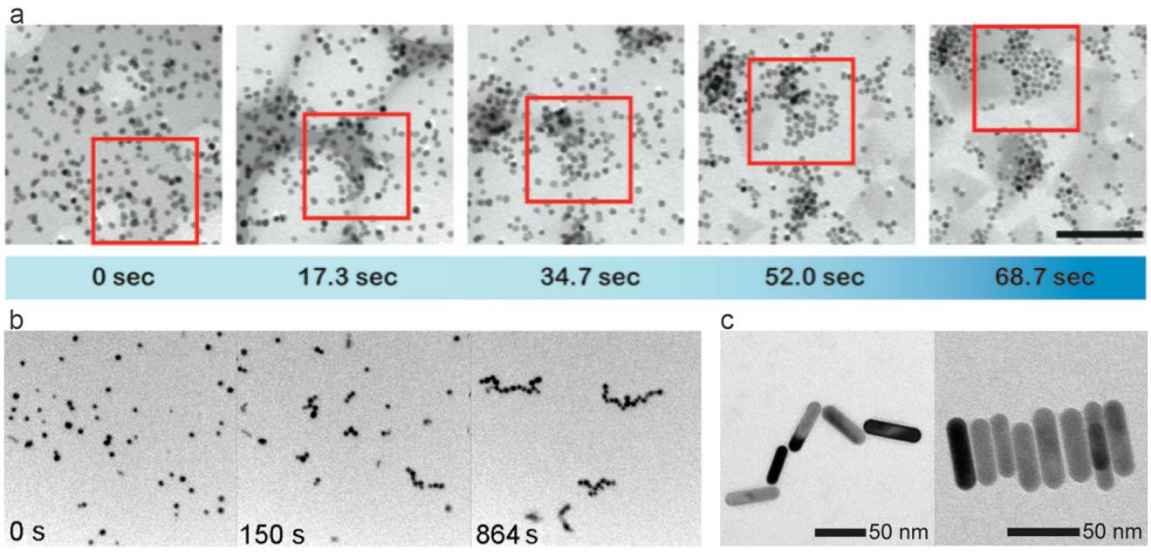

Figure 1.9. Nanoparticles dynamics in LPTEM (a) crystallization of 7.3 nm Pt nanoparticles into a superlattice. Figure reproduced with permission from reference.[141] (b) self – assembly of Au nanoparticles into chains. Figure reproduced with permission from reference.[139] (c) different conformations of Au nanorods in end – end and side – side assemblies. Figure reproduced with permission from reference.[150]

Among these processes visualizing nanoparticle motion and assembly dynamics in aqueous media hold special interest to us due to the crucial role nanoparticle assembly plays in bottom – up strategy for nanofabrication (**Figure 1.9**). Nanoparticles made of different metals such as Au, Pt or a composite of metals such as Pt – Fe, PbSe, CdSe/CdS have been used widely in LPTEM due to high contrast resulted by strong electron scattering of high atomic number metallic particles as well as their relative degradation resistance with extended periods of electron irradiation during imaging.[135,141,151,152] Nanometer resolution in LPTEM and in some cases sub – nanometer resolution has enabled visualizing

nanoparticles of few nanometers to couple hundred nm in size. Most of the nanoparticles that have been observed are spherical particles with isotropic properties, but directional interactions of anisotropic particles such as nanorods, nano – arrows, nanoprisms and octapods were monitored as well.[151] Tip – tip assembly of nanorods, stacking of nanoprisms, chain assembly of octapods and side – side assembly of nano – arrows[153] due to directional interparticle interactions were transformed into superlattices[154] and moire lattice[155] by tuning experimental conditions in subsequent studies. In situ changes to the morphology of nanoparticles during assembly such as nanocrystal deformations during superlattice phase changes,[152] oriented attachment of assembled particles by rotation to align the crystal planes[140] were captured by LPTEM. Assembly driven by a receding liquid boundary[156] or arrangement of nanoparticles in surface templated nanochannels[157] were realized by drying / solvent evaporation induced assembly in LPTEM. DNA coated nanoparticle assembling through DNA hybridization and surfactant coated nanoparticles assembling through hydrogen bonding realized linker molecules mediated assembly in LPTEM.[148,158] Real time measurements of interparticle interactions between individual particles is an advantage that are accessible to LPTEM , but could not be achieved in nanoscale by other techniques. Powers et al showed that the chain assembly of superparamagnetic particles (Pt – Fe) at first was due to anisotropic interactions while the later stage contraction into superlattices was due to van der Waals interactions.[159] Lee et al was able to identify the type of interparticle interaction dominating in each step of nanoparticle superlattice formation by cluster growth (**Figure 1.10a**).[122]

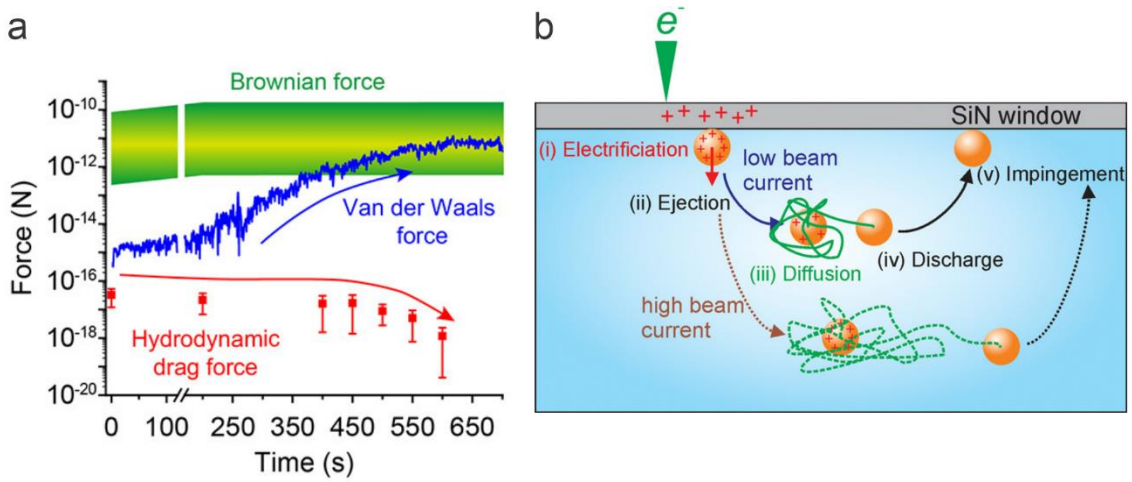

Figure 1.10. (a) Fluctuation of theoretically estimated interaction forces during assembly of Au nanoparticles. Figure reproduced with permission from reference.[122] (b) Mechanism of nanoparticle surface diffusion by electrostatic interactions. Figure reproduced with permission from reference.[135]

In addition to these complex systems, simple systems with metallic spherical nanoparticles were imaged in LPTEM in common aqueous solutions and buffers. In these studies, one of the recurring observations irrespective of particle surface chemistry or solution chemistry was the controlled motion of the nanoparticles. In the study by Woehl and Prozorov, the carboxylated particles in acetate buffer showed sporadic sticky motion of nanoparticles on SiN_X membrane (**Figure 1.10b**).[135] They postulated this to surface diffusion of nanoparticles by electrostatic means. Electrostatic charging of both SiN_X membrane and nanoparticles by electron beam and subsequent electrostatic interactions between the two regulate the particle motion during assembly. The electrostatic charging by electron beam was also evidenced by immediate discharge of particles from the image area just after imaging started.[160] The stick and hop/slip motion of nanoparticles were observed in several other studies as well. Chee et al. posited the intermittent adsorption –

desorption of nanoparticles at the SiN_X – solution interface to stable/unstable adsorption sites on SiN_X membrane determined by uneven charge distribution.[161] Evidence contrary to stick and hop/slip motion was also apparent by continuous motion of nanoparticles in several other studies.[123,160] Most of the studies saw an increase in particle motion and fast diffusion with increasing electron flux / electron dose rate (modulated by electron beam current and magnification).[135,160,161] The beam effects were also supported by observations of nanoparticles mobilization and assembly limited to the imaging area.[160] The measured diffusion coefficients of nanoparticles in LPTEM experiments were several order of magnitudes lower than that in a bulk solution. In addition to electron beam effects, substrate interactions arising from confinement in a small volume of liquid inside the liquid cell such as rise in hydrodynamic drag on nanoparticles at a liquid – solid interface[160] or increase in solvent viscosity by ordering of solvent molecules at the interface[162] contribute to this deviation in diffusion coefficients. Despite altered motion of nanoparticles in the liquid cell makes it hard to draw parallels with ex – situ experiments of assembly dynamics in bulk liquid, LPTEM give useful information about nanoparticle dynamics at solid – liquid interfaces.[163] However, a recent study was successful in achieving Brownian motion similar to that of bulk liquid in 150 nm nanoparticle dispersions of 3 – 4 μm in thickness.[164] But the loss of resolution in thick liquid samples, hence the necessity to use high electron fluxes (high magnifications and high beam currents) would make it difficult to obtain Brownian motion in nanoparticles of smaller sizes (<10 nm).

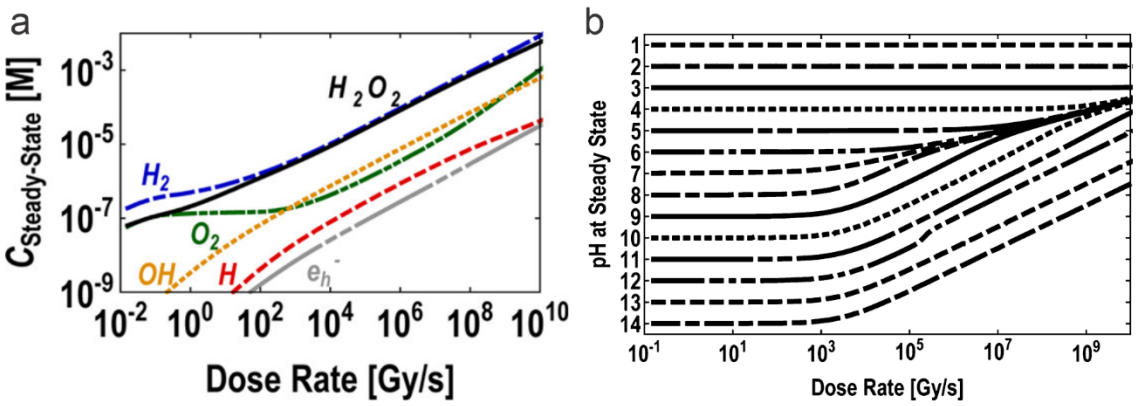

Figure 1.11. Theoretical modelling of radiolysis of water (a) steady state concentration of radical species with electron dose rate (b) pH variation as a function of electron dose rate and initial pH of water. Figures reproduced with permission from reference.[165]

Radiolysis of liquid samples during LPTEM imaging can make irreversible changes to solution chemistry that would impact nanoparticle dynamics. In dilute solution conditions in LPTEM, radiolysis of solvent molecules is much more prominent and can have a considerable effect on the solute species (e.g. molecules, nanoparticles, etc.). Especially in aqueous solutions, water molecules decompose and produce highly reactive species.[166]

$$H_2O \xrightarrow{e^-} H_2O^+, OH^{\cdot}, e_{aq}^-, H^{\cdot}, OH^-, H_2O_2, H_2, HO_2 \qquad (1.14)$$

These reactive species will further undergo reactions with solute species which will lead to modifications or damage to the original structure of the species. Not only that, pH variations of solution also occur and Schneider et al demonstrated this by modelling radical reactions of water in liquid cell (**Figure 1.11**).[165] Among the radicals produced by radiolysis of water hydrogen radical and hydrated electrons have highly reducing properties while hydroxyl radical have highly oxidizing properties. For example, reducing the nature of hydrated electrons could be manipulated to synthesize metal nanocrystals while the

oxidizing nature of hydroxyl radicals could be manipulated to dissolve them.[166] The whole field of nucleation, growth, and degradation of metallic nanomaterials in LPTEM is consolidated on creative utilization of beam – sample interactions. Ability to produce reducing environment comparable to ex – situ bench top synthesis conditions achieved through chemicals such as sodium borohydride has paved the way for understanding heterogenous nucleation pathways of nanocrystals.[167] Despite the large number of studies done on this subject, less effort has been directed to characterize effects of radiolysis on surface capping ligands which are crucial in stabilizing nanoparticles in solution as well as deciding nanoparticle assembly dynamics and pathways. Surface capping ligands could be categorized under soft materials, and they are mostly small molecules or large organic molecules such as polymers or DNA. The hydroxyl radical and hydrogen radicals are highly reactive towards organic molecules and react to produce radicals on either carbon backbone or functional groups. These radical sites leave an opening for more reaction where two radical sites on two separate molecules form a bond leading to intermolecular crosslinking or the bond between the radical site and adjacent atom is broken through chain scission resulting in two fragments.[168,169] Nagamanasa et al. employed graphene liquid cell electron microscopy to capture both intermolecular crosslinking and chain scission of polymer molecules.[170] These results from previous studies on radiolysis of aqueous organic molecule solutions suggests that there would be irreversible changes to nanoparticle ligand shell during LPTEM imaging which is worth exploring.

1.7 Goals and outline of the dissertation

The aim of this dissertation is to probe the dynamics during formation of colloidal and nanoparticle assemblies by non – equilibrium assembly mechanisms. Mainly we focused on two types of non – equilibrium phenomena that are known to make dynamic assemblies and patterns in nature, dissipative assembly and reaction – diffusion systems. We utilized optical microscopy for visualizing chemical fuel dependent dissipative assembly of colloids and liquid phase transmission electron microscopy (LPTEM) to visualize nanoparticle surface pattern formation by reaction – diffusion instability. Also, a special interest was given to study electron beam – sample interactions during LPTEM during in – situ nanoscale imaging of nanoparticles assembly in liquid, as these interactions drive the reaction – diffusion instability for nanoparticle surface pattern formation. In this dissertation we have addressed the following questions.

1. How does colloidal surface chemistry change during fuel driven dissipative assembly?
2. Do hydrophobic interactions play an important role during dissipative assembly and could we develop methods to measure colloidal surface hydrophobicity?
3. Can we use pairwise colloidal interparticle interactions models developed for colloidal aggregation to explain out – of equilibrium assembly?
4. How do electron beam – sample interactions during LPTEM imaging modify organic capping ligands and polymers used for nanoparticle stabilization and surface functionalization?
5. How can we harness electron beam – polymer radiolysis reactions during LPTEM to create a reaction – diffusion instability to make stable nanoparticle patterns?

The answers to the first three questions are discussed in **Chapter 2**. Here we selected carboxylated polystyrene microspheres as the model system and successfully established the chemical fuel range in which dissipative assembly occurs for this system. We developed a correlative fluorescence spectroscopy-based method to measure time dependent surface hydrophobicity of microspheres to estimate contribution of hydrophobic interactions for colloidal assembly at different chemical fuel concentrations. We demonstrated that conventional interparticle interaction model with a secondary minimum can be used to predict the outcome of a system undergoing dissipative assembly. We showed that hydrophobic interactions between particles were necessary to explain experimental observations of irreversible aggregation at high fuel concentrations.

The work discussed in **Chapter 3** addresses question 4. We performed electron dose – controlled irradiation experiments in LPTEM and using a correlative fluorescence microscopy method it was established that organic capping ligands undergo polymer radical reactions. The hydroxyl radicals produced by radiolysis of water attacks polymer capping ligands which underwent competing crosslinking and chain scission reactions making modifications to the SiN_X membrane and metallic nanoparticles. Based on the insights gained from **Chapter 3**, we developed a preliminary experimental model to address question 5 in **Chapter 4**. We used a gold nanoparticle – siloxane polymer system inside the LPTEM to create a wide range of nanoparticle surface patterns such as spot, labyrinth and string. Finally, the conclusions drawn from the work are summarized in **Chapter 5** with proposed future work to advance the work on nanoparticle pattern formation during LPTEM.

Chapter 2. Dynamic Surface Chemistry and Interparticle Interactions Mediating Chemically Fueled Dissipative Assembly of Colloids*

2.1 Introduction

Dissipative assembly is a dynamic assembly process found in nature where assembly and disassembly of cellular structures, *e.g.*, microtubules and actin filaments, are modulated by biochemical reaction networks.[171–173] Here, chemical fuel is consumed by a reaction to convert molecular building blocks, *e.g.*, proteins, to an activated state where they assemble into nanostructures. The structures disintegrate when the fuel is exhausted, and the building blocks are deactivated by a slow concurrent back reaction. Unlike near-equilibrium self-assembly, assembled structures exist only under continuous fuel supply and dissipation of chemical energy.[174] The assembled structure concentration is dictated by reaction kinetics as opposed to thermodynamic interactions in near-equilibrium assembly. This approach applied to synthetic soft matter enables generating transient populations of assembled structures that autonomously disassemble. Various synthetic polymeric, supramolecular, and nanoscale systems have been demonstrated to undergo dissipative assembly, including molecular hydrogelators,[27,175,176] proteins,[30] DNA,[177,178] vesicles[33,179,180] and polymers.[181] Prior synthetic dissipative assembly work has focused primarily on demonstrating similarity to biological systems,[27] discovery of new chemical

* Note: This chapter was previously published by Dissanayake et al. and reproduced here with some modifications: Dissanayake, T.U., Hughes, J., Woehl, T.J., "Dynamic Surface Chemistry and Interparticle Interactions Mediating Chemically Fueled Dissipative Assembly of Colloids", *Journal of Colloid and Interface Science*, **2023**, 650, 972–982.

reaction cycles,[182] applications in drug delivery,[40] and reconfigurable material properties, such as catalytic activity.[33]

Compared to small molecule and polymer building blocks, dissipative assembly of colloids has received relatively less attention.[26,37,40,41,43,183] Several works have utilized chemical fuels that react with and convert charged hydrophilic surface ligands into uncharged hydrophobic groups bound to the colloid by metastable ester bonds. For example, the reaction cycle developed by Grötsch and Boekhoven *et al*. activates colloids by reacting a carbodiimide fuel molecule with surface carboxylic acid groups to form metastable hydrophobic groups that induce transient particle aggregation.[40,41] Here it was posited that diminished repulsive electrostatic interactions and enhanced attractive hydrophobic interactions between colloids led to assembly. A slow simultaneous hydrolysis reaction recovers carboxylic acid ligands after the fuel is exhausted, causing nanoparticles to disassemble over several hours.[40,41] A similar method was developed by Van Ravensteijn *et al*. for micron sized polymer colloids using dimethyl sulfate as the chemical fuel.[37]

While several chemistries for dissipative colloid assembly have been established, *a priori* determination of system parameters (fuel concentration, colloid surface chemistry and concentration, pH, ionic strength) required to prescribe the aggregate lifetime, size, and concentration remains challenging. On the other hand, the impact of reaction conditions on assembled structure concentration can be effectively modeled with homogeneous reaction kinetics for dissipative assembly of small molecules.[27,184] Homogeneous reaction kinetics are not predictive for dissipative colloid assembly due to several complicating factors. Prior works have noted that adding excessive chemical fuel

led to irreversible aggregation due to 'overactivation' of the colloids, while too little fuel caused no assembly.[41] Likewise, chemical fuel molecules react with surface bound ligands or polymers during dissipative colloid assembly as opposed to free molecules in bulk solution. Fuel-ligand reactions exhaust fuel within less than an hour compared to the time scale for colloidal aggregation,[41] which occurs over several hours. Surface reaction rates govern chemical activation of the colloids, while colloidal aggregation is mediated by electric double layer, Van der Waals, steric, and solvation interparticle interactions.[185] Finally, complex phenomena can modify the deactivation reaction rate beyond what is predicted by reaction kinetics, such as trapping of metastable hydrophobic groups in poorly hydrated interstitial spaces between colloids.[186] The complexity of dissipative colloid assembly indicates that reaction kinetic models are not sufficient to predict conditions for dissipative assembly. Rather, systematic and quantitative measurements of the time dependent colloid surface chemistry (*e.g.*, surface charge and hydrophobicity) and dynamic interparticle interactions during assembly are a required first step toward developing predictive kinetic models for dissipative colloid assembly.[26]

In this article, we reconcile reaction conditions for fuel driven dissipative assembly and irreversible aggregation with dynamic surface chemistry measurements and interparticle interaction models. We utilize the carbodiimide fuel reaction cycle initially developed by Grötsch and Boekhoven *et al.*,[40,41] which has emerged as one of the most important reaction cycles in the dissipative assembly field. This reaction cycle relies on attractive hydrophobic interactions to aggregate colloids, which are challenging to quantify with experiments and colloidal theory. We measure the colloid surface chemistry during dissipative assembly to quantify dynamic hydrophobic and electrostatic interactions that

inform a pairwise colloidal interaction potential model. The model was broadly consistent with experimental observations of dissipative colloid assembly, explaining phenomena such as transient aggregation, fuel concentration dependent aggregate concentration, and irreversible aggregation. This is the first study to quantify dynamic colloid surface chemistry and interparticle interactions during dissipative colloid assembly and we expect the approach and insights here can be broadly applied to other colloids and nanoparticles. We expect these results will lay the groundwork for a mechanistic understanding of the interplay between fuel reaction kinetics, colloid surface chemistry, interparticle interactions, and assembly kinetics during dissipative colloid assembly. A holistic understanding of these physicochemical processes during dissipative colloid assembly is a necessary precursor to realize more complex transient colloidal structures, such as colloidal superlattices [187–189] and colloidal molecules,[190–193] and complex, multistage reaction cycles that have been demonstrated for dissipative assembly of small molecules.[194]

2.2. Materials and Methods

2.2.1. Preparation of colloids for dissipative assembly and optical microscopy measurements

A stock solution of 1 μm carboxylated polystyrene particles (Thermofisher, size dispersity (SD) of 2.4%) at a particle concentration of 3×10^9 particles/ml was prepared in a buffer of 5 mM 2-(N-morpholino)ethanesulfonic acid (MES, Thermofisher) and 25 mM N-Hydroxysuccinimide (NHS, Thermofisher). Carboxylic acids were introduced on the colloids by grafting polystyrene colloids with poly(methyl methacrylic) acid (PMMA), which renders the colloids negatively charged and hydrophilic. The buffer was adjusted to a pH of 6.5 with 1 M NaOH (Sigma). 1-Ethyl-3-(3-dimethylaminopropyl)carbodiimide

(EDC, Thermofisher) was added from a freshly prepared stock solution to set the initial EDC concentration to the desired level. The centrifuge tube was inverted several times to dissolve the EDC.

Aliquots were drawn from the particle solution before EDC was added (t = 0 hrs) and at 2 hour intervals for 24 hours. The solution was gently inverted prior to withdrawing each aliquot to resuspend any sedimented particle aggregates. The aliquots were deposited onto a glass coverslip and imaged with an inverted optical microscope (Zeiss Axio Observer) with a 40× magnification objective lens. Each sample was allowed to sediment for 5 minutes and then several images were acquired for each aliquot. This short sedimentation time was chosen as it moved sufficient numbers of colloids into the same focal plane, but avoided additional assembly during imaging. Sedimentation likely led to artificially inflated counts of large aggregates for all experimental conditions but was necessary to form a sub-monolayer coverage of monomers and aggregates on the cover glass. The number of single colloids and oligomers containing up to 10 particles was counted in each image. A similar set of experiments was performed with 500 nm diameter carboxylated polystyrene particles in the same buffer, but with various particle concentrations of 3×10^9 particles/mL, 4.5×10^9 particles/mL, and 6×10^9 particles/mL. For each particle concentration the initial EDC concentration was varied from 5 mM to 15 mM in steps of 2.5 mM, yielding aggregation data for a total of 15 unique conditions. Here aliquots were taken of the particles in buffer only (t = 0 hr) and 4 hrs and 24 hours after EDC addition. An in-house Matlab script was used to measure the number of aggregates and monomers for each reaction condition and reaction time. The fractal dimension of aggregates was determined by the box counting method implemented in Matlab.[195] The

fractal dimension of each aggregate was measured for 9 box sizes ranging from 1 pixel to 256 pixels, with the values reported as the average across all box sizes, plus or minus one standard deviation.

2.2.2. Zeta potential and ANS binding measurements

A stock solution of 1 μm polystyrene particles at a concentration of 3×10^9 particles/mL was prepared at the same buffer conditions as described above. EDC was added to the particles to give final concentrations of 5 mM, 10 mM, and 15 mM and aliquots were drawn at 1 – 2 hour time increments over 24 hours. Two aliquots were drawn out from the particle solution at each time point, one for zeta potential and one for particle hydrophobicity measurements. Zeta potential was measured using a photon correlation spectrometer (Malvern ZetaSizer ZS90) and 3 separate measurements were taken of each sample and averaged. The Smoluchowski model for thin double layers was used to calculate zeta potential from raw electrophoretic mobility data, which is applicable in this system because the Debye length was much smaller than the particle radius (~3 nm). The solution conductivity was measured as a function of time simultaneous to the zeta potential measurements.

The particle surface hydrophobicity was estimated by measuring the fluorescence emission from a lipophilic dye, 8-Anilinonaphthalene-1-sulfonic acid (ANS, Thermofisher), as a function of EDC concentration and time. ANS has strong affinity towards hydrophobic groups and increases its fluorescence quantum yield upon binding. ANS was added to the particle solution at a final concentration of 100 μM. The solution was placed in a quartz cuvette and excited at a wavelength of 375 nm and the fluorescence

emission intensity (I_{ANS}) was measured at 475 nm with a fluorescence spectrometer (Jasco FP-8500). The ANS binding experiments were performed in triplicate.

The calibration curves for quantifying hydrophobic interactions were measured with a different method. A stock solution of 1 μm carboxylated polystyrene particle at a concentration of 3×10^9 particles/mL was prepared at the same buffer conditions described above and ANS was added at a final concentration of 100 μM. EDC was added from a freshly prepared stock solution to 1 mL of particle solution in a quartz cuvette to reach the desired EDC concentration. The fluorescence emission intensity was measured at 475 nm at 2 min intervals for several hours after adding EDC. The experiments were performed under magnetic stirring at 500 rpm to prevent aggregation and break up aggregates to probe the surface hydrophobicity of monomeric colloids.

2.3. Results & Discussion

2.3.1. Kinetics of dissipative colloid assembly

Carboxylic acid functionalized polystyrene colloids with diameters of 500 nm or 1 μm were utilized to allow optical microscopy observations of the aggregation kinetics during dissipative assembly. The particles were diluted to a specified concentration in an aqueous buffer containing MES and NHS, in which they formed a stable colloidal suspension. EDC was added as the chemical fuel at initial concentrations ranging from 2.5 – 15 mM to colloidal suspensions. The carboxylic acid groups on polystyrene particles imbue them with a negative charge and hydrophilic surface. NHS and EDC react with carboxylic acid groups on the colloids to form metastable NHS-ester groups (**Figure 2.1a**),[40,41] which are nonpolar and uncharged and induce aggregation of the colloids by attractive hydrophobic interactions. EDC acts as the chemical fuel, which is consumed and

converted to the inert byproduct, 1-(3-dimethylamino)propyl-3-ethylurea (EDU), in the process. When the fuel is exhausted hydrolysis reactions break ester bonds between the colloid surface and NHS to deactivate the particles, which causes aggregates to break apart.

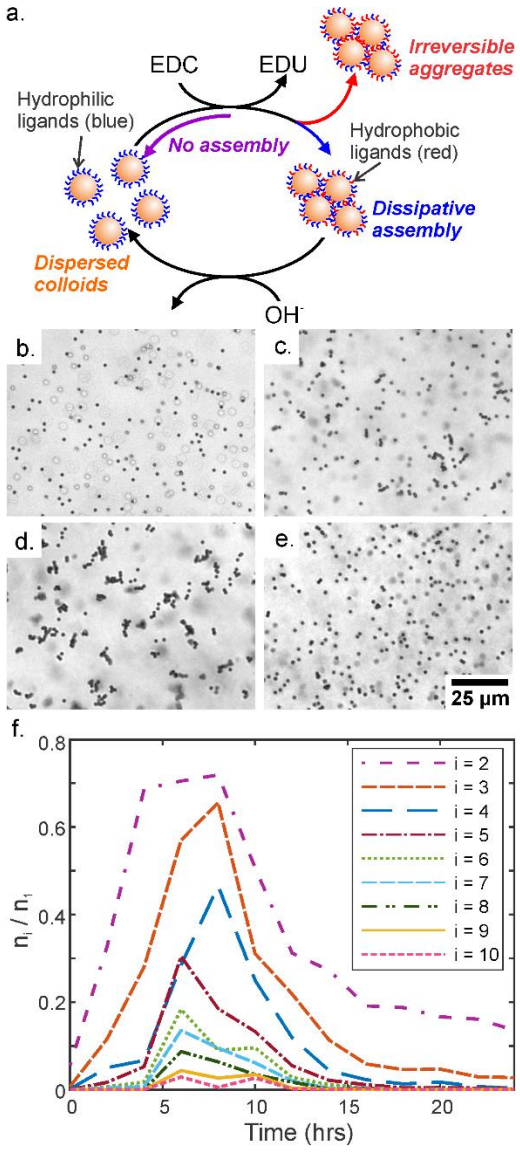

Figure 2.1. Dissipative assembly of polystyrene colloids over 24 hours. (a) Schematic of dissipative colloid assembly using EDC-NHS chemistry. Depending on the EDC fuel concentration and solution conditions, colloids either do not assemble, undergo dissipative assembly, or form irreversible aggregates. (b)-(e) Images of carboxylated polystyrene particles (1 μm) at various times after addition of 10 mM EDC: (b) t = 0 hours (prior to

EDC addition), (c) t = 2 hours, (d) t = 6 hours, and (e) t = 24 hours. (f) Number of aggregates divided by number of monomers as a function of time, where i corresponds to the number of monomers in an aggregate.

In a typical experiment, EDC was added to the particles and aliquots were drawn at different times and imaged with bright field optical microscopy (see Experimental methods for further details). We measured the aggregate size distribution as a function of time for 1 μm diameter particles and the total number of aggregates and single particles as a function of time for 500 nm due to limited spatial resolution. **Figure 2.1b-f** show exemplary images of the dissipative assembly of 1 μm particles for 10 mM initial EDC concentration and the number of each aggregate size as a function of time. Prior to EDC addition the particles existed predominantly as monomers in solution (**Figure 2.1b**). Dimers, trimers, and tetramers were observed in the solution 2 hours after adding fuel (**Figure 2.1c**). The total number of aggregates peaked 6 hours after adding fuel and images showed a continuous distribution of aggregate sizes containing between 2 – 10 particles (**Figure 2.1d**). The number of aggregates decreased after 6 hours and by 16 hours only small aggregates containing 2 – 4 particles were observed. After 24 hours the colloids nearly recovered to the initial state except the dimer count was about 3 times higher than before fuel addition (**Figure 2.1e**). At all times the aggregate concentration decreased monotonically with increasing cluster size.

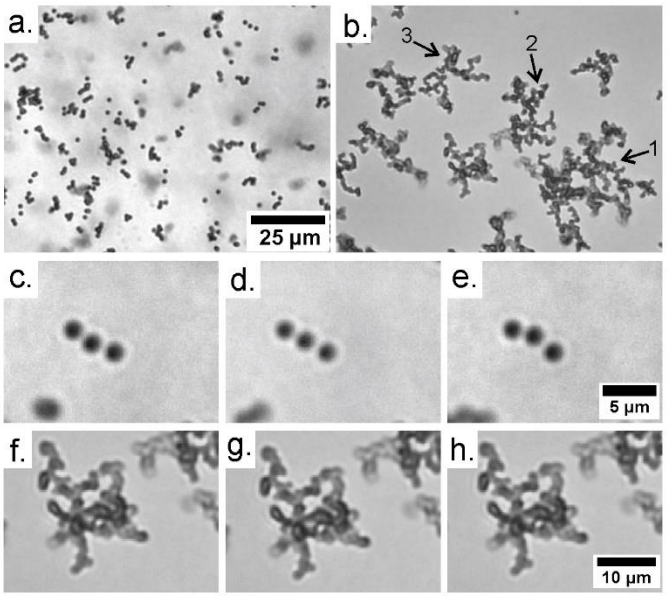

Figure 2.2. The aggregate structure and bonding were qualitatively different for dissipative assembly and irreversible aggregation. (a) Aggregates formed during dissipative assembly 10 hours after addition of 10 mM EDC. (b) Irreversible aggregates formed 4 hours after addition of 15 mM EDC. The arrows denote the aggregates used for fractal dimension measurements. (c) - (e) Time lapsed snapshots from an optical microscopy movie showing motion of individual particles inside an aggregate during dissipative assembly. There is a 2 second time interval between each image. (f) - (h) Time lapsed snapshots from an optical microscopy movie showing no individual motion of particles within a fractal aggregate during irreversible aggregation. There is a 5 second time interval between each image.

We performed a series of experiments varying the EDC concentration to establish reaction conditions over which dissipative assembly and irreversible aggregation occurred (**Figure 2.2**). Similar to previous studies, we observed transient aggregates formed over a range of fuel concentrations with no assembly below a lower critical fuel concentration and irreversible aggregation above an upper critical fuel concentration.[41] Below a fuel

concentration of 5 mM no dissipative assembly occurred. Transient clusters formed at 10 mM EDC persisted for hours and consisted mainly of small aggregates with < 10 particles per aggregate. The aggregates were globular, disordered, loosely packed and co-existed with a nearly equal number of single particles in the solution (**Figure 2.2a**). The aggregate structure and co-existence of aggregates and monomers suggests the colloids were reversibly aggregated, akin to self-assembly. Irreversible aggregation occurred for an initial EDC concentration of 15 mM where large fractal aggregates containing dozens of particles were observed 4 hours after adding fuel, reminiscent of classical diffusion limited colloidal aggregation (**Figure 2.2b**).[196] The fractal dimensions of several aggregates formed at 15 mM EDC were measured using the box counting method (arrows in **Figure 2.2b**), which yielded fractal dimensions of 1.71 ± 0.16 (aggregate 1), 1.67 ± 0.19 (aggregate 2), and 1.66 ± 0.20 (aggregate 3). These values are near the theoretical value of 1.7 for diffusion limited aggregation. The values may be slightly decreased due to the finite size of pixels and aggregates in the images.[197,198] The fractal aggregate size grew monotonically with time and completely consumed all monomers in solution.

A close look at the transient clusters formed during dissipative assembly showed that particles had relatively weak interparticle bonds (**Figure 2.2c-e**). This was evidenced by flexible colloid bonds that enabled particles to move independently within an aggregate, indicating bonds were of a similar strength as thermal forces.[199] Weak interparticle bonds can be broken by thermal forces or collisions once the fuel is exhausted. There was an observable water layer between the particles in the aggregates, which is expected to facilitate hydrolysis of NHS ester groups. On the other hand, particles inside irreversible fractal aggregates formed with 15 mM initial fuel concentration were tightly packed with

close interparticle spacings that could not be resolved by optical microscopy (**Figure 2.2f-h**). The interparticle bonds in aggregates were not flexible and the aggregates translated and rotated as rigid structures. This indicates strong interparticle bonds relative to the thermal energy were present in irreversible aggregates. Close packing of the colloids in aggregates has previously been shown to inhibit deactivation reactions by excluding water from interparticle interstices.[186]

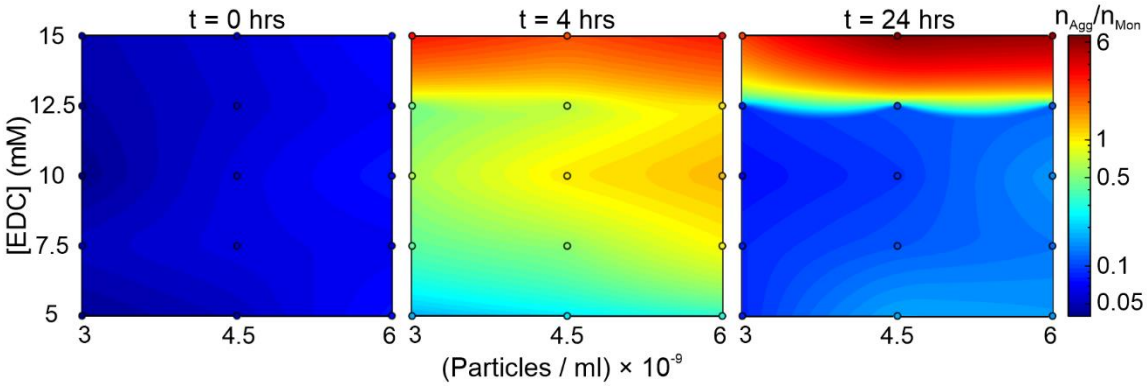

Figure 2.3. Phase diagrams showing degree of aggregation of 500 nm polystyrene particles prior to fuel addition (0 hours) and 4 hours and 24 hours after. Colored circular data points correspond to experimental measurements while the contour heat map was interpolated using a cubic model. The heat map corresponds to the number of aggregates normalized to the number of monomers (n_{Agg}/n_{Mon}) as a function of EDC and particle concentration.

Experiments varying the particle and initial EDC concentration demonstrated the impacts of these parameters on the aggregation behavior of the colloids (**Figure 2.3**). At each reaction condition we measured the number of aggregates prior to fuel addition, 4 hours after fuel addition, and 24 hours after fuel addition. The aggregation data is displayed in three phase diagrams in **Figure 2.3** where each diagram corresponds to one time point. Within each phase diagram the color of each data point corresponds to the experimentally

measured aggregate count normalized to the monomer count (n_{agg}/n_{mon}) as a function of initial EDC concentration (y-axis) and particle concentration (x-axis). The heat map was interpolated between the experimental data based on a cubic model fit. Prior to EDC addition (t = 0 hrs) there were nearly no aggregates in all particle solutions with the aggregate concentration increasing slightly with particle concentration. After 4 hours the number of aggregates increased for all particle and EDC concentrations. For each particle concentration the number of aggregates increased as a function of EDC concentration up to 10 mM, decreased slightly at 12.5 mM, and then increased by 5 – 10 times at 15 mM EDC. It is not currently known why the aggregate number decreased at 12.5 mM EDC concentration. After 24 hours, the phase diagram shows the aggregate number decreased for EDC concentrations between 5 – 12.5 mM at all particle concentrations, indicating dissipative assembly occurred. As shown in **Figure 2.1** there were slightly higher numbers of aggregates after 24 hours compared to the initial condition before EDC addition, indicating a small degree of irreversible aggregation. The aggregate number increased monotonically with time for 15 mM EDC concentration at all particle concentrations, indicating these conditions led to irreversible aggregation.

2.3.2. Evolution of colloid surface charge and surface hydrophobicity during dissipative assembly

Colloid aggregation during dissipative assembly is mediated by colloid surface chemistry and interparticle interactions. Adding fuel to the system converts negatively charged carboxylic acids to non-polar NHS groups, which causes the colloid surface charge to decrease and the surface to become hydrophobic. Based on this understanding, we

measured surface charge and hydrophobicity of the colloids as a function of time during dissipative assembly (**Figure 2.4**).

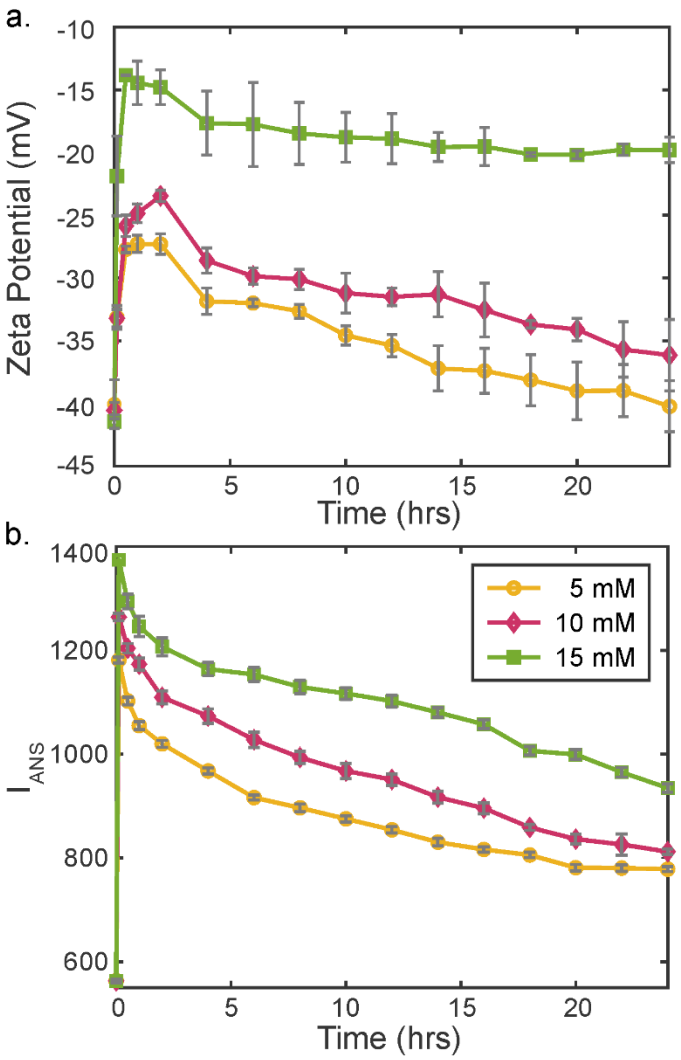

Figure 2.4 Time dependent surface charge and hydrophobicity of colloids during dissipative assembly. Time dependence of (a) zeta potential and (b) ANS fluorescence intensity of 1 µm polystyrene particles after adding various EDC concentrations corresponding to nearly no aggregation (5 mM EDC), dissipative assembly (10 mM EDC), and irreversible aggregation (15 mM EDC). Each data point in (a) and (b) is the mean of

three independent measurements with error bars representing ± 1 standard deviation from the mean.

We quantified the particle surface charge by measuring the zeta potential of the colloids as a function of time after adding EDC (**Figure 2.4a**). Three EDC concentrations were selected representing the existence of nearly no transient aggregates (5 mM), dissipative assembly of transient aggregates (10 mM), and irreversible aggregation (15 mM). Initially, the colloids had a zeta potential of about -40 mV, indicating a stable particle dispersion. The zeta potential magnitude in all three solutions decreased rapidly in the first 1 – 2 hours after EDC addition and reached minimum values of -28 mV, -23 mV, and -14 mV for initial fuel concentrations of 5 mM, 10 mM, and 15 mM, respectively. The zeta potential magnitude increased for each fuel concentration after reaching a minimum value, consistent with regeneration of negatively charged carboxylic acid groups on the particles. The zeta potential magnitude continued to increase for 5 mM and 10 mM EDC to reach values of -40 mV and -36 mV after 24 hours. In contrast, the zeta potential magnitude of the 15 mM EDC solution increased by about 25% until 15 hours, after which it remained approximately constant at –20 mV until 24 hours. The constant zeta potential is consistent with irreversible aggregation forming large particle aggregates with NHS esters trapped in the center, which had lower effective surface charge densities and zeta potentials.

Attractive hydrophobic interactions have been posited to be important for dissipative colloid assembly.[40,41,186,200] However, there is no standard method for measuring surface hydrophobicity of colloids similar to that used for zeta potential. Here we describe a new method utilizing ANS, a fluorescence probe that exhibits strong fluorescence emission upon binding to hydrophobic functional groups. ANS has been

conventionally used to evaluate structural changes in biomolecules associated with polarity changes, such as protein (un)folding,[201] DNA binding,[202] enzyme conformational changes,[203] and protein aggregation.[204] ANS has been used in inorganic colloids to probe binding of hydrophobic biomolecules to metallic nanoparticles.[205] The non-polar anilinonaphthalene group in ANS binds to hydrophobic sites through non-covalent interactions, which increases the ANS fluorescence quantum yield several orders of magnitude compared to a polar solvent (ANS quantum yield = 0.003 in water and 0.4 in ethanol).[206,207] Here ANS preferentially binds to NHS ester groups on colloids, which generates an increase in the fluorescence emission intensity at a fixed wavelength of 475 nm. We added 100 μM ANS to aliquots drawn from particle solutions undergoing reaction with EDC to measure the particle hydrophobicity as a function of reaction time (see Experimental methods for further details). The fluorescence emission intensity at 475 nm increased rapidly to a maximum within minutes after EDC addition and the peak intensity increased as a function of increasing EDC concentration (**Figure 2.4b**). The ANS emission intensity decreased monotonically with time over the next 24 hours with the final value increasing as a function of increasing EDC concentration. The results indicate that colloid surface hydrophobicity increases in a concentration dependent manner after adding EDC. The ANS binding results showed that the particles did not recover their initial surface hydrophobicity, similar to the zeta potential measurements.

2.3.3. Colloidal interactions during dissipative assembly

2.3.3.1. Pseudo-equilibrium colloidal interaction model

In the dilute regime, the stability and aggregation of colloids can be interpreted based on the pairwise potential of mean force between two particles, *i.e.*, the pairwise

interparticle interaction potential.[52,208] While chemical fuel driven dissipative assembly is an out-of-equilibrium process due to continuously changing colloid surface chemistry, significant changes to surface chemistry occur over relatively long time scales of tens of minutes to an hour compared to the diffusive time scale of individual colloids, $\tau_D = \frac{r^2}{D} \approx 0.5\ s$, where r is particle radius and D is the Stokes-Einstein diffusion coefficient of the colloid. If colloids do not irreversibly aggregate, they will respond rapidly to changes in the pairwise interaction potential during dissipative assembly. In other words, we expect that thermodynamic models for interaction potentials can be effectively applied in this case to interpret fuel driven dissipative assembly under the assumption of pseudo-equilibrium conditions.

The formation of reversible aggregates that respond to changes in surface chemistry during dissipative assembly suggests that the interaction potential between the colloids displays a shallow potential minimum, *i.e.*, a secondary minimum, with a depth that changes as a function of time and fuel concentration. In other words, colloidal aggregation during dissipative assembly is akin to a reversible reaction under pseudo-equilibrium conditions. The equilibrium constant slowly changes over time and colloids and aggregates interconvert rapidly compared to the time scale over which the equilibrium constant changes. On the other hand, irreversible aggregation of colloids at large fuel concentrations occurs due to destabilization of the colloidal system, where the primary maximum has an energy much smaller than thermal energy.

Polystyrene particles in aqueous solution interact by repulsive electric double layer overlap interactions, repulsive steric interactions between polymer brushes on the colloid surfaces,[57] and attractive Van der Waals interactions. Based on our experimental

measurements of colloid surface hydrophobicity we expect that hydrophobic interactions contribute significantly to the colloidal interactions as well. The total pairwise interaction potential is described by the sum of each interaction potential:

$$\Phi_{Total}(h) = \Phi_{elect}(h) + \Phi_{vdw}(h) + \Phi_{steric}(h) + \Phi_{hyd}(h). \quad (2.1)$$

Here Φ_{Total} is the total pairwise interaction potential, Φ_{elect} is the potential due to double layer overlap, Φ_{vdw} is the Van der Waals interaction potential, Φ_{steric} is the steric interaction potential, Φ_{hyd} is the hydrophobic interaction potential, and h is the distance of closest approach between the spheres. Generally accepted thermodynamics models exist for each interaction potential except the hydrophobic interaction.[64] The origin of the hydrophobic interparticle interactions is the repulsion of water from the hydrophobic polystyrene particle surface during dissipative assembly,[63] which is transiently coated in non-polar NHS esters. The repulsion of water from the particle surface increases the particle-water interfacial energy, which creates a short ranged attractive interaction between neighboring particles. We utilize an empirical model from Israelachvili *et al*. that proposes pairwise hydrophobic and hydrophilic interparticle forces decay with an exponential dependence on surface separation.[63] Applying the Derjaguin approximation to the flat plate potential produces a DLVO type expression for the pairwise hydrophobic/hydrophilic interaction potential between two spheres of equal size:

$$\Phi_{hyd} = -4\pi r\gamma D_0 H_y e^{-(h/D_0)}. \quad (2.2)$$

Here R is particle radius, γ is the polystyrene – water interfacial tension, D_0 is the hydrophobic interaction decay length, and H_y is the empirical Hydra parameter that quantifies surface coverage of hydrophobic and hydrophilic regions.[59] The Hydra parameter quantifies the ratio between the hydrophobic ($a_{Hydrophobic}$) and hydrophilic

($a_{Hydrophilic}$) surface area of a solid/liquid interface: $H_y = (1 - a_{Hydrophilic}/a_{Hydrophobic})$. A negative Hydra parameter indicates repulsive hydrophilic interactions while a positive Hydra parameter indicates attractive hydrophobic interactions.[63,66]

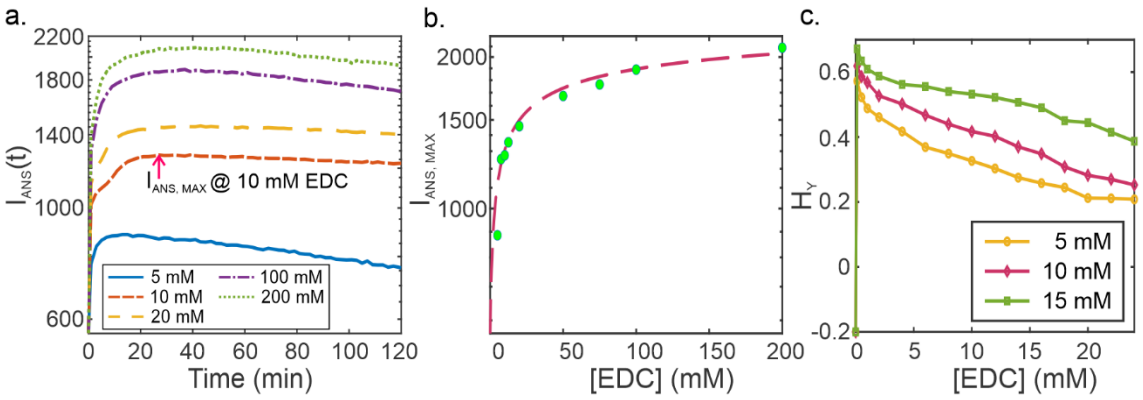

Figure 2.5. Quantification of Hydra parameter using ANS binding measurements. (a) ANS fluorescence emission intensity at 475 nm as a function of time at different EDC concentrations. (b) Maximum ANS fluorescence emission intensity as a function of EDC concentrations. The black line is a logarithmic fit to the data the dashed red line shows the asymptotic emission intensity as EDC concentration goes to infinity, $I'_{ANS,Max}$. (c) The Hydra parameter calculated by applying equation (3) to data in **Figure 4b** as a function of time for three different EDC concentrations.

3.3.2. Quantifying hydrophobic interactions between colloids

We utilized ANS binding measurements to quantify the Hydra parameter. All prior work has utilized the surface force apparatus and data fitting to quantify Hydra parameter.[63] However, the quantitative nature of fluorescence suggests this method can be utilized to determine the Hydra parameter during dissipative assembly experiments. Under the

assumption that a single ANS molecule binds to each NHS ester and the fluorescence quantum yield of each ANS molecule is identical, the fluorescence emission is directly proportional to the number of NHS ester groups on the particle surface and thus the hydrophobic surface area, $I_{ANS} \propto a_{Hydrophobic}$ (**Appendix A2**). We note that contributions of the native colloids and organic solutes to changes in the ANS quantum yield and emission intensity were removed from the measurement by subtracting off the initial ANS emission intensity of the particle solution prior to adding EDC. The hydrophilic and hydrophobic areas are divided in the Hydra parameter expression so the unknown proportionality constants are divided out and fluorescence emission intensities can be used to directly quantify the Hydra parameter. To determine the hydrophilic surface area, we performed a set of calibration experiments to determine the fluorescence emission intensity proportional to the total surface area of the colloids, $I'_{ANS,Max} \propto a = a_{Hydrophobic} + a_{Hydrophilic}$. Here EDC was added at concentrations ranging from 5 mM to 200 mM to solutions of polystyrene colloids and the ANS fluorescence emission intensity was measured for several hours. As illustrated in **Figure 2.5a** the fluorescence intensity increased with time until about 20 minutes and then decreased over several hours. The rate of fluorescence decay here is related to the hydrolysis reaction rate of NHS esters but cannot be reconciled with dissipative assembly kinetics because the colloids were subject to vigorous stirred in this experiment. The maximum fluorescence intensity observed for each EDC concentration ($I_{ANS,Max}$), which corresponded to the maximum coverage of NHS groups, followed a logarithmic dependence on EDC concentration (**Figure 2.5b**). The value of the maximum emission intensity as EDC concentration goes asymptotically to infinity ($I'_{ANS,max}$) was determined from the logarithmic fit and represents the condition

when the colloid surfaces were saturated with NHS groups, *viz.*, $I'_{ANS,max} \propto a$. This indicates the hydrophilic area will follow the proportionality, $a_{Hydrophilic} \propto I'_{ANS,max} - I_{ANS}$. Equipped with fluorescence emission intensity values proportional to the hydrophobic and hydrophilic area the Hydra parameter can be quantified as follows,

$$H_y = \left(1 - c\frac{I'_{ANS,max} - I_{ANS}}{I_{ANS}}\right), \tag{2.3}$$

where c is a constant that depends on the Hydra parameter of the native colloids prior to EDC fuel addition. The Hydra parameter of the colloids prior to EDC addition is unknown; however, the Hydra parameter has been observed to range from $-0.2 < H_y \leq 1$ in prior works.[63] Based on the polar nature of carboxylic acids on the colloid surface we presumed the initial particle surface had a Hydra parameter of –0.2, giving a value of $c = 0.277$. **Figure 2.5c** shows the corresponding values of Hydra parameter after applying equation (2.3) to the fluorescence emission intensity data in **Figure 2.4b**, which are used to compute the hydrophobic interaction potentials in **Figure 2.6** and **Figure 2.7**.

2.3.3.3. Modeling the interaction potential of colloids during dissipative assembly

We utilized the time dependent zeta potential and Hydra parameters to calculate the pairwise interaction potential during dissipative assembly under conditions equivalent to the experiment in **Figure 2.1** (**Figure 2.6**). The values of other parameters, such as the Hamaker constant and the polymer brush thickness were estimated based on literature values or assigned reasonable values if literature values were not available (**Table A1**).[57]

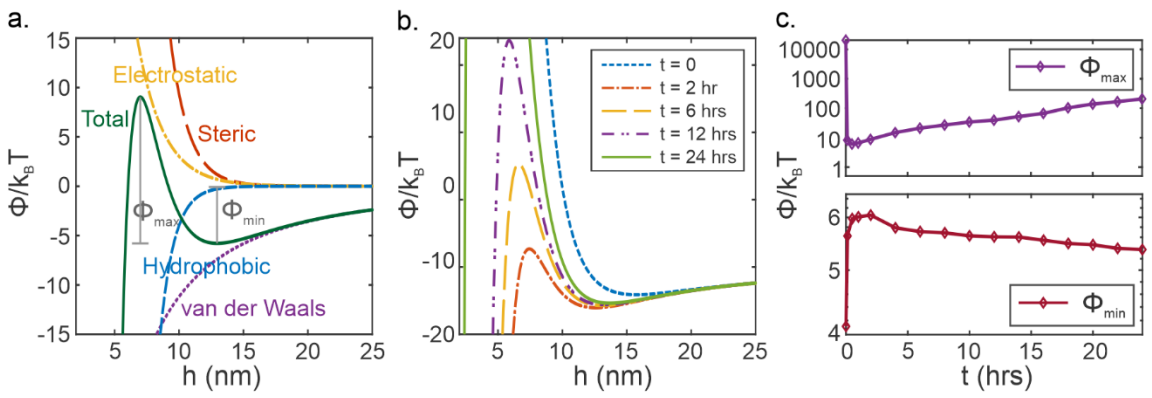

Figure 2.6. Pairwise interaction potential of 1 µm polystyrene particles at different time points after addition of 10 mM EDC. (a) Contribution of different interparticle interactions to the total pairwise interaction potential 4 hours after adding EDC. (b) Total interaction potential curve as a function of time over the dissipative assembly cycle. (c) Primary maximum height (top) and secondary minimum depth (bottom) as a function of time.

Figure 2.6a shows the contribution of each colloidal interaction to the total pairwise interaction potential for 1 μm particles 4 hours after adding EDC at an initial concentration of 10 mM. At a zeta potential value of –28.6 mV and Hydra parameter of 0.50, the secondary energy minimum depth was $\Phi_{min} = 5.8$ k_BT and primary maximum height was $\Phi_{max} = 14.8$ k_BT. **Figure 2.6b** shows how the pairwise interaction potentials evolved with time during dissipative assembly while **Figure 2.6c** shows how the secondary minimum depth and primary maximum height changed with time. In the model, the ionic strength of the solution was increased after addition of fuel to include the urea byproduct from the fuel reaction (EDU), which decreased the Debye length and repulsive double layer forces irreversibly (**Appendix A1**). Prior to addition of chemical fuel, the colloids exhibited stability due to large repulsive electrostatic interactions, with a relatively shallow secondary minimum depth of 4.1 k_BT and large primary maximum exceeding 10^4 k_BT.

After 2 hours the colloids were at their least stable state with the secondary minimum depth increased to 6.0 k_BT and the primary maximum height decreased to 8.7 k_BT. One thing to note here is that the hydrophobicity of the particles was highest immediately after EDC addition while the zeta potential reached a minimum about 2 hours after adding EDC (*cf.* **Figure 2.4**). The primary maximum height reached the smallest value about 30 minutes after fuel addition, suggesting this potential landscape feature was predominantly controlled by hydrophobic interactions. Interaction potential calculations performed without hydrophobic interactions further supported their importance to reconciling the model with experiments. These interaction potentials showed ~1000 k_BT primary maximum values at all fuel concentrations and times due to the strong electrostatic and steric repulsion interactions. Likewise, the secondary minima without hydrophobic interactions showed minimal recovery back to initial levels without including hydrophobic interactions.

The secondary minimum depth was sensitive to electrostatic repulsion as it reached a maximum after 2 hours, in line with the time corresponding to the minimum zeta potential magnitude. Estimation of interaction potential without hydrophobic interactions confirmed these findings where primary maximum seemed to heavily depend on the hydrophobic interactions and the effect of hydrophobic interactions on secondary minimum was insignificant (**Figure A1**). The secondary minimum at different time points with or without hydrophobic interactions were similar whereas the primary maximum remained > 7500 k_BT at all times without hydrophobic interactions. As time progressed beyond 1 hour after fuel addition the primary maximum increased monotonically to 21.7 k_BT after 6 hours, but the secondary minimum depth displayed a modest decrease in magnitude to 5.7 k_BT. The

primary maximum increased monotonically from 21.7 k_BT at 6 hours to 207 k_BT after 24 hours. Over the same time period, the secondary minimum depth decreased from 5.7 k_BT to 5.4 k_BT. The minimal decrease of the secondary minimum depth after 24 hrs disagrees with the experiments, which showed only a small number of aggregates remaining after 24 hours. While the zeta potential recovered to nearly the same value as prior to EDC addition, the ionic strength irreversibly increased by approximately 10 mM after adding EDC (**Appendix A1**). This irreversible change in ionic strength leading to irreversible decrease in particle stability is consistent with previous observations that showed buildup of EDU in solution eventually prevented dissipative assembly from occurring.[40]

While this model did not show complete quantitative agreement with experiments, it qualitatively agreed with several experimental observations. First, the model showed the secondary minimum depth increased 2 – 3 hours following fuel addition and then monotonically decreased, which agrees with the increase in aggregate count for several hours followed by a monotonic decrease in their number. Secondly, the model showed that when the particles were at their most unstable there was a primary maximum of about 6.1 k_BT, in agreement with the experiments showing formation of almost no irreversible aggregates. Finally, the secondary minimum depth was 4 – 6 k_BT during dissipative assembly, which agrees with observations of weak colloidal bonds in aggregates. Potential reasons for the lack of complete quantitative agreement between experiments and the model include additional interparticle interactions in the experimental system that could not be quantified and included in the model, such as acid-base interactions,[209] changes to the Flory Huggins interaction parameter of the surface polymer ligands after fuel addition, and effects of colloid surface roughness on interparticle interactions.[210]

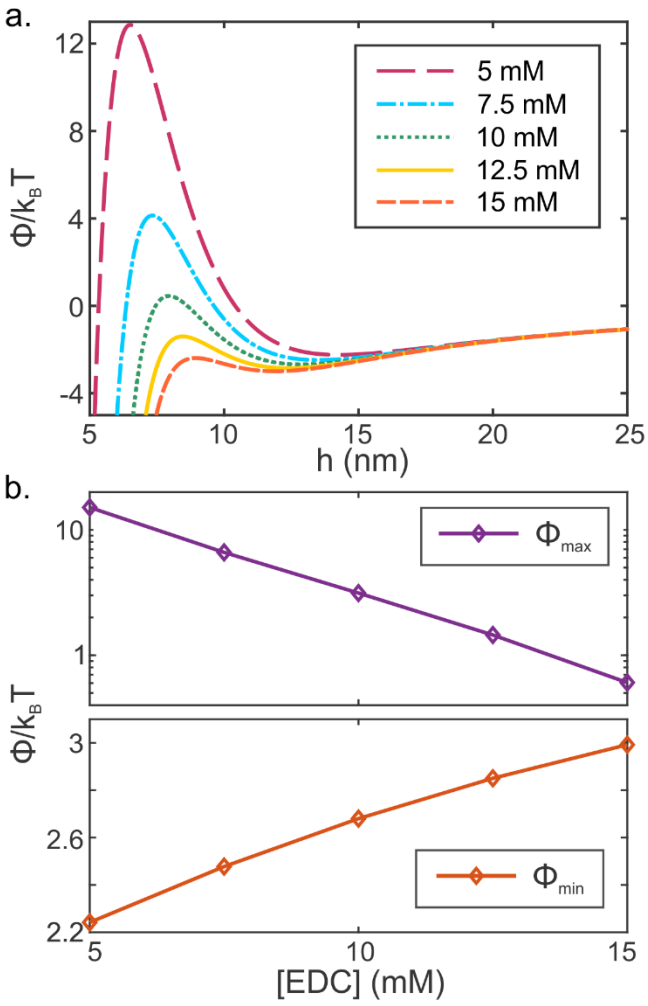

Figure 2.7. Interaction potential of 500 nm polystyrene at their most unstable point during dissipative assembly. (a) Interaction potential as a function of fuel concentration. (b) The primary maximum height and secondary minimum depth as a function of EDC concentration.

We applied the pairwise interaction potential model to interpret the effect of EDC concentration on dissipative assembly as shown in **Figure 2.3** (**Figure 2.7**). Here we used zeta potentials and Hydra parameters corresponding to when the particles were most unstable, *i.e.*, about 2 hours after adding EDC (*cf.* **Figure 2.4a, Figure 2.5c** and **Figure**

A2). The rationale for utilizing these values is that primary maxima and secondary minimum > 1 k_BT when the particles were at their most unstable suggests the particles will undergo reversible assembly in the secondary minimum. However, if the primary maximum is < 1 k_BT at this point then the particles are expected to irreversibly aggregate. **Figure 2.7a** shows that the secondary minimum depth increased as a function of increasing EDC concentration, consistent with the experimentally observed increase in aggregate concentration up to 10 mM EDC (*cf.*, **Figure 2.3**). **Figure 2.7b** shows there was a secondary minimum for all EDC concentrations and that a primary maximum > 1 k_BT existed for initial EDC concentrations < 13.7 mM, consistent with the experimental range of fuel concentrations that effected dissipative assembly. Above 13.7 mM initial EDC concentration, the model predicts that any aggregates formed in the secondary minimum will rapidly convert to irreversible aggregates due to the small energy barrier, consistent with irreversible aggregation seen at 15 mM EDC concentration. Removal of hydrophobic interactions from the interaction potential resulted in large primary maxima heights (above 3800 k_BT) for all EDC concentrations, which disagreed with our experimental observations of irreversible aggregation at higher EDC concentrations and further indicated the importance of these interactions (**Figure A3**).

2.3.3.4. Broader implications for dissipative assembly of colloids

A key finding of this work is that dissipative colloid assembly experiments can be reconciled with equilibrium pairwise interaction potential models despite the non-equilibrium nature of fuel driven assembly. The interparticle interaction model developed here showed quantitative agreement with some aspects of the experiments, such as the range of EDC concentrations leading to dissipative assembly, and qualitative agreement

with others, such as the non-monotonic change in secondary minimum over time and the weak interparticle bonds in aggregates formed by dissipative assembly. Pairwise interaction potential models together with time dependent measurements of colloid surface chemistry can enhance our understanding of how fuel-ligand reactions affect colloidal interactions during dissipative assembly and assist in rational design of a dissipative assembly process. In particular, we found that colloidal interactions that dictate the depth of the secondary minimum will control the aggregate concentration during dissipative assembly. In this study, the time dependent repulsive electrostatic interactions were found to mediate the secondary minimum depth and thus the relative concentration of aggregates formed. Decreased zeta potential magnitude led to a deeper secondary minimum and increasing aggregate concentration as a function of increasing fuel concentration, except for 12.5 mM initial fuel concentration. This work highlights the importance of identifying which colloidal interactions that control the depth of the secondary minimum. It is possible that in other systems different colloidal interactions will dictate the secondary minimum depth and position, such as depletion forces,[211] and in that case the strength of those interactions will control the aggregate concentration during dissipative assembly. Secondly, this work showed that time dependent hydrophobic interactions, independent of electrostatics, controlled the primary maximum height during dissipative assembly and therefore determined whether the colloids would irreversibly aggregate. This is important because hydrophobic interactions can be tuned independent of electrostatics, for instance by adding chaotropic agents, hydrotropes, or nonionic surfactants to screen nonpolar surface moieties on colloids. These molecules can be added to the solution, taking care to avoid reactivity with the chemical fuel, to finely tune hydrophobic interactions. While in

this case it was not necessary to add these molecules to achieve dissipative assembly, experiments showed that adding non-ionic surfactants to solution prevented dissipative assembly of colloids, ostensibly by screening hydrophobic attraction (**Figure A3**). Ultimately, this work indicates that many design rules developed for near-equilibrium self-assembly can be applied to dissipative assembly, albeit with the added complexity that the interparticle interactions are time-dependent.

Moving beyond dissipative assembly of disordered colloidal aggregates to form transient ordered colloidal structures, such as colloidal molecules,[192] microrobots,[212] and superlattices,[213] represents a significant challenge and will require intimate understanding of the dynamic colloid surface chemistry and interparticle interactions during dissipative assembly. Ordered colloidal assemblies often require directional interparticle interactions, which will require development of more complex interaction potential models. Directional interactions are less kinetically favored, meaning colloids require longer annealing times to assemble into the favored spatial configuration. This will necessitate fuel reaction cycles that activate colloids into an assembly prone state for prolonged periods of time as opposed to generating a short-lived spike in activated colloid concentration as demonstrated in this work. Experimental measurements of surface hydrophobicity demonstrated here will aid in designing new reaction cycles that yield sustained constant activation without inducing irreversible aggregation.

2.4 Conclusions

This work reconciled the dissipative assembly and irreversible aggregation of micron sized colloids due to carbodiimide fuel addition with dynamic surface chemistry and equilibrium pairwise interparticle interactions. Microscopic observations of colloidal

aggregated demonstrated distinct differences in morphology with aggregates formed by dissipative assembly were loosely packed with weak interparticle bonds, while irreversible aggregates were fractal in nature with strong interparticle bonds. A fluorescence assay was developed to quantify the time dependent hydrophobicity and hydrophobic interactions between colloids undergoing dissipative assembly. The interaction potentials estimated from the time dependent zeta potential and hydrophobicity at different conditions qualitatively agreed with the microscopic observations and elucidated that electrostatic repulsion and hydrophobic attraction control different aspects of dissipative assembly. This work has several implications for dissipative assembly of colloids. The number of successful studies of dissipative assembly of small molecules and polymers significantly outnumbers those focused on micron sized colloids and nanoparticles. This work, together with prior work by other labs, emphasizes the importance of characterizing colloid surface chemistry and interparticle interactions to establish appropriate fuel reaction conditions for dissipative assembly. In particular, a delicate balance must be struck between the time scale of the fuel-ligand reactions, the dynamics of the surface chemistry, and the resulting attractive and repulsive forces, and the assembly kinetics.

Chapter 3. Revealing Reactions between the Electron Beam and Nanoparticle Capping Ligands with Correlative Fluorescence and Liquid-Phase Electron Microscopy[†]

3.1 Introduction

Self-assembly of colloidal nanoparticles enables constructing intricate nanostructures and macroscopic materials that cannot be realized by top-down processing.[214,215] Self-assembly of nanoparticles is a complex process in which both thermodynamics and kinetics play important and intertwined roles in determining the final self-assembled structure.[216] Liquid phase transmission electron microscopy (LPTEM) can uniquely visualize the dynamics of nanoparticle self-assembly in a liquid medium in real time with nanometer scale resolution. Numerous LPTEM studies have investigated self-assembly of nanoparticles functionalized with small molecules, polymers, and DNA capping ligands.[122,136–141,150–153,157,159,217–220] Interparticle interactions during self-assembly, including steric forces, electrostatic forces, hydrogen bonding, and hydrophobic/hydrophilic forces are mediated by the specific physicochemical properties (*e.g.* molecular weight, ligand density, functional groups, protonation/deprotonation) of organic surface ligands on nanoparticles.[1,214] It is well known that the TEM beam strongly interacts with organic molecules through radiolysis reactions.[166,221] However, despite the importance of organic capping ligands in self-assembly and their susceptibility to electron beam damage,[169] few LPTEM studies have focused on electron beam damage mechanisms

[†] Note: This chapter was previously published by Dissanayake et al. and reproduced here with minor modifications: Dissanayake, T.U., Wang, M., Woehl, T.J., "Revealing Reactions Between the Electron Beam and Nanoparticle Capping Ligands with Correlative Fluorescence and Liquid – Phase Electron Microscopy", *ACS Appl. Mater. Interfaces*, **2021**, 13 (31), 37553–37562.

of organic capping ligands. To correctly interpret self-assembly dynamics and mechanisms observed with LPTEM, it is imperative to understand how the electron beam modifies nanoparticle surface ligands and to establish limits on the electron doses and dose rates used to image nanoparticle self-assembly.

The electron beam creates highly reactive radicals through solvent radiolysis during LPTEM imaging. For instance, radiolysis of water creates both strongly reducing radicals, aqueous electrons (e_{aq}^{-}) and hydrogen radicals ($H^{\cdot}$), and oxidizing hydroxyl radicals ($OH^{\cdot}$), which can react with organic molecules.[165,166] While electron beam-sample interactions have been extensively studied in terms of general radiolysis reactions and formation of metal nanocrystals,[122,222] little work has been performed to understand how these radical reactions impact organic capping ligands. The radiation chemistry field has shown that radicals readily react with organic molecules and polymer through various redox processes.[223–232] Given the large number of LPTEM studies on self-assembly, the lack of systematic studies of electron beam reactions with nanoparticle surface ligands has prohibited discovery of acceptable "low dose" imaging conditions for LPTEM nanoparticle self-assembly experiments that produce minimal beam induced changes to nanoparticle surface chemistry.

Electron beam induced reactions during LPTEM are only perceptible if visible changes occur in the material being imaging, *e.g.*, growth/etching of nanoparticles,[233–238] dissolution of metal organic frameworks,[239] pitting of carbon nanotubes,[240] shrinkage of bacterial cells,[241] or formation of visible polymeric nanoparticles.[242] Nanoparticle surface ligands are not observed during LPTEM due to their small size (typically < 2 nm ligand layer thickness) and low image contrast compared to inorganic nanoparticles. Even if

ligands can be visualized with state-of-the-art aberration corrected or graphene liquid cell TEM, LPTEM images provide no information about the chemical structure of the ligands. In this article, we employ fluorescent probes and correlative fluorescence microscopy (FM) to establish the fate of excess and absorbed capping ligands during LPTEM imaging. Our results show that polymer crosslinking and chain scission occur during LPTEM imaging, leading in some cases to a non-monotonic time dependent change in ligand thickness on the nanoparticles and the silicon nitride membrane surface. The results emphasize the magnifying effect of high atomic number nanoparticles on local radiation damage, in agreement with a recent report,[242] and the effectiveness of radical scavengers in mitigating electron beam damage. We expect this method can be applied to other nanoparticle surface ligands as well as biomolecules by drawing from the extensive library of conjugation reactions developed for conjugating fluorophores to biomolecules.

3.2. Methods

3.2.1. Preparation of nanoparticles and LP-TEM samples

An aqueous suspension of 100 nm BPEI coated silver nanoparticles was purchased from nanoComposix (San Diego, USA). BPEI covalently bonds to the surface of silver nanoparticles *via* amine-metal binding with an approximate grafting density of 0.05 molecules/nm^2 (calculated based on a ~1 nm ligand shell thickness observed in TEM images). The silver nanoparticles were centrifuged and washed with DI water two times to remove excess ligands and contaminants. Liquid cell silicon nitride chips (Protochips) with 500 µm × 50 µm silicon nitride windows and 500 nm gold spacers were rinsed consecutively with acetone and methanol and were treated with an air plasma for 2 minutes

to render them hydrophilic and remove residual organics. Three 5 µl drops of silver nanoparticles were consecutively air dried on the silicon nitride windows of both top and bottom chips **(Figure 3.1**, step 1). The membranes were rinsed with DI water after nanoparticle deposition. For experiments using only BPEI ligands, the twice cleaned nanoparticle solution was centrifuged a third time and three 5 µl drops of clear supernatant were air dried on the silicon nitride membranes. The silicon chips were assembled dry in the liquid cell holder (Protochips) and HPLC grade water was flowed into the cell using a syringe pump (Harvard Apparatus) at a rate of 300 µl/h **(Figure 3.1** step 2). For experiments with radical scavenger, 1 M tert-butanol in HPLC grade water was flowed into the cell.

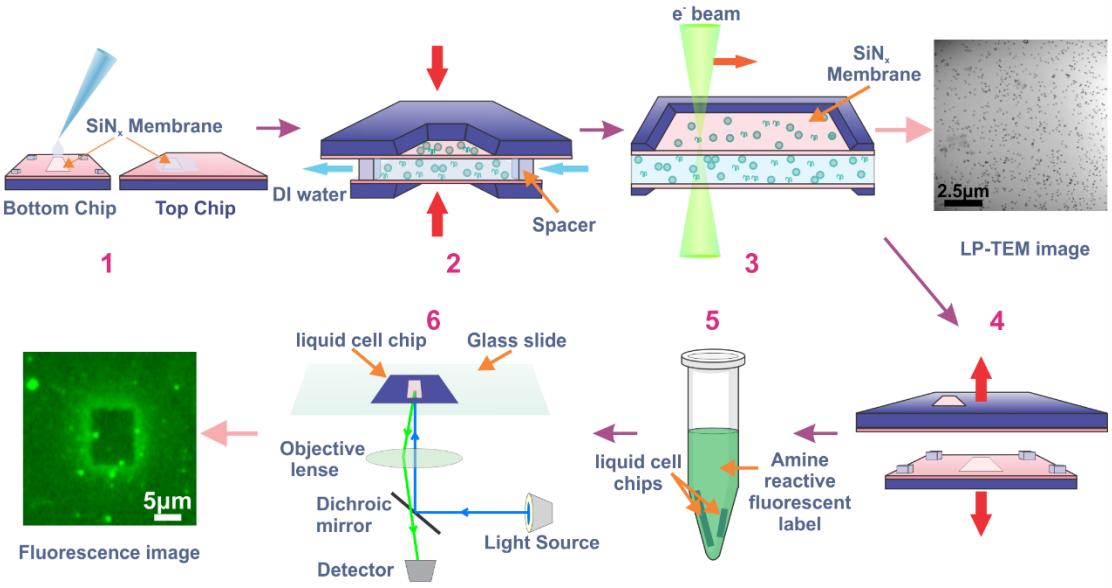

Figure 3.1. Summary of the method for correlative LPTEM and FM visualization of capping ligand damage. (1) Silver nanoparticles were drop cast and dried onto cleaned silicon nitride membranes, which were (2) assembled in the liquid cell. (3) Various regions of the sample were imaged in the TEM under different conditions. (4) The sample was disassembled after removing from the TEM and (5) the BPEI ligands were fluorescently

labeled by incubating with amine reactive fluorescent molecules. (6) The chips were imaged with FM to visualize electron beam induced reactions with BPEI ligands.

3.2.2. LP-TEM experiments

LPTEM imaging was performed in a JEOL JEM-2100F field emission electron microscope operating at 200 kV in STEM mode at a magnification of 20,000x. After focusing and rotating the beam to align with the edge of the silicon nitride membrane, the sample was translated to one corner of the silicon nitride membrane. Different regions of the silicon nitride membrane were irradiated at electron fluxes ranging from 0.032 - 0.138 $e^-/Å^2$ s (dose rate of 0.144 – 0.616 MGy/s) for 30 s - 10 min **(Figure 3.1**, step 3). The spaces between each irradiated area were systematically varied to create an easily identifiable pattern in the FM image to correlate each irradiated area with the respective exposure time and dose. Other than to demonstrate how the electron beam reacts with ligands while translating, rotating, or focusing the sample, the electron beam was blanked when moving to a new region using an electrostatic blanker. LPTEM images showed nanoparticles were deposited onto the membrane surface as single particles and aggregates (**Figure 3.1**, top right). The liquid cell was disassembled carefully after the LP-TEM experiment and silicon chips were removed from the holder with the silicon nitride windows intact (**Figure 3.1** step 4).

3.2.3. Fluorescence labeling of samples and fluorescence microscopy

A 10 mg/ml stock solution of fluorophore was prepared by dissolving 2 mg of 6-[Fluorescein-5(6)-carboxamido]hexanoic acid (Sigma) in 200 µl of dimethyl sulfoxide (DMSO). 25µl of 16mg/ml 1-Ethyl-3-(3-dimethylaminopropyl)carbodiimide (EDC,

Thermo Scientific), and 25 µl of 44 mg/ml N-hydroxysulfosuccinimide (Sulfo-NHS, Thermo Scientific) were added to 100 µl of the fluorophore stock solution and left to react for 15 minutes at room temperature to form an amine reactive fluorophore. After that, 0.28 µl of 2-Mercaptoethanol (Thermo Scientific) was added to the fluorescein – EDC – NHS solution and incubated for 5 minutes to quench excess EDC in the solution. The disassembled top and bottom liquid cell chips were placed in 425 µl of DI water in a centrifuge tube and 75 µl of fluorescein – EDC – NHS solution was injected. The reaction between the amine reactive fluorophore and primary amine groups on the BPEI molecules proceeded for 1 hour after which the chips were washed 3 times with DI water **(Figure 3.1**, step 5). The cleaned chips were dried using compressed air and placed on a clean cover slip. FM was performed in an inverted optical microscope (ZEISS Axio Observer) with a 40x dry objective lens **(Figure 3.1**, step 6). All the FM images in this study originated from the top chip of the liquid cell in each experiment because this is where the electron beam was focused during LPTEM. FM images were processed and analyzed using ImageJ.[243] Silicon nitride membrane fluorescence intensity profiles were measured along lines draw across the image area with each intensity divided by the background fluorescence intensity immediately outside the image area. Fluorescence intensities of nanoparticles were determined by measuring the average intensity of each nanoparticle.

We labeled the BPEI capping ligands after the sample was imaged and removed from the TEM to avoid electron beam damage to fluorescent molecules, which can extinguish their fluorescence emission. The FM images provided a snapshot of the local relative BPEI ligand thickness for a given LPTEM imaging time and cumulative dose. Benchtop control experiments varying the thickness of polymer layers on flat silicon

substrates were performed to validate the method. A solution of fluorescein labeled BPEI was serially diluted to various polymer concentrations and dried on silicon chips to create samples with linearly varying BPEI thicknesses. FM images were taken of each sample and average fluorescence intensity measurements were linearly proportional to the BPEI solution concentration (**Figure A4**), and thus linearly proportional to the local thickness of BPEI on the surface.

3.3. Results

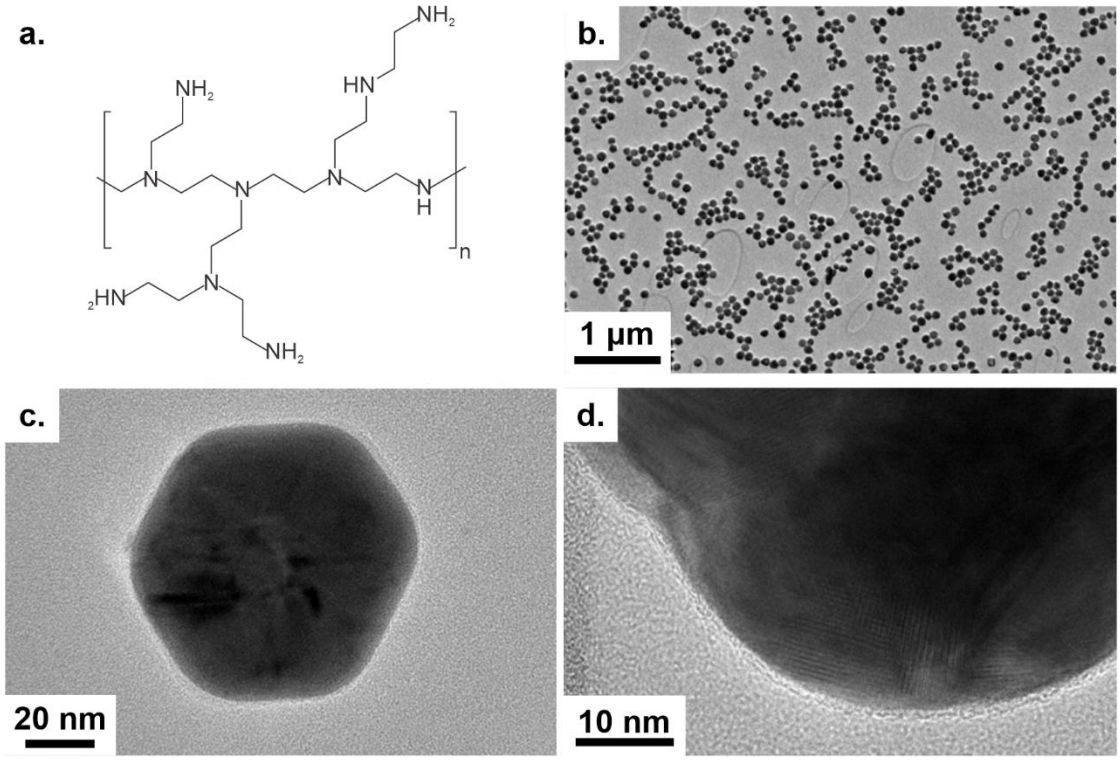

Figure 3.2. Branched polyethylenemine (BPEI) and TEM images of silver nanoparticles in the dry state. (a) Molecular structure of BPEI. (b) Low magnification TEM image of BPEI coated silver nanoparticles. (c) HRTEM image of a single nanoparticle showing the particle shape. (d) HRTEM image showing the BPEI ligand layer on a polycrystalline silver nanoparticle.

Systematic dose rate controlled LPTEM experiments probing electron beam reactions with nanoparticle capping ligands were performed on 100 nm diameter silver nanoparticles coated with 25,000 g/mol BPEI, which contains primary, secondary, and tertiary amine groups that imbue the nanoparticle surfaces with a positive charge (**Figure 3.2a**). TEM images of the silver nanoparticles in the dry state showed they were either spherical or faceted, polycrystalline, had a monomodal size distribution (**Figure 3.2 b,c**), and were coated by a ~1 nm thick BPEI ligand layer (**Figure 3.2d**). Due to the low spatial resolution of the FM images (~500 nm), low magnification (M = 20,000 x) scanning TEM mode (STEM) was used for all LPTEM experiments to create a large irradiated region on the order of 10 μm that could be visualized with FM. Within each irradiated area, each nanoparticle or nanoparticle aggregate was exposed to a uniform dose rate and cumulative electron dose. In this article, we report the dose rate in units of Grays per second (Gy/s), which is the product of the area averaged electron flux (electron beam current divided by the image area size) and stopping power of water (2.798×10^5 eV.m^2/kg), following previously established methods.[122,235] Cumulative doses given in each figure were calculated by multiplying the dose rate by the total irradiation time. We note that electron fluxes (0.032 - 0.138 $e^-/Å^2s$) and cumulative electrons delivered (1 – 80 $e^-/Å^2$) used here are generally considered to be "low dose" conditions used for imaging electron beam sensitive polymers and biomolecules with LPTEM and cryo-EM.[145,148,244,245]

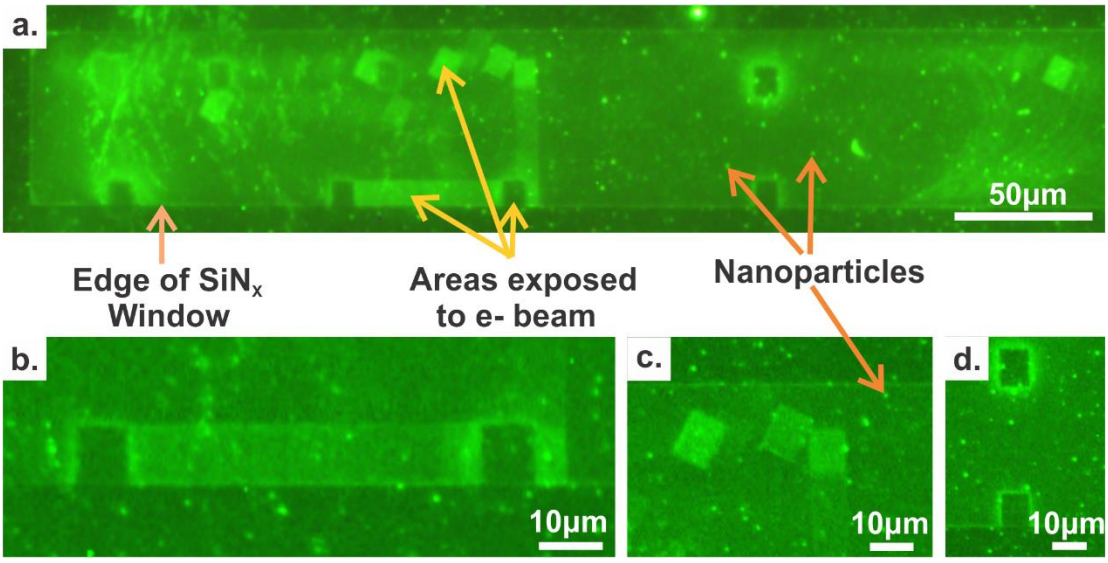

Figure 3.3. Exemplary FM images of a fluorescent labeled silicon nitride membrane after an LPTEM experiment. The green fluorescence intensity shows the relative local thickness of BPEI ligand. (a) Survey image of the silicon nitride membrane showing various fluorescent features created by presence of nanoparticles and electron beam exposure. (b) Sample translation during LPTEM with continuous imaging created pathways of bright fluorescence intensity due to brief (seconds) electron beam exposure. (c) STEM scan rotation can be observed by a change in the angle of the bright fluorescent square image regions. (d) Different exposure times and cumulative doses created image regions with different fluorescence intensity compared to the background.

FM images showed background fluorescence across the silicon nitride surface from adsorbed BPEI ligands, while silver nanoparticles and nanoparticle aggregates appeared as bright fluorescent spots above the background (**Figure 3.3a**). Some sample regions had bright fluorescence and nanoparticle coverage due to evaporation induced aggregation of nanoparticles (left side of **Figure 3.3a**); these regions were not considered in quantitative analyses. Sample regions irradiated by the electron beam were clearly distinguished as

bright or dark square regions with sizes roughly equal to the STEM image size. Two characteristic features were immediately evident in the FM images (**Figure 3.3a**). The first feature was squares or tracks across the membrane surface that were brighter than the background; these regions corresponded to image regions irradiated with the electron beam for < 30 s during focusing, sample translation (**Figure 3.3b**), or image rotation (**Figure 3.3c**). We did not know the exact irradiation time for these as the shortest timed irradiation was 5 minutes, but these image manipulations typically took ≤ 30 s. Nanoparticles in these regions had brighter fluorescence intensity than non-irradiated nanoparticles. The second type of fluorescent feature observed was image areas that were similar intensity or darker than the background intensity and surrounded by a bright fluorescent halo and corresponded to image regions irradiated for > 5 minutes (**Figure 3.3d**). Nanoparticles within these dark regions had lower fluorescence intensity compared to those in the bright irradiated regions and unirradiated regions. In most cases, nanoparticles remained immobile on the silicon nitride membranes throughout the irradiation experiments and no beam induced nanoparticle aggregation was observed. At a relatively high dose rate of 0.616 MGy/s, some nanoparticles moved into the image area in the first few seconds after which they were immobile for the rest of the irradiation, indicating they received a nearly identical cumulative dose compared to the initially present particles (**Figure A6**).

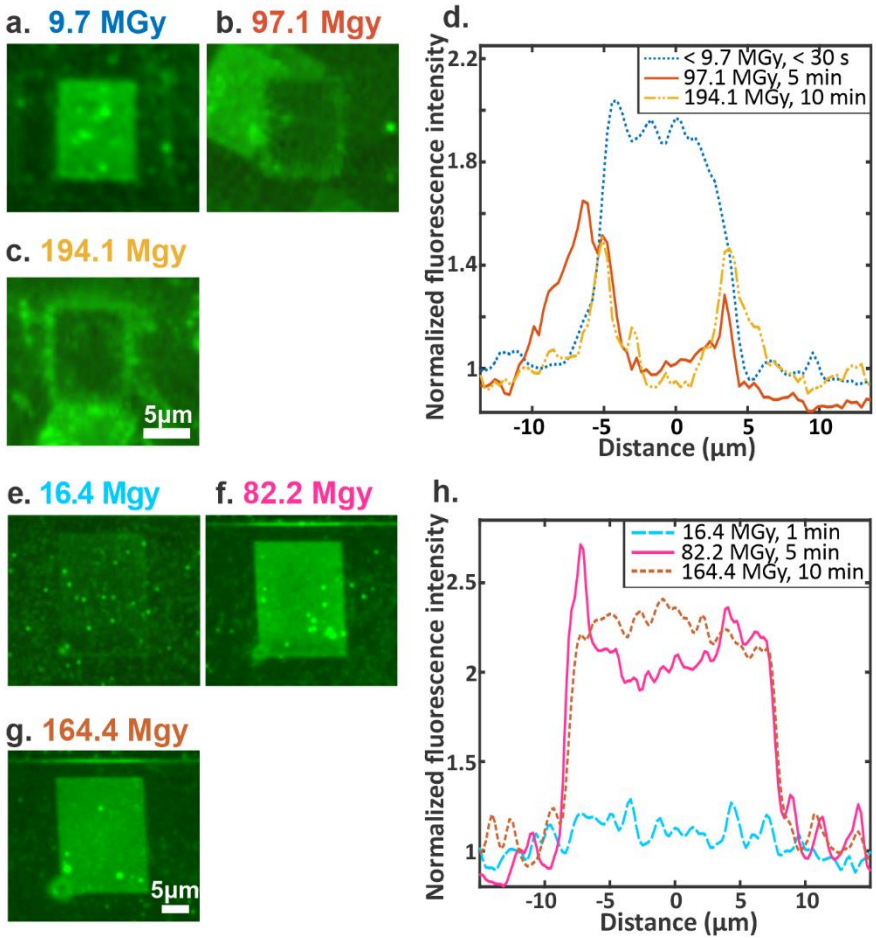

Figure 3.4. Effect of cumulative dose on the fluorescence intensity of the silicon nitride membrane with (a)-(c) and without (e) – (g) silver nanoparticles deposited on the membrane. (a) – (c) FM images of irradiated sample regions with BPEI coated nanoparticles irradiated at a dose rate of 0.324 MGy/s for times of (a) < 30 s, (b) 5 minutes, and (c) 10 minutes. (d) Fluorescence intensity measured along a horizontal line drawn across the center of each irradiation region in (a)-(c). (e) – (g) FM images of irradiated sample regions with only BPEI ligands irradiated at a dose rate of 0.274 MGy/s for times of (e) 1 minute, (f) 5 minutes, and (g) 10 minutes. (h) Fluorescence intensity measured along a horizontal line drawn across the center of each irradiation region in (e) – (g). The

fluorescence intensity of each irradiated region was normalized to the local background intensity.

All regions irradiated for < 30 seconds were brighter than the non-irradiated surrounding area (**Figure 3.4a**), while those irradiated for > 5 minutes were either lower intensity or similar intensity compared to the background (**Figure 3.4b,c**). For the longer irradiation times, the intensity inside the irradiated regions and the intensity of the surrounding fluorescent halo showed no trend with cumulative dose (**Figure 3.4d**). We did not observe any effect of the dose rate on the qualitative effects of LPTEM irradiation, as irradiating a sample at a dose rate of 0.616 MGy/s yielded a similar sequence of events as the lower dose rate (**Figure A7**). To test the effect of nanoparticles on the electron beam damage to the ligands, we irradiated a separate sample containing only excess soluble BPEI capping ligand. The sample regions exposed to the electron beam for 1 minute were barely discernible (**Figures 3.4e**). In contrast to the experiments with nanoparticles present, bright fluorescence intensity was observed in image regions irradiated for 5 (82 MGy) and 10 minutes (164 MGy) (**Figures 3.4e-g**). The fluorescence intensity of the silicon nitride increased by ~10% between the 5 minute and 10 minutes irradiations (**Figures 3.4h**).

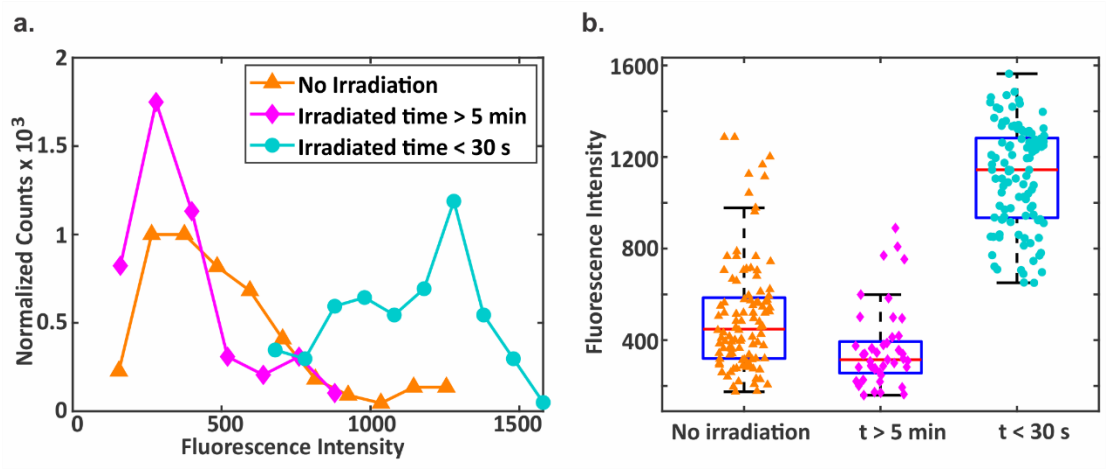

Figure 3.5. Fluorescence intensity distributions of silver nanoparticles after electron beam exposure in DI water. Intensity data were measured from the sample regions shown in **Figure 3.3**. (a) Probability distribution functions of silver nanoparticle fluorescence intensities for particles that were not irradiated (orange triangles), irradiated for < 30 s (< 9.7 MGy, cyan circles), and irradiated for > 5 minutes (> 97.1 MGy, pink diamonds). (b) Box plots of nanoparticle fluorescence intensities for each condition. Wilcoxon rank-sum tests showed there were statistically significant differences between each fluorescence intensity distribution ($P < 0.005$). Fluorescence intensities of 104, 45, and 105 particles were measured from the regions of no irradiation, irradiation for > 5 minutes, and irradiation for < 30 seconds, respectively.

In addition to changing the fluorescence intensity of the membrane surface, irradiation during LPTEM modified the fluorescence intensity, and thus the ligand coverage, of silver nanoparticles compared to non-irradiated areas. Nanoparticles displayed a distribution of fluorescence intensities due to variations in initial ligand coverage, particle size, and particle aggregation, so we performed a statistical analysis of the effect of cumulative dose on nanoparticle fluorescence intensity (**Figure 3.5**). Measurements of nanoparticles intensities were merged for all < 30 sec irradiation areas

and all > 5 min irradiation areas shown in **Figure 3.3a** to gain statistically significant population sizes (> 40 particles per data set). Histograms of individual particle fluorescence intensities showed the nanoparticle intensity distribution for regions irradiated for > 5 minutes was lower overall compared to unirradiated regions, while nanoparticles irradiated for < 30 seconds had overall larger fluorescence intensities (**Figure 3.5a**). A statistical comparison of intensity distributions revealed that each intensity distribution was statistically different (for $P < 0.005$) (**Figure 3.5b**). The changes in the nanoparticle fluorescence intensities with cumulative dose therefore mirrored those of the silicon nitride membranes, indicating that similar chemical processes controlled ligand damage on the silicon nitride and silver nanoparticles.

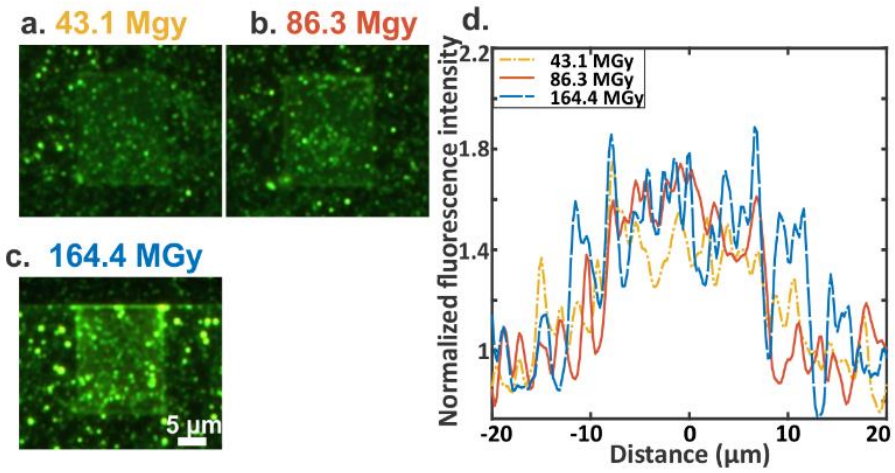

Figure 3.6. The fluorescence intensity of irradiated silicon nitride regions for a nanoparticle sample containing 1 M tert-butanol. (a) – (c) FM images corresponding to image areas irradiated at a dose rate of 0.144 MGy/s for times of (a) 5 minutes and (b) 10 minutes and irradiated at a dose rate of 0.274 MGy/s for (c) 10 minutes. (d) Fluorescence intensity measured along a horizontal line drawn across each irradiated region in (a) – (c).

Prior works have established that alcohols, such as isopropanol and tert-butanol, and other organic molecules can act as hydroxyl radical scavengers to mitigate radiation damage to organic molecules during LPTEM imaging.[113,146,167,242,246] We added 1 M tert-butanol in DI water as a radical scavenger to test its impact on electron beam damage of BPEI in the presence of silver nanoparticles (**Figure 3.6**). Similar to the experiment without any nanoparticles, there was no visible change in fluorescence intensity in the image regions exposed for 30 seconds and 1 minute at a dose rate of 0.274 MGy/s. Compared to samples with no tert-butanol irradiated for > 5 min, which showed decreased fluorescence intensity, a small increase in fluorescence intensity compared to background was observed at similar irradiation times for the nanoparticle sample containing tert-butanol (**Figure 3.6a-c**). The largest fluorescence intensity of the sample region irradiated with tert-butanol present (≈ 1.6) was smaller than the sample with no tert-butanol (≈ 2) after being irradiated with 10 times less cumulative dose.

3.4. Discussion

The electron beam indirectly reacts with soluble and nanoparticle surface adsorbed polymers in aqueous solution *via* radicals formed by water radiolysis, including oxidizing hydroxyl radicals ($OH^{\cdot}$), reducing hydrogen radicals ($H^{\cdot}$), and reducing aqueous electrons (e^{-}_{aq}).[166,230,247] Hydroxyl radicals readily react with polymers by abstracting hydrogen atoms from the main carbon chain and amine groups, which forms reactive radicals that either undergo intramolecular or intermolecular crosslinking or serve as intermediates to carbon-carbon chain scission reactions.[168] Radiation induced crosslinking reactions have been utilized to form hydrogels and bulk polymers by irradiating both solid phase and liquid phase precursors.[168,230,248,249] While each of the three reactions occur simultaneously,

the dominant reaction is influenced by polymer chemistry, molecular weight, concentration, dose rate, and cumulative dose. The fluorescence labeling approach used in this study distinguishes between intermolecular crosslinking (enhanced local fluorescence intensity with electron irradiation) and chain scission (reduced local fluorescence intensity with electron irradiation), but cannot readily identify intramolecular crosslinking, which will change the local ligand layer thickness but not the fluorescence intensity. However, because the polymer used here is 25,000 g/mol, which is a relatively low molecular weight, we expect intermolecular crosslinking to dominate over intramolecular crosslinking.[232] Based on these reactions, we interpreted irradiated regions that were darker compared to the background as those where chain scission reactions dominated for the given cumulative dose, while brighter fluorescent regions experienced net intermolecular crosslinking.

In addition to radical reactions, we also considered the effect of electric fields on the deposition/removal of BPEI ligands from the image area. It is well known that the thin solid silicon nitride membranes emit secondary electrons during LPTEM imaging, which can induce a positive charge on the membrane.[135] Positive charge on the silicon nitride gives rise to a divergent electric field inside the liquid directed away from the irradiated region of the membrane into the bulk liquid.[250] If this field is sufficiently strong, it could impact the attachment of BPEI to the negatively charged silicon nitride membrane as well as the transport of the positively charged polymer in solution. Recent studies have provided conflicting estimates of the local electric field and membrane potential during LPTEM. The electron beam induced membrane potential was estimated to be +2 mV by prior Monte-Carlo scattering simulations.[222] The silicon nitride-water interface has a zeta potential of about -30 mV near neutral pH, so this beam induced surface potential would

not significantly affect the overall membrane surface potential. Another recent study concluded that there will be no appreciable electric field in the system due to charge screening at the solid-liquid interface.[164] However, several other studies suggested more significant electric fields form due to beam induced charging, but did not offer any practical estimates of their magnitudes in the presence of liquid.[250,251] The observation that the solution chemistry and cumulative dose, and not the dose rate (which controls the magnitude of electron beam charging[251]), controlled whether ligand was added or removed from the irradiated area suggests that radiation chemistry mediates the observed phenomena and not beam induced charging. However, due to the lack of comprehensive studies on electric fields during LPTEM we cannot completely disregard electric fields and acknowledge that they could affect polymer transport in solution and local radical concentrations.

Positively charged nanoparticles and free BPEI ligand initially dried onto the negatively charged silicon nitride surface physisorbed by electrostatic interactions. Any loosely bound or entangled nanoparticles and polymers on top of this adsorbed layer become solubilized after water was introduced into the liquid cell. The adsorbed and soluble BPEI ligands reacted with radicals created by the electron beam and crosslinking and chain scission reactions proliferated. In DI water only, the fluorescence intensity of the silicon nitride membrane and nanoparticles locally increased after short irradiation times (~30 seconds) due to crosslinking of soluble BPEI to BPEI adsorbed to nanoparticles and the silicon nitride membrane. Previous work has shown that radical concentrations are elevated near the water – silicon nitride interface and near nanoparticle surfaces,[252] which enhances local production of BPEI radicals compared to bulk solution. The initial rate of

BPEI crosslinking reactions was higher than the rate of chain scission as evidenced by the increased fluorescence intensity. Over several minutes, soluble BPEI ligands were depleted by the crosslinking reactions and the hydrogen abstraction rate constant, which creates crosslinking sites, decreased due to the increasing BPEI molecular weight.[229] Moreover, electrostatic repulsion between similarly charged BPEI molecules could play a role in slowing the crosslinking reaction rate over time.[231] Due to the increase in the radical lifetime on BPEI molecules, resulting from the decreased free BPEI concentration and crosslinking reaction rates, chain scission reactions began to dominate over crosslinking, leading to decreased fluorescence intensity in the image regions irradiated for several minutes. While this method does not detect intramolecular crosslinking, it is possible the BPEI ligands crosslinked onto the surface underwent intramolecular crosslinking as alkyl radicals continued to form in close proximity. During the chain scission process, rupture of the bonds between BPEI and silver surface is not expected to be a significant reaction due to the abundance of reactive C – H and N – H bonds in BPEI polymers. We do not expect reactions between radicals and the polymer-nanoparticle or polymer-silicon nitride bonds to be significant due to their low abundance compared to the PEI repeat units. BPEI fragments from chain scission reactions did not crosslink again inside the image area but transported away and crosslinked outside the image area as apparent by bright halos surrounding the irradiated regions. In the absence of nanoparticles and when 1 M tert-butanol was included with the nanoparticles, BPEI ligands only displayed net crosslinking reactions across all doses and dose rates tested.

Recent studies showing amplification of electron beam damage and radical concentrations by high atomic number nanoparticles provide clues about the different

behaviors of nanoparticle laden, nanoparticle free, and radical scavenger laden samples. Korpanty *et al.* found that gold nanoparticles accelerated the radiation crosslinking of polyethylene glycol and found through modeling that nanoparticles enhanced the yields of hydroxyl and polymer radicals.[242] Prior numerical radiolysis simulations predicted that the local yield of radicals was several times higher near a metal – water interface compared to bulk liquid due higher yield of secondary and backscattered electrons from metals when irradiated.[252] In the field of radiation processing of bulk polymers, empirical evidence shows that crosslinking predominates at low cumulative dose while chain scission dominates at larger cumulative doses. This occurs because the yields for crosslinking and chain scission increase as a function of cumulative dose and the chain scission yield increases more rapidly.[248] Finally, prior simulations by Wang *et al.* found that addition of tert-butanol reduced the steady state hydroxyl radical concentration in water by several orders of magnitude.[113] Taken together, these prior studies suggest that silver nanoparticles created larger concentrations of hydroxyl radicals, which accelerated the electron beam damage process of crosslinking at low cumulative dose followed by chain scission at high cumulative dose. In the absence of nanoparticles or in the presence of tert-butanol, the hydroxyl radical concentration decreased, and crosslinking was the dominant reaction over the experimental time scales. In other words, the effective cumulative dose was higher with nanoparticles present and was lower in the absence of nanoparticles and with tert-butanol present. These results demonstrate that chain scission reactions, which will deplete the ligand shell and negatively affect the nanoparticle stability and potential to undergo self-assembly, could be avoided by using a radical scavenger or reducing nanoparticle concentration.

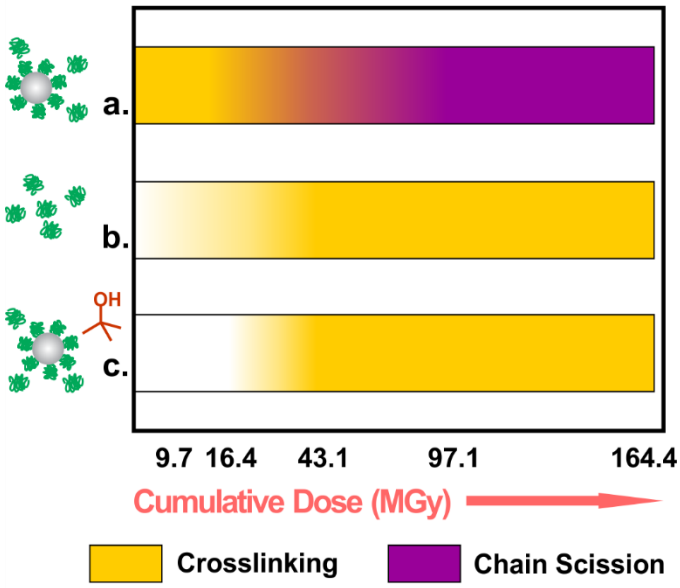

Figure 3.7. Qualitative schematic showing the prevalence of crosslinking and chain scission reactions in BPEI ligands as a function of cumulative dose as determined by FM for (a) a sample with nanoparticles and free ligands in DI water, (b) a sample with only free ligands in DI water and (c) a sample with nanoparticles and free ligands in 1 M aqueous tert-butanol. In sample (a) the exact crossover point from crosslinking to chain scission was unknown but occurred between 16.4 – 43.1 MGy. In both (b) and (c) the regions with lighter color represent cumulative doses where little to no change in the irradiated area was observed by FM. The x-axis is not to scale.

An overall picture of the dominant radical reactions as a function of cumulative dose for nanoparticles in DI water, soluble BPEI in DI water, and nanoparticles with radical scavenger is illustrated in **Figure 3.7**. The colors in each horizontal bar denote the approximate range of cumulative doses where each radical reaction dominated for each type of sample, as observed by FM, with white corresponding to no perceivable change to the sample. As metallic nanoparticles enhance electron beam damage to ligands near the

surface, removing much of the excess ligand prior to experiments can prevent the initial crosslinking reactions. Our experiments demonstrated that electron beam alterations to surface capping ligands could be delayed to some extent by including a radical scavenger.

The time dependent ligand surface coverage on nanoparticles and the silicon nitride membrane during LPTEM experiments has several implications for the colloidal and interfacial properties of LPTEM nanoparticle samples. First, removal or addition of ligands by radical reactions modifies the surface charge on the nanoparticles and silicon nitride membranes. While fluorescence intensity changes do not directly correspond to changes in surface charge, there is clearly a significant change in ligand surface coverage on nanoparticles after electron beam irradiation, especially at short times in the absence of radical scavengers. The radiation induced reactions can have significant effects on the surface charge of nanoparticles and thus on their electrostatic and steric colloidal interactions and overall colloidal stability. Changes in surface charge and ligand coating thickness will impact nanoparticle-nanoparticle and nanoparticle-membrane interactions during self-assembly. Perhaps the most interesting observation is that the most significant changes in surface concentration of ligands occurred at *short times and for low cumulative doses*, indicating low dose imaging alone may not be effective at preventing significant electron beam modifications to polymer capping ligands and that radical scavengers must be used in concert with low dose imaging.

Several prior works by our group and others have demonstrated irreversible electron beam induced aggregation of polymer ligand capped nanoparticles during LP-TEM.[135,136,167] It is plausible that electron beam induced intermolecular crosslinking and chain scission of polymer ligands will contribute to nanoparticle aggregation by reducing

nanoparticle colloidal stability or covalently linking nanoparticles together. An important implication of this process is that irreversible electron beam induced aggregation of nanoparticles is a kinetically controlled process driven by radical reactions, making it distinct from self-assembly, which is a reversible process driven by interparticle interactions. Even though radiation induced crosslinking can explain some nanoparticle systems with high molecular weight polymeric ligands, it appears that nanoparticles capped with small molecules do not display irreversible nanoparticle aggregation. For an example, recent LPTEM self-assembly studies of nanoparticles capped with small molecules (*e.g.*, carboxylic acids, cationic surfactants) showed reversible assembly under electron beam irradiation, implying that electron beam damage to the surface ligand coating did not result in irreversible aggregation.[219,220] Prior LPTEM experiments have shown that BPEI functionalized nanoparticles attached to the silicon nitride membrane began to diffuse under electron irradiation after an initial lag time.[162] Prior studies have posited this was due to radiation induced changes in pH[161] or electron beam charging of the silicon nitride membranes,[162] but pH changes and charging occur on short time scales (milliseconds) compared to the lag time for particle motion to begin (tens of seconds).[165] Our results show that ligand surface concentrations can increase on the nanoparticles and silicon nitride membranes over tens of seconds, which could increase repulsive steric and electrostatic forces.

The specific functional groups present on a polymer ligand will mediate the type of radiation reactions it undergoes upon electron beam irradiation. Aqueous PEI solutions degrade upon electron irradiation by chain scission reactions at secondary amine sites and carbon-carbon bonds in the main polymer chain.[223] At neutral pH values, primary amine

groups on PEI are mostly protonated and repulsive electrostatic forces between positively charged polymer molecules may prevent crosslinking. Similar effects are observed for polyacrylic acids where negatively charged carboxyl groups suppress crosslinking reactions; crosslinking was only observed at acidic pH values (~2) where most carboxylic acids were uncharged.[231] Similarly, polymethacrylic acids prefer chain scission over crosslinking and degrade by β-fragmentation of alkyl radicals formed during radiolysis.[253] Chitosan, a polymer molecule containing amine and hydroxyl functional groups predominantly undergoes chain scission through peroxyl radicals formed in the presence of oxygen or through scission of glycosidic bonds in deoxygenated solutions.[254] A recent study by our group showed that PEG – SH ligands act as radical scavengers for hydroxyl radicals by hydrogen abstraction from the thiol groups and PEG chain.[167] In aqueous solutions of PEG or polyacrylamide, intermolecular and intramolecular crosslinking prevails over degradation in deoxygenated solutions while main chain scission dominates with oxygen present.[232,255,256] Therefore, the molecular structure of the ligands are important in determining the successive radiation driven reactions of polymeric capping ligands during LPTEM experiments.

3.5 Conclusions

We utilized correlative LP-TEM and FM to investigate electron beam modification of BPEI capping ligands for controlled nanoparticle imaging with LP-TEM. BPEI coated silver nanoparticles irradiated in LP-TEM for different times and cumulative doses were labeled with fluorescent molecules after imaging, which enabled directly visualizing the outcome of electron beam driven reactions with capping ligands. Two competing electron beam induced reactions, intermolecular crosslinking and chain scission, determined the

fluorescence intensity of the nanoparticles and silicon nitride membrane with irradiation time. Crosslinking reactions dominated at short irradiation times due to high concentrations of free BPEI ligand in solution and high crosslinking reaction rate constant, while chain scission reactions dominated for irradiation times of > 5 minutes due to increased concentration of crosslinked polymers and decreased soluble polymer concentration. Crosslinking dominated for all cumulative doses tested in the absence of nanoparticles and for nanoparticles in the presence of tert-butanol as a radical scavenger. The observations are explained in terms of kinetic competition between crosslinking and chain scission reactions and the relative amounts of oxidizing hydroxyl radicals created. Competing electron beam reactions are expected to modify the surface properties and colloidal interactions of the nanoparticles and silicon nitride membranes by modifying electrostatic and steric interparticle interactions. This method can be extended to probe other capping ligand chemistries, such as carboxylic acid or thiol moieties, by utilizing commercially available fluorophore conjugation chemistries developed for biomolecules. We expect the specific response of a capping ligand to the electron beam will be chemistry and solvent specific. The example of BPEI ligand reactions serves as an initial demonstration of how correlative FM and LP-TEM can be used to track electron beam-ligand reactions and demonstrates the potentially complex and time dependent modifications the electron beam can induce in the surface ligand chemistry and concentration, even for low dose imaging conditions.

Chapter 4. Polymer reaction driven assembly of gold nanoparticles into Turing patterns.

4.1 Introduction

Unique chemical, photonic, magnetic, and catalytic properties emerge in ordered ensembles and patterns of nanoparticles on solid substrates. These emergent properties are controlled by both the nanoparticle composition and their spatial arrangement. Nanoparticle patterns have been incorporated for diverse applications such as in electronics for nano – transistors,[257] logic circuits,[258] stretchable wireless electronics,[259] foldable batteries,[260] nanophotonic modulators,[261] photodetectors and electroluminescent diodes,[262] biosensors,[9,263] pressure sensors,[264] and vapor sensors,[265] and supercapacitors.[266] Nanoparticle patterns are also utilized in catalytic platforms to enhance catalytic activity,[267,268] as stamps / templates in synthesis of microporous thin films,[269] to increase solute selectivity in microchip capillary electrophoresis[270] and to synthesize superhydrophobic surfaces.[271] Both top – down and bottom – up approaches have been used to make nanoparticles patterns on different substrates. Lithographic techniques such as direct electron beam writing, focused ion beam (FIB) milling and dip – pen lithography are used to generate nanoparticle arrays with nanometers scale control over pattern geometry.[272–278] These lithographic techniques are a popular choice due to the ability to fabricated precise intricate patterns with high reproducibility and resolution.[279] However, the serial nature of top-down pattern formation requires long fabrication times and there are limitations in material choice that can be deposited by lithographic techniques. Parallel methods, such as spin coating, dip coating, drying/dewetting, flow coating, organic

molecule based templating (e.g. Micelles, DNA origami) and interfacial deposition have been developed to obtain 2D nanoparticle arrangements covering large areas with reduced fabrication times.[280–284] Surface template directed assembly of nanoparticles employ lithographically patterned solid surfaces that can capture nanoparticles deposited via parallel methods to assemble particles on the templated pattern.[279]

The above techniques for forming nanoparticles patterns all require either soft or hard templates or nanoparticle surface ligands with specific interactions (*e.g.*, DNA, peptides). Significant effort has been given to adapt functions and processes in biological systems, such as self – assembly and biomolecular interactions, to arrange nanoparticles into spatial patterns that exhibit emergent functional properties. Despite the huge effort deposed on developing this diverse pool of techniques for preparing nanoparticle patterns on substrates, a common mechanism by which patterns emerges in nature, reaction-diffusion instability (RDI), has been underutilized by the material science community. There is increasing evidence that RDI is responsible for formation of coloration patterns on the skin of mammals and fish,[76,77] digitation during embryo morphogenesis,[85] and cellular patterns in tissues, such as spatial patterns of hair follicles.[86] During RDI induced pattern formation, an initially randomly distributed system of molecules undergo activation and inhibition reactions that couple with dissimilar diffusion coefficients, which together leads to a mathematical instability that results in stable spatial patterns of the molecules or cells, known as Turing patterns.[74] In a simple two species RDI system, an activator species catalyzes the production of itself while diffusing slowly. An inhibitor species diffuses faster while suppressing the production of the activator, leading to local accumulation of activator and accumulation of inhibitor in the periphery creating a periodic pattern in space.[75] The

RDI framework was applied for multiple synthetic chemical systems, where it is shown to form two dimensional (2D) or three dimensional (3D) stable patterns at the micron to macroscopic scales.[97,103,285,286] Only a very few synthetic systems have been discovered to this date that produce stable patterns at the nanometer scale resembling Turing patterns, which makes it difficult to come up with design rules to discover new nanoscale reaction – diffusion systems manifesting spatial patterns.[104,106–108] Difficulty in creating dissimilarity in diffusion coefficients between chemical species that is favorable for pattern formation, which are usually in the same order of magnitude, and difficulty in instigating an instability in an otherwise homogenous stable system could be a few reasons behind lack of application of RDI for nanopatterning.

In this study we show that nanopatterns akin to Turing patterns emerge in a nanoparticle – polymer system at a solid-liquid interface. The nanoparticle – polymer system is exposed to chemical radicals generated by irradiating the solvent with a high energy electron beam, which also enables high spatial resolution dynamic imaging using liquid phase transmission electron microscopy (LPTEM). Here we manipulate the electron beam – sample interactions to create an RDI in the nanoparticles – polymer system and use the interactions of nanoparticles and polymer molecules with the solid substrate to restrain their motion and create diverge diffusion coefficients, leading to formation of diverse types of nanoscale spatial patterns of nanoparticles.

4.2 Materials and Methods

4.2.1. APTES treatment of silicon chips

Silicon chips used for LPTEM were first cleaned with acetone to remove the photo – resistant layer and then cleaned with methanol to remove any organic impurities on the chips followed by drying with compressed air. The chips were plasma cleaned (Harris plasma cleaner) for 2.5 minutes. The small silicon chips were used as prepared and top silicon chips were submerged in a solution of 3% w/w (3-Aminopropyl)triethoxysilane (APTES, Sigma) at 75^0C and kept for 1 hour. Afterwards the chips were cleaned with DI water and air dried.

4.2.2. Preparation and deposition of nanoparticles

Ligand exchange was used to prepare 5 nm gold nanoparticle coated in self-assembled monolayers of carboxylic acid terminated organic ligands. 100 µl of aqueous 80 mM thiol - PEG_4 - carboxylic acid (PEG works) solution and 100 µL of aqueous 80 mM thiol - PEG_8 - carboxylic acid (PEG works) solution was added to 10 mL of as received citrate capped 5 nm gold nanoparticles (nanoComposix). The nanoparticle - ligand solution was stirred for 72 hours to facilitate exchange of the thiol ligands for the citrate ligands on the nanoparticle surfaces. The excess free ligands in the solution were removed by repeated centrifugal filtration through a 10 kDa cellulose acetate filter (10k, Thermoscientific). The concentrated nanoparticle retentate solution was dispersed in DI water. This cleaning procedure was repeated 2 more times and the resulting concentrated gold nanoparticle solution was dispersed in a buffer of 5 mM 2–(N–morpholino)ethanesulfonic acid (MES, Thermoscientific) and 5 mM N–Hydroxysuccinimide (NHS, Thermoscientific) at a pH of

6.75. Freshly prepared 1-Ethyl-3-(3-dimethylaminopropyl)carbodiimide (EDC, Thermofisher) aqueous solution was added to nanoparticle solution such that the final EDC concentration was 5 mM. After 10 minutes, a drop of nanoparticle solution was deposited on the silicon nitride window of the top chips to facilitate conjugation of particles to the amine coated silicon nitride. Afterwards the chip was rinsed with DI water to remove unbound nanoparticles and then dried with air. These chips were used for all experiments except for the experiment without nanoparticles where the top chip was directly used after APTES treatment.

4.2.3. LPTEM experiments

An aqueous solution of MES, NHS and EDC was prepared by mixing a freshly prepared EDC solution with the buffer (MES 5 mM, NHS 5 mM, pH 6.75) where the final EDC concentration was 1 – 5 mM. The liquid cell was assembled with a drop of the aqueous solution of buffer and EDC confined between the silicon chips in the sample holder. The aqueous solution was flowed into the liquid cell at a flow rate of 300 µL/h throughout the experiments using a syringe pump (Harvard Apparatus). For the experiment without EDC, only buffer was used in the liquid cell. For the experiment with radical scavenger, EDC and Tert – butanol was mixed with the buffer at final concentrations of 5 mM and 10 M respectively. The imaging was performed using a JEOL JEM-2100F field emission transmission electron microscope (TEM) operating at 200 kV. The nanoparticles were imaged in scanning TEM (STEM) mode at electron dose rates of MGy/s by varying the spot size of the electron beam and magnification.

4.3 Results

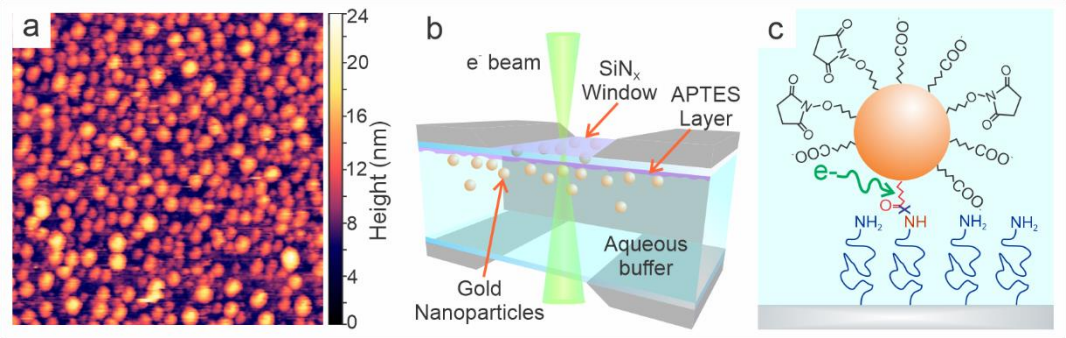

Figure 4.1. (a) AFM image of thickness variation of APTES on SiN_X membrane (b) liquid cell setup during LPTEM experiments (c) Gold nanoparticles immobilized on APTES treated SiN_X membrane by EDC – NHS chemistry.

AFM images of the silanized SiN_x surface showed an APTES layer that was rough, consisting of mounds of polymer with maximum thicknesses of ~20 nm (**Figure 4.1a**). This is consistent with literature observations that dissolving APTES in water causes polymerization of the monomers to form oligomers, which deposit on the surface as a thick, non-uniform coating layer.[287,288] The carboxyl groups on nanoparticles were conjugated to amine groups on SiN_X membrane through amide coupling chemistry, where carboxyl groups react with linker molecule EDC and NHS to make a metastable intermediate which is reactive with amine groups. The gold nanoparticles were imaged in a liquid cell containing an aqueous buffer with a liquid layer thickness of about 500 nm (**Figure 4.1b**). Upon initial irradiation by electron beam during imaging, nanoparticles become mobile in the solvent, indicating that the covalent amide bond between the nanoparticles and the SiN_X membrane is cleaved and NPs gain freedom to move and interact with other nanoparticles and surface siloxane (**Figure 4.1c**). Previously it has been demonstrated that amide bonds are preferentially cleaved during radiolysis.[289] In addition to varying the solution

chemistry, we varied the intensity of the electron beam to investigate the impact on the nanoparticle assembly. The electron beam intensity is reported in units of Grays, which is the SI unit for absorption of ionizing radiation and has units of energy absorbed per mass absorbing medium (1 Gy = 1 J/kg).

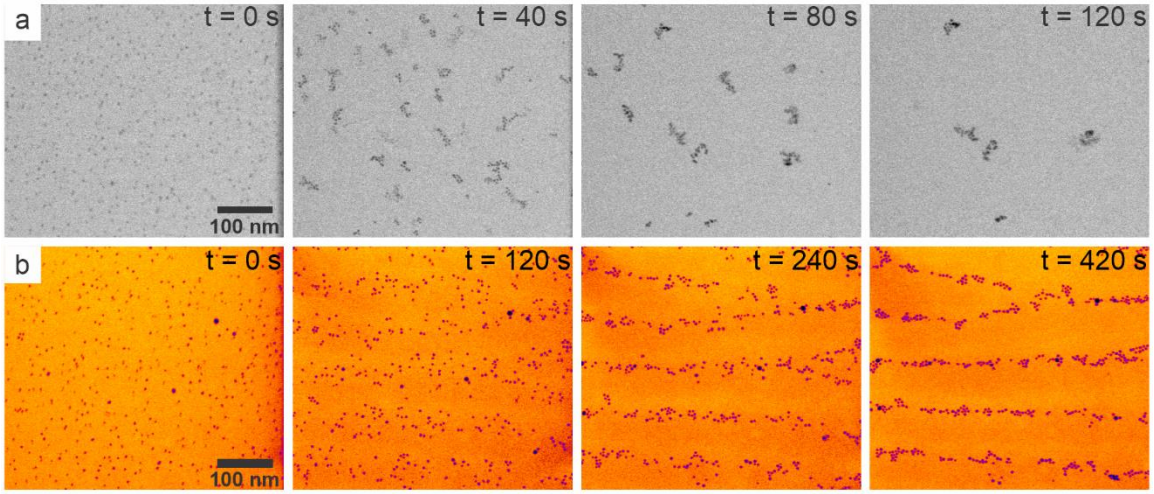

Figure 4.2. (a) Time lapsed images of gold nanoparticles imaged at a dose rate of 79.5 MGy/s s (electron beam current of 74 pA and a magnification of ×500k) without EDC in solution. (b) Time lapsed images of gold nanoparticles imaged at a dose rate of 79.5 MGy/s (electron beam current of 74 pA and a magnification of ×500k) with EDC at an initial concentration of 5 mM in solution. The images are false colored to show the polymer striped in the background. Nanoparticles appear purple and siloxane polymer dark orange and brown.

When gold nanoparticles anchored to top chip were imaged in an aqueous buffer only containing MES and NHS, nanoparticles detached from the surface as soon as irradiated and rapidly aggregated into small, disordered aggregates containing tens of nanoparticles (**Figure 4.2a**). Nanoparticles moved rapidly during imaging, and the slow frame rate of imaging was not sufficient to capture particle movement clearly in the first

10 s. By 15 seconds small aggregates, mostly dimers or trimers could be seen and by 25 seconds the nanoparticles assembled into disordered aggregates. The aggregates moved out of the imaging area upon continuous imaging and two minutes after the start of imaging most of the nanoparticles and aggregates were gone from the imaging area (**Figure 4.2a**). Nanoparticles were imaged with EDC included in the buffer medium. As the electron beam cleaves amide bonds, EDC continuously reforms the bonds, confining the nanoparticles to the surface during LPTEM imaging (**Figure 4.1c**). Upon the first few seconds of imaging with EDC at a concentration of 5 mM at an electron beam current of 74 pA and a magnification of ×500k (electron dose rate of 79.5 MGy/s), nanoparticles moved significantly more slowly than when EDC was not included. Further imaging revealed that NPs moved slowly along the membrane surface and after 1.5 minutes there were visible signs of the initially homogenous nanoparticles distribution segregating into horizontal zones. By 3 minutes slow movement nanoparticles created narrow horizontal bands dense with nanoparticles (**Figure 4.2b**). After five minutes of imaging the horizontal stripes densified into strings of nanoparticles, where nanoparticles aggregated together and could be seen forming Y – junctions in the next 2 minutes. Concurrent with nanoparticle movement, we observed formation of diffuse horizontal stripes of lower image intensity surrounding the nanoparticle strings. This contrast indicated that these regions had a higher average mass-density compared to the solvent and were attributed to formation of polymerized APTES layers. Nanoparticles congregated on the low image contrast bands and were mostly absent in between the bands. The nanoparticles strings were evenly spaced, separated by about 100 nm.

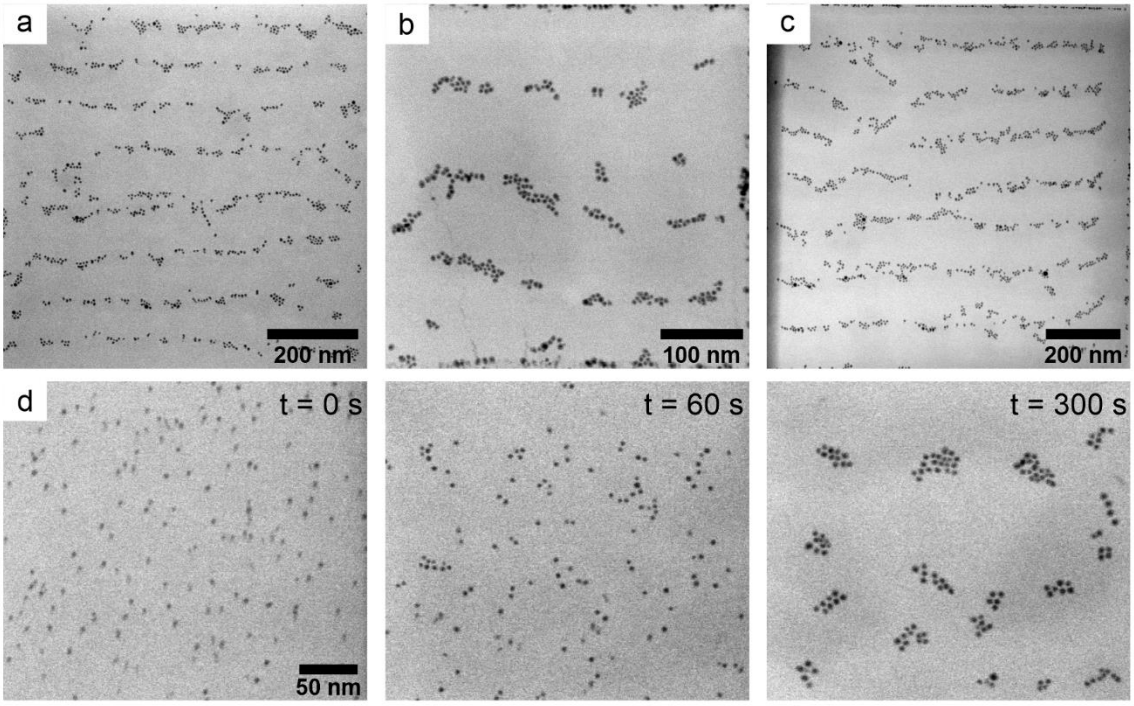

Figure 4.3. String patterns of gold nanoparticles imaged at dose rates of (a) 35.0 MGy/s s (electron beam current of 74 pA and a magnification of ×400k), (b) 106.5 MGy/s s (electron beam current of 74 pA and a magnification of ×600k) and (c) 44.6 MGy/s s (electron beam current of 141 pA and a magnification of ×500k) with EDC at an initial concentration of 5 mM in solution. (d) Time lapsed images of gold nanoparticles imaged at a dose rate of 203.4 MGy/s s (electron beam current of 74 pA and a magnification of ×800k) with EDC at an initial concentration of 5 mM in solution.

The formation of horizontal nanoparticle strings only occurred over a small range of electron dose rates (**Figure 4.3a-c**). The average spacing between two adjacent strings was 100 nm, 120 nm, 80 nm and 110 nm for dose rates of 35.0 MGy/s, 44. 6 MGy/s, 79.5 MGy/s and 106.5 MGy/s, indicating there was no trend between nanoparticle string spacing and dose rate. Increasing the dose rate beyond 203.4 MGy/s resulted in aggregation of nanoparticles into small random shaped aggregates with nanoparticles organized into a

hexagonal closed pack arrangement (**Figure 4.3d**). We observed formation of higher mass-density regions on the substrate, likely regions of higher APTES concentration. With increasing magnification and electron dose rate, the assembly rate increased and the nanoparticles moved more quickly from the imaging area. This assembly behavior contrasts the case without EDC present (**Figure 2a**), which might be due to additional hydrophobic forces with EDC as described in chapter 2 and interactions with the substrate.

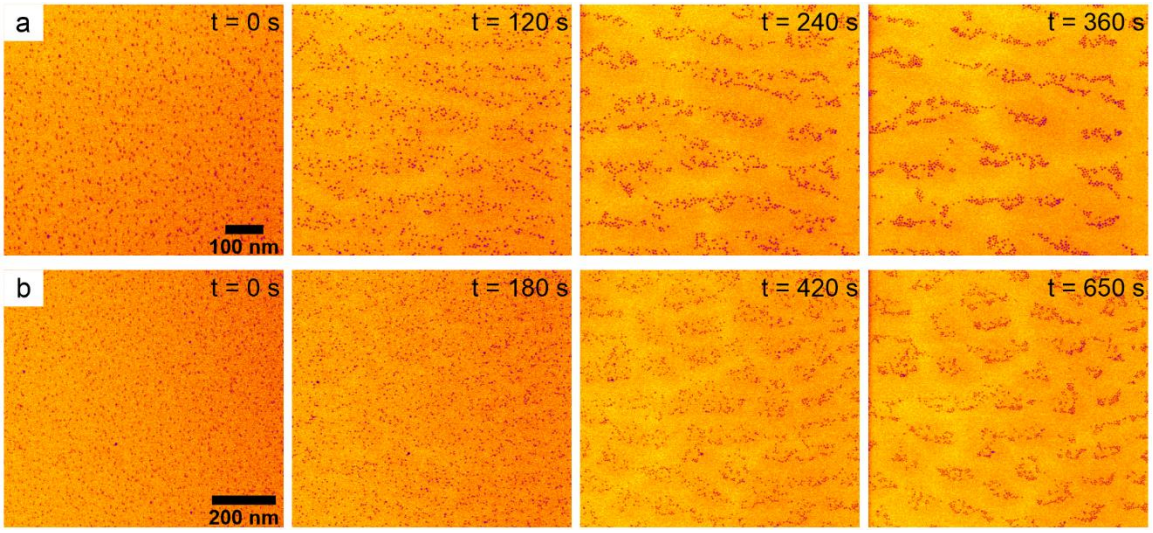

Figure 4.4. (a) Time lapsed images of labyrinth pattern formation in gold nanoparticles imaged at a dose rate of 79.5 MGy/s (electron beam current of 74 pA and a magnification of ×500k) with EDC at an initial concentration of 2.5 mM in solution. (b) Time lapsed images of spot pattern formation in gold nanoparticles imaged at a dose rate of 23.4 MGy/s s (electron beam current of 74 pA and a magnification of ×300k) with EDC at an initial concentration of 2.5 mM in solution.

Experiments varying the EDC concentration demonstrated that this parameter impacted the type of pattern formed. At an EDC concentration of 2.5 mM and the same imaging conditions as in **Figure 4.2b**, nanoparticles separated into elongated patches as

opposed to continuous horizontal bands across the imaging area (**Figure 4.4a**). With continuous imaging particles condensed into discontinuous linear nanoparticle structures oriented in different directions. This random arrangement of nanoparticle – dense strips is referred to as a labyrinth pattern. At a decreased electron dose rate of 23.4 MGy/s, the nanoparticle movement was very slow compared to previous experiments and no changes in the nanoparticle distribution were observed after ~3 minutes (**Figure 4.4b**). This time nanoparticles distribution as well as background intensity ruptured into small patches and nanoparticles contracted to form spot like pattern seen on leopards. At some places these spots showed almost hexagonal close packed arrangement.

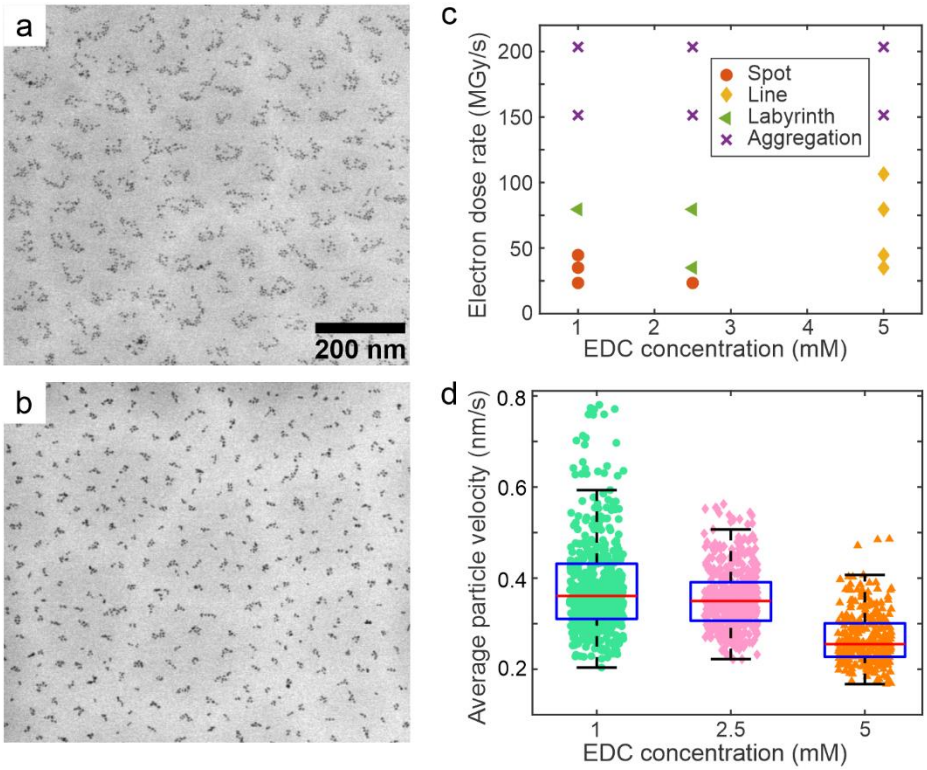

Figure 4.5. Spot patterns of gold nanoparticles in the sample of 1 mM EDC imaged at dose rates of (a) 23.4 MGy/s s (electron beam current of 74 pA and a magnification of ×300k) and (b) 79.5 MGy/s s (electron beam current of 74 pA and a magnification of ×500k). (c)

Phase diagram of different nanopatterns against EDC concentration and electron dose rate (d) Average velocity of nanoparticles at a dose rate of 79.5 MGy/s vs. EDC concentration.

Reducing the EDC concentration further to 1 mM also resulted in spot like nanoparticle pattern instead of a string pattern for dose rates ranging from 23.4 to 76 MGy/s (**Figure 4.5a,b**). The phase diagram shows that spot patterns emerged at low EDC concentrations and low dose rates (**Figure 4.5c**). Going below this dose rate is not possible as lower magnification beyond this point is not sufficient to resolve the 5 nm gold nanoparticles. Spot patterns transitioned to labyrinth – like patterns in the mid dose rates while at high dose rates it was always aggregation. Nanoparticle string patterns were only observable at a higher EDC concentration of 5 mM in the mid – range of dose rates. The motion of nanoparticles is controlled by EDC as increasing EDC concentration is expected to enhance the amide coupling reaction rate, which will anchor the nanoparticles to the surface more strongly. To test whether the mobility of nanoparticles changes with EDC concentration, the average velocity of each particle over 300 s was measured as a function of EDC concentration while holding electron dose rate constant at 79.5 MGy/s (**Figure 4.5d**). The mean velocities of nanoparticles decreased with increasing EDC concentration, supporting the proposed mechanism. At low EDC concentrations, nanoparticles assembled into smaller sized, less ordered spots due to higher nanoparticle mobility. At higher EDC concentrations nanoparticles formed string patterns due to low mobility of nanoparticles that facilitated controlled, slow motion across longer distances.

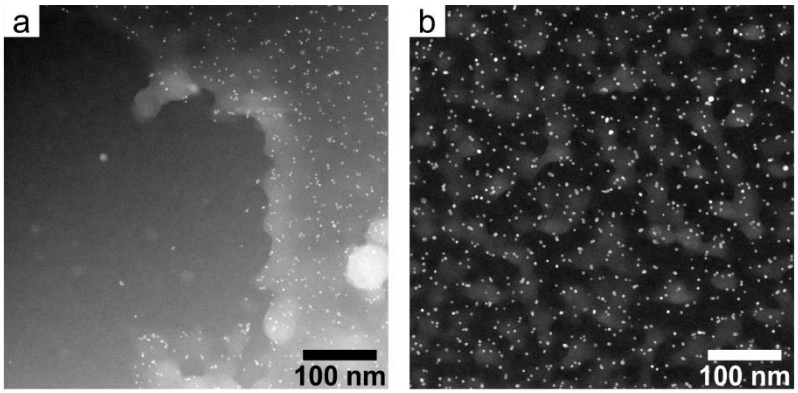

Figure 4.6. Electron beam modification of the APTES layer on SiN_X membrane as seen after LPTEM experiments. (a) a region where underlying polysiloxane layer was damaged by radiolysis (b) segregated polysiloxane patches in an imaged region of spot pattern.

Darkfield TEM imaging of the dried SiN_x chips after LPTEM experiments revealed regions where electron beam irradiation modified the APTES layer on the SiN_X membrane (**Figure 4.6**). An area of the SiN_X membrane where the APTES layer was nearly completely removed by electron beam induced reactions is illustrated in **Figure 4.6a** and regions where the siloxane polymer piled up could be clearly seen. An area where dose rate-controlled imaging was conducted showed patches with higher mass-thickness contrast, similar to spot patterns seen during liquid phase experiments (**Figure 4.6b**). To confirm these findings that radiolysis of the siloxane polymer drives the pattern formation, a hydroxyl radical scavenger, tert – butanol was included in the system as in chapter 3 (**Figure 4.7a**). We expect that the radical scavengers will eliminate hydroxyl radicals and will minimize the electron beam induced modification of the APTES, preventing formation of nanoparticle patterns. With 10 M tert-butanol present, we did not observe aggregation or patterning of nanoparticles under the same experimental conditions that the string patterns emerged. Some minor nanoparticle motion was observed over several minutes. At

longer irradiation times of 580 s we observed some damage of the APTES, perhaps due to depletion of the tert – butanol radical scavenger. To establish whether nanoparticles were required to form polymer and nanoparticle patterns we performed experiments under the same imaging conditions with only APTES present on the SiN_x surface. Here, fluctuations of background intensity indicated some damage to the APTES layer with increasing imaging time, but no discernible pattern emerged (**Figure 4.7b**). This finding demonstrated that presence of nanoparticles is imperative for pattern emergence, which might be due to local dose enhancement by gold nanoparticles.[242,290]

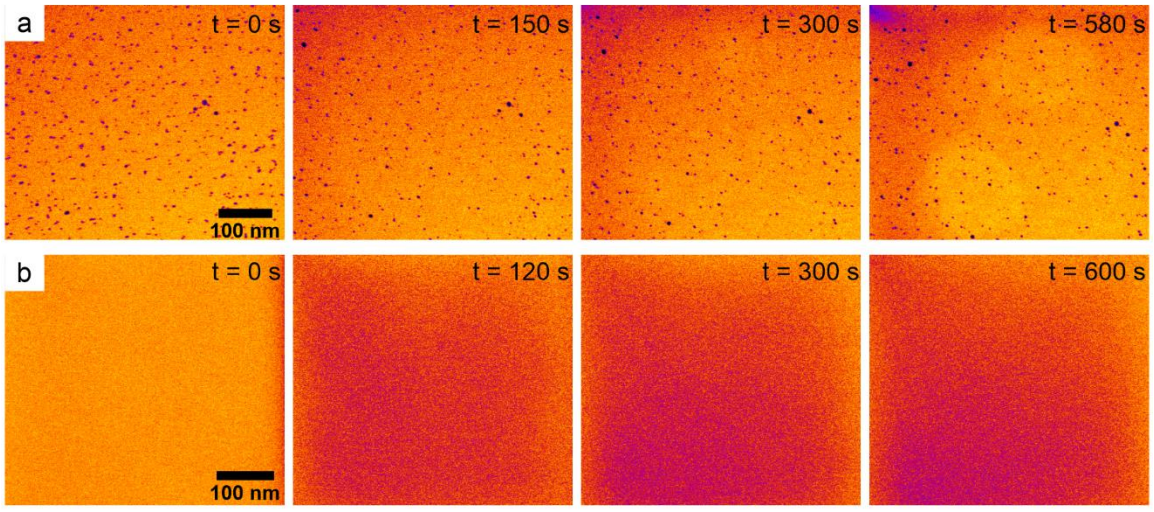

Figure 4.7. Time lapsed images of SiN_X membrane at a dose rate of 79.5 MGy/s (electron beam current of 74 pA and a magnification of ×500k) and EDC at an initial concentration of 5 mM in solution (a) with 20% w/w tert – butanol and (b) without gold nanoparticles.

4.4. Discussion

Previous studies on nanoparticle assembly with LPTEM have utilized physisorption of nanoparticles on the SiN_X membrane by drying a drop of nanoparticles on the top chip of the liquid cell to obtain a high surface coverage of nanoparticles near the membrane to observe nanoparticles dynamics.[135] Here, particles were mobilized immediately after beam irradiation and underwent assembly in the next few minutes. Silanization of SiN_X membrane by APTES was used to eliminate unwanted motion of nanoparticles by covalently attaching gold nanoparticles to the APTES layer via amide coupling.[291] Our AFM results showing a rough APTES layer with variable thickness between a few nanometers and ~20 nanometers indicates that APTES undergoes oligomerization, which is consistent with previous studies of APTES surface treatments in aqueous media.[287] The APTES molecule consists of 3 ethoxy groups branching out from the Si atom and one propane chain terminated by an amine group. The ethoxy groups are rapidly hydrolyzed to silanol groups in water, which can then form silicon oxygen (Si - O – Si) bonds with surface silanol groups (Si-OH) and silanol groups on neighboring hydrolyzed APTES molecules. During aqueous phase silanization, there are several ways in which APTES can form a siloxane layer on the surface, including single APTES molecules bonding with the surface through one to three silanol groups, formation of lateral structures of APTES by bonding with both surface and adjacent APTES, formation of ladder like vertical structures by stacking of APTES thought Si – O – Si bonds, and attachment of silane oligomers formed in the solution to the surface.[287,288,292] Hydrogen bonding of amine groups and silanol groups can also contribute to multilayering.[288,292,293] This multilayered APTES structure provides abundant siloxane polymer for radiolysis

induced polymer radical reactions inside the liquid cell in comparison to a monolayer, which could significantly alter the chemical processes and nanoparticles behavior near the membrane.

As discussed in chapter 3, radiolysis of water produces a myriad of radicals including oxidating hydroxyl radicals that have the most significant effect on organic materials. Hydroxyl radicals attack organic molecules by abstracting hydrogen atoms from carbon-hydrogen bonds, such as alkyl carbons, leaving an alkyl radical site.[168] Hydroxyl radicals can make weakly bound complexes with certain bonds in Si – O bonds, which leads to homolytic cleavage.[294] The resulting polymer radicals either participate in crosslinking or chain scission reactions or are neutralized by an electron. According to the chemical structure of APTES oligomers and multilayers, chain scission polymer radical reactions will propagate through the cleavage of Si – C, C – C, O – H, C – N and Si – O bonds in the polymer matrix and intermolecular crosslinking of fragmented polymer will occur through formation of Si – C, C – C, Si – O and Si – Si bonds.[289,294–297] Amide bonds are readily broken by radiolysis to make amine groups and carboxyl groups, which is likely the reaction leading to mobilization of covalently surface bound nanoparticles after exposure to the electron beam (**Figure 4.2a**).[289] Including EDC facilitates regeneration of the amide bond between surface amines and carboxylic acids on the nanoparticles. Here, nanoparticle motion is controlled by the interactions with the polymer coated SiN_x and follows the movement of underlying polymer in a smooth gliding motion across the surface unlike the hop and stick movement observed in previous studies of nanoparticles by LPTEM.[135,161,162] As nanoparticles approach within a few diameters of each other, interparticle interactions play an increasingly important role in the nanoparticle motion.

This observation implies that nanoparticles and siloxane polymer fragments initially move as a single entity across the surface, which might be due to polymerization with the membrane on the way. At high concentration of EDC, one nanoparticle might make several bonds with underlying siloxane polymer, both stationary polymer on the SiN_X membrane and free polymer fragments, limiting its mobility. However, lower concentration of EDC will produce fewer amide bonds and the mobility of the nanoparticles will be increased. Estimation of diffusion coefficients of nanoparticles during LPTEM assembly experiments revealed that they are 5 – 9 orders of magnitudes smaller than bulk diffusion coefficients. This discrepancy was attributed to physical phenomena which controls motion in addition to Brownian motion such as electrophoretic charging of membrane and nanoparticles and drag arising from interactions with membrane.[135,160] Overall, this shows that nanoparticles and bulky polymer complexes will experience slow diffusion coefficient relative to the large diffusion coefficients of hydroxyl radicals in the bulk liquid solution.

Previous LPTEM studies of nanoparticles physisorbed on the SiN_x surface saw nanoparticles only in the imaging area or in the peripheral of the imaging area were mobilized and assembled.[160] Similar behavior was observed here where patterns only emerged in the imaging area. The implication of this is that electron beam creates an instability in the initially homogenous system of randomly distributed nanoparticles bound to the siloxane polymer by means of radiolysis, similar to how a homogenous system is triggered to make Turing patterns by RDI. During imaging the local net electron dose near a nanoparticle will increase due to secondary electron emission which will locally accelerate radiolysis of water and increase production of hydroxyl radicals.[242,290] The rise

in hydroxyl radicals means a higher number of attacks on the siloxane polymer in the vicinity, thereby providing more radical sites for chain scission at the beginning. The nanoparticles increase the local concentration of both hydrogen radicals and polymer fragments around them, similar to a catalyst site leading to an irregular spatial distribution of chemical species. When nanoparticles are taken out of the system (**Figure 4.7**), the average dose received by the imaging area is decreased and the radical production hot spots are removed. The observation that the polymer layer sustained minor damage with no pattern formation indicated that nanoparticles are one of the essential components for pattern formation, consistent with the idea that nanoparticles act as hot spots for local radical generation. Removal of hydroxyl radicals by a radical scavenger further established that hydroxyl radicals are necessary for pattern emergence, consistent with the polymer radiolysis mechanisms discussed above.

So far, our experimental results have established that there are three major components in our RDI system, namely, slowly diffusing gold nanoparticles, rapidly diffusing hydroxyl radicals, and slowly diffusing siloxane polymer. There is a complex activation and inhibition interaction network among these three species. Therefore, this system could not be explained by a simple conventional two component RDI model where one component strictly assigned as the activator and the other component strictly assigned as the inhibitor. A recent work explored graph theoretical approach to multicomponent RDI, where components are assigned as nodes connected by feedback loops depending on their interactions. Positive feedback corresponds to activation and negative feedback corresponds to inhibition.[298] **Figure 4.8a** shows the proposed RDI mechanism controlling pattern formation in our system.

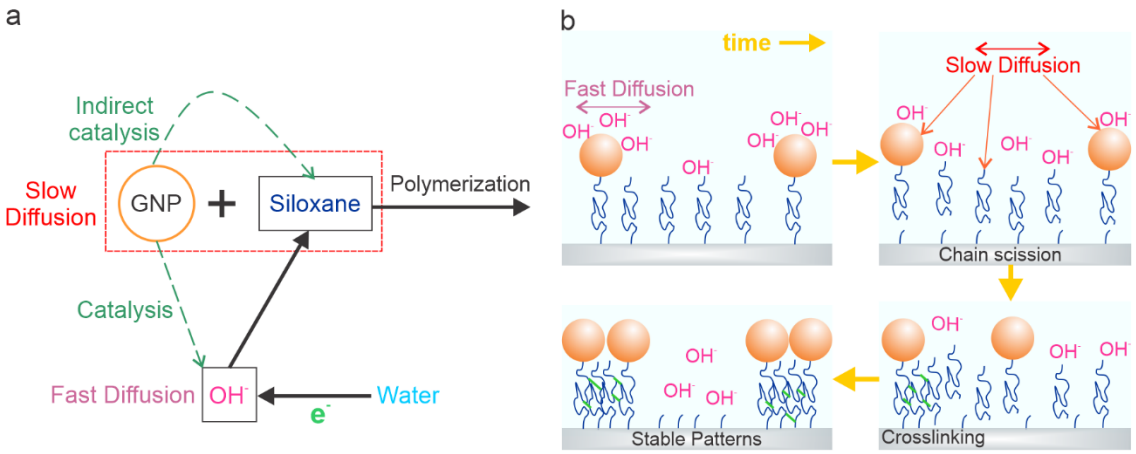

Figure 4.8. (a) Proposed reaction diffusion framework of the three – component system. (b) Time dependent changes in the system.

The chemical events occurring in the system are summarized as follows. Water reacts with high energy electrons from the TEM beam to produce hydroxyl radicals (OH) (**Figure 4.8a,b**). Next, hydroxyl radicals attack both amide links between the nanoparticles and polymer layer and produce radicals in the siloxane polymer layer. Nanoparticles take on the role of activator as they catalyze the production of hydroxyl radicals in the vicinity in a positive feedback loop; the more nanoparticles in a given area the more hydroxyl radicals are produced. Nanoparticles also indirectly catalyze the production of siloxane polymer radicals *via* hydroxyl radicals. These siloxane radicals participate in competing chain scission and polymer crosslinking reactions. When radical sites on the siloxane layer build up with continuous imaging (and continuous production of hydroxyl radical) chain scission propagates increasing the concentration of mobile siloxane fragments (low MW siloxane) and mobilized nanoparticles, which explains the lag time before nanoparticles starts to move. The production of siloxane fragments by hydroxyl radicals resembles an inhibition reaction, as hydroxyl radicals are consumed in this reaction. The depletion of

one component required for activation of a second component due to its rapid diffusion and production of the second component results in overall inhibition of the second component.[299] The mobilized nanoparticles and siloxane fragments slowly diffuse while intermittently polymerizing on the membrane which results in an overall slow diffusion. Simultaneously, hydroxyl radicals diffuse faster and build up in nanoparticle scarce regions, locally depolymerizing and depleting the polysiloxane. When the concentration of siloxane fragments becomes large in a particular area (siloxane is not continuously supplied to the system and the concentration would have an upper limit decided by the initial amount of siloxane on the surface), intermolecular crosslinking dominates and siloxane fragments are removed from the system by conversion to the polymerized siloxane (high MW siloxane) which condense on the SiN_X membrane, effectively reducing net concentration of siloxane fragments and resulting in stable patterns.

How an RDI system differentiates between different patterns depends on conditions such as rate constants, feed rates, initial spatial distribution of chemical species, diffusion coefficients, and the mechanism / reaction network. For an anisotropic patterns like nanoparticle strings to emerge from the initial homogeneous nanoparticle distribution, there should be some directional features arising in the system at the respective experimental conditions. Stripe patterns are found to be formed when there is either confinement by narrow geometry, a production gradient of chemical species across space, a spatial parameter gradient (e.g., interactions between species), or anisotropic diffusion coefficients.[300] In this system the only factor that contributes to anisotropy is the scanning electron beam, as we use isotropic nanoparticles and there is not gradient in polysiloxane concentration on the surface. The nanoparticle strings were always perpendicular to the

fast scanning direction of the electron beam (raster scanning direction of left to right and top row to bottom row). When the electron beam scanning direction was rotated by 90^0, the resulting nanoparticles strings remained perpendicular to the scanning direction. This observation confirmed that the directionality was introduced by the STEM beam and it might be due to either scanning beam induced production gradients of radicals or anisotropic diffusion coefficients arising from electric fields generated by the electron beam.

4.5 Conclusions

In this study we utilized LPTEM to investigate how Turing like patterns emerge in a nanoparticle – polymer system due to RDI. PEG – carboxyl coated gold nanoparticles arranged into diverse nanoscale patterns within minutes in the presence of a linker molecule, EDC, which facilitated covalent bonding between the nanoparticles and the underlying polymer layer. At high EDC concentrations and moderate electron dose rates nanoparticles formed string patterns, while labyrinth like patterns were observed at a low EDC concentration and moderate electron dose rates. Further reduction of electron dose rates at low EDC concentrations resulted in spot patterns. Inclusion of a hydroxyl radical scavenger halted formation of nanoparticle patterns and demonstrated that hydroxyl radicals were critical to pattern formation. Gold nanoparticles were also necessary for pattern formation, likely due to their ability to locally enhance radical production. A three – component reaction – diffusion mechanism, including hydroxyl radicals, gold nanoparticles and siloxane polymer, was proposed to explain the experimental observations. This system can be used as a model system to examine nanoscale Turing patterns in depth in the future.

Chapter 5. Conclusions and Future Directions

5.1 Conclusions

In this dissertation, we demonstrate two ways to produce colloidal assemblies under experimental conditions that are far from equilibrium. First, dissipative assembly was applied to a colloidal system to decipher the time dependent interparticle interactions during transient aggregation. Secondly, LPTEM was utilized to discover a system where nanoparticles could be assembled into 2D patterns with a reaction – diffusion mechanism.

- We successfully demonstrated that colloidal interparticle models developed for equilibrium assembly could be applied to dissipative assembly systems when the time taken for any significant changes in the system during dissipative assembly cycle is long compared to the diffusive time scale of the colloids. By developing a fluorescence spectroscopy method, we were able to quantify the time dependent hydrophobicity of particles during a dissipative assembly cycle. The interparticle interactions estimated using the time dependent zeta potential and hydrophobicity values qualitatively explained the fuel dependent assembly behavior of a dissipative colloidal assembly system.
- By using a correlative fluorescence microscopy and LPTEM method, we demonstrated that nanoparticle polymeric capping ligands undergo electron beam induced crosslinking and chain scission reactions. At small electron doses, crosslinking reactions dominated and increased the ligand coverage on nanoparticles and SiN_X membrane, while chain scission took over at high electron doses and decreased the ligand coverage. Without the presence of nanoparticles,

only crosslinking reactions were observed due to the diminished dose enhancement caused by metallic nanoparticles. Use of a radical scavenger could effectively slow down the crosslinking reactions and eliminate chain scission reactions.

- Based on the fact that electron beam induces major chemical changes to the sample in the imaging area during LPTEM, we used electron beam radiolysis of polysiloxanes to introduce an instability to an initially homogenous gold nanoparticles – polysiloxane film to produce Turing like patterns by a reaction – diffusion mechanism. The crosslinking and chain scission reactions of polysiloxane induced by electron beam, combined with different diffusion rates of radicals, nanoparticles, and polymers, produced spatial patterns of nanoparticles. Tuning electron dose rate and linker molecule concentration led to formation of spot, labyrinth, and stripe patterns.

5.2 Future Work

5.2.1 Expanding the experimental parameter space for nanoparticle pattern formation.

In chapter 4, we varied EDC concentration and electron dose rate to explore their impacts on the resulting nanoparticle assemblies. EDC controlled the nanoparticle mobility and electron dose rate determined whether nanoparticles formed surface patterns or underwent random aggregation. We observed string pattern formation only at an EDC concentration of 5 mM. Increasing the EDC concentration to 10 mM did not result in any Turing like patterns but instead nanoparticles assembled into hexagonal close pack arrangements. We did not observe any dependent of the separation between nanoparticle strings on electron dose rate at 5 mM EDC. Therefore, varying EDC concentration around

5 mM would be the next step. Also increasing the concentration of nanoparticles would increase the effective electron dose rate and accelerate the production rate of hydroxyl radicals which would change the dynamics in the system. This is quite similar to increasing electron dose rate by manipulating beam current and magnification, where we saw no pattern formation. But at the same time, small separation between nanoparticles at high concentrations would make the contribution from interparticle interactions to the nanopattern formation more pronounced, potentially changing the assembly dynamics and final pattern.

Here we use 5 nm gold nanoparticles, which due to their small size limits the range of dose rates that could be explored by preventing testing magnifications below ×300, 000 and low electron beam currents. Increasing nanoparticle size would enable exploring lower image magnifications and lower electron dose rates. Currently the patterns are confined into a small area defined by magnification. Testing low magnifications with large nanoparticles might make way for patterning a larger surface area. Using larger sized nanoparticles would also decrease the diffusion coefficient and increase the effective dose rate. Varying dwell time of the STEM beam also presents exciting prospects of expanding the parametric space as it defines the electron beam scanning rate. In a typical experiment we used a dwell time of 5 µs. Preliminary experiments at 2.5 mM EDC and reducing the dwell time to 2 µs (faster scanning rate) resulted in a labyrinth like pattern similar to the pattern in Figure 4. But when the dwell time was raised to 10 µs, nanoparticles formed random aggregates. The effect of electron beam scanning would be verified by conducting the experiments in the TEM mode. As directionality introduced by scanning is removed in TEM mode, at similar electron dose rate conditions the nanoparticles strings would not be

formed in TEM mode. The diffusivity of the nanoparticles and radical reaction rates could be manipulated by varying the temperature during LPTEM experiments. Temperature dependent change of spacing between nanoparticle strings or change of nanopattern from one type to another (e.g. string to spot) would yield valuable information in verification of reaction – diffusion model in future.

5.2.2 Investigating interparticle interactions during formation of nanoparticle surface patterns.

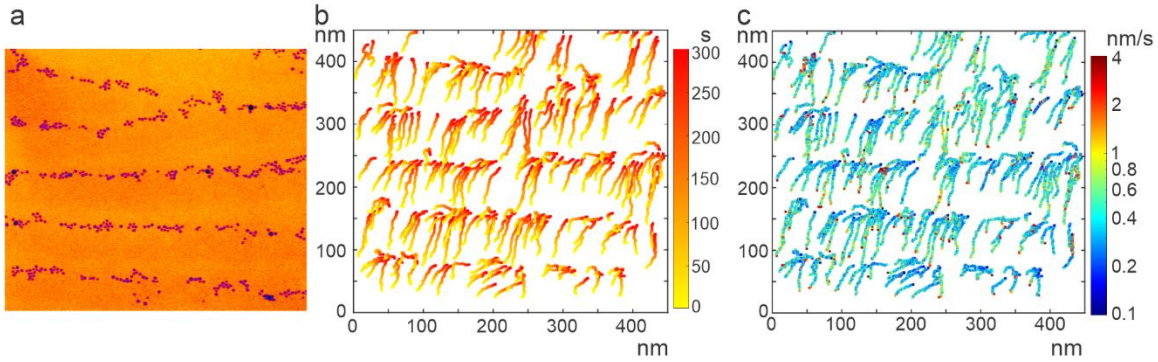

Figure 5.1. (a) Gold NP string pattern formed at a dose rate of 79.5 MGy/s (electron beam current of 74 pA cm-2 and a magnification of ×500k) with EDC at an initial concentration of 5 mM in solution. (b) The trajectories of the NPs across space. The color bar corresponds to the time during the assembly process. (c) Trajectories of the nanoparticles with the color representing instantaneous velocities of the NPs.

NPs are temporarily released from the polysiloxane film when a radical breaks the amide bond. During this time the particle will experience attractive/repulsive forces from surrounding NPs and the SiNx substrate due to various interparticle forces between them. The sum of pairwise forces between a particle and the neighboring particles will determine the instantaneous velocity of the particle while the amide bonds are broken. Therefore,

colloidal interparticle interactions should be considered when building an all-encompassing reaction – diffusion model. The preliminary particle tracking performed on the videos showed that particles moved in an upward direction compared to the downward direction of scanning electron beam (**Figure 5.1**). The velocity of particles was higher at the beginning of NP assembly and decreased as time went by when particles formed the string pattern. The real time forces acting between NPs could be estimated by modelling van der Waals attractive forces, electrostatic repulsive forces, steric repulsive and hydrophobic force with time from interaction potentials described in Chapter 1. The contribution to NP motion from interactions with underlying polymer layer could be introduced as a friction force opposing the motion of the particle. The direction of this force would be the direction of instantaneous velocity and could be quantified as the product of instantaneous velocity and a friction coefficient.

Jaewon et al. measured distance from one particle to all the other particles surrounding it and mapped it during nanoparticles aggregation in LPTEM (**Figure 5.2**).[122] One nanoparticle interacts with all the adjacent particles and forces experienced by the particle at an instance would depend on the distance to each particle. A net force can be calculated by summation of all the interaction forces with other particles and the direction of this force could be obtained as well. In their experiments the Brownian force acting upon the particles were considered and as the nanoparticles during pattern formation did not show any Brownian motion, it could be removed from our system. The hydrodynamic force accounts for the drag force experienced by a particle due to relative motion with another particle. This would be estimated by the product of relative velocity and hydrodynamic resistance function.[122] Mapping each type of force with time would reveal information on

contribution of interparticle interactions to nanoparticle pattern formation and which type of interaction dominated in each regime of nanopattern formation.

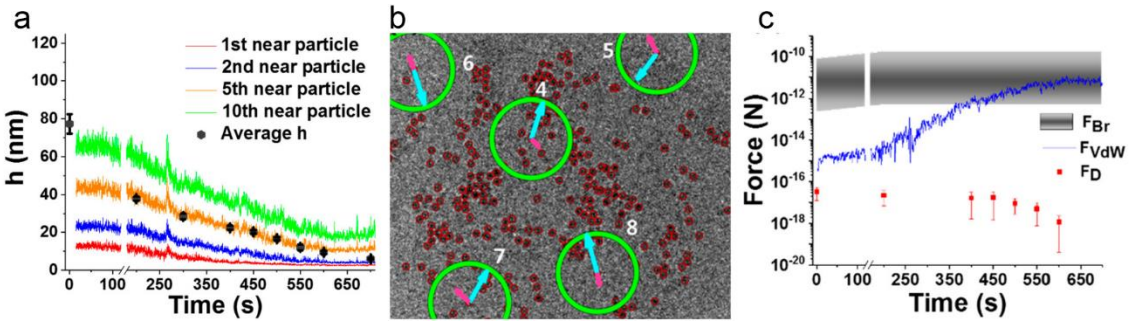

Figure 5.2. (a) Particle separation distance with time. (b) Different types of forces acting on particles at an instance in an LPTEM movie. The green circle represents the Brownian force (F_{Br}), the blue arrow represents the van der Waals force (F_{VdW}) and the pink arrow represents the hydrodynamic force (F_D). (c) Variation of theoretically calculated interparticle forces with time. Figures adapted with permission from reference.[122]

5.2.3 Determining reaction products of siloxane formed during LPTEM.

To establish a more accurate reaction – diffusion mechanism for the nanoparticle pattern formation in chapter 5, first we will need to identify the proposed electron beam induced polysiloxane chain scission and crosslinking reactions. This could be achieved by characterizing the structure and chemical composition of the film before and after irradiation by electron beam. The extent of polymerization and the type of bonds formed during radical-polymer reactions could be determined by attenuated total reflection Fourier transform infrared spectroscopy (ATR – FTIR), while the molecular weight of the resulting reaction products could be determined using matrix assisted desorption ionization time of flight mass spectrometry (MALDI – TOF). Korpanty et al. utilized mass spectroscopy to determine changes to polyethylene glycol (PEG) by electron irradiation during LPTEM by

spraying matrix molecules over the liquid cell chip followed by MALDI – TOF.[242] They were able to capture changes to the molecular weight distribution after irradiation (**Figure 5.2**) and when compared with the distribution without irradiation, the mass signal intensity was reduced and there were peaks at low mass intensities indicating chain scission of the PEG. Similarly, for polysiloxane, peaks at higher mass intensities would indicate crosslinking while peaks at lower mass compared to the original molecule would indicate chain scission.

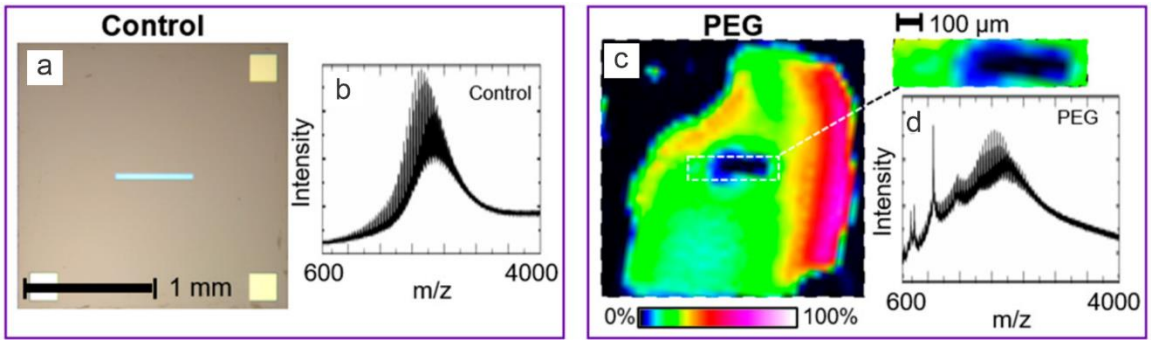

Figure 5.3. (a) Image of a liquid cell chip used for irradiation (b) mass spectra of a PEG coated chip before irradiation (c) MALDI-IMS color map of liquid cell chip after irradiation (d) mass spectra of the PEG coated chip after irradiation. Figure reproduced with permission from reference.[242]

The image area during nanoparticle pattern formation was a few hundred nanometers in size. The fluorescence microscopy data in chapter 4 showed that a low magnification (~ ×20,000) should be used during LPTEM imaging to match the resolution limit afforded by optical microscopy. Therefore, deciphering and utilization of FTIR microscopy or MALDI mapping on the exact regions irradiated at different dose rates would be difficult due to limited resolution, hence the sensitivity of the signal. However, an external electron source for irradiation of bulk samples under experimental conditions

similar to LPTEM could enable producing sufficient reaction products for analysis with MALDI-TOF and FTIR. The 3 MeV electron accelerator at the nuclear reactor facility at University of Maryland could be used to perform pulse radiolysis on samples and deliver electron doses comparable to doses delivered to irradiated regions during imaging with LPTEM. Here APTES treated silicon chips submerged in buffer could be irradiated at known electron doses.

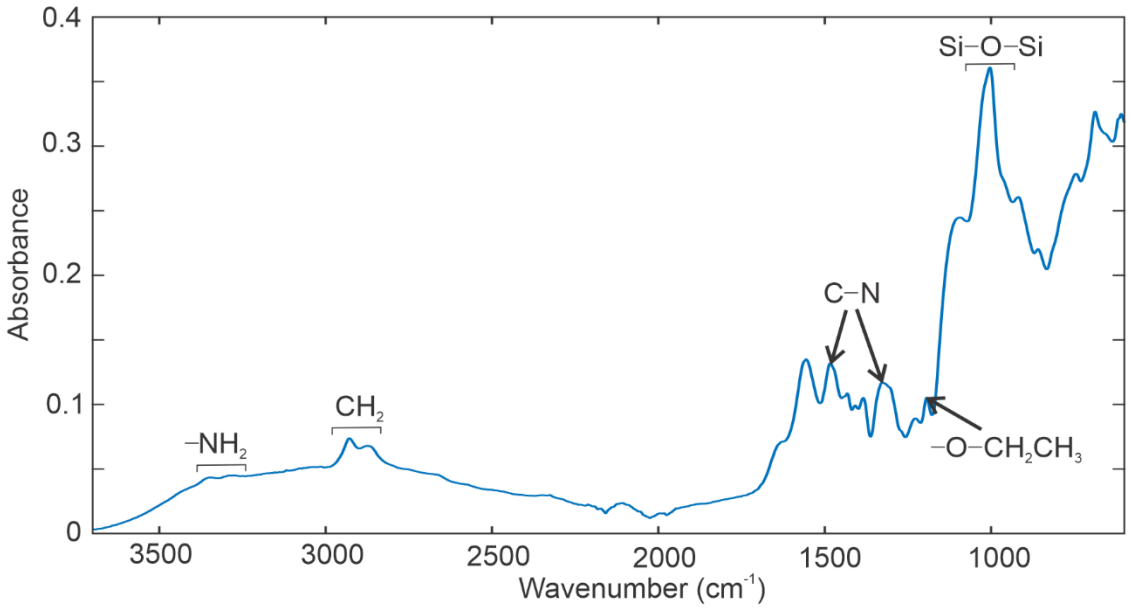

Figure 5.4. FTIR spectra of APTES layer on SiO_2 surface.

ATR – FTIR was widely used in previous studies to characterize siloxane thin polymer layers on substrates after APTES treatment.[301–303] Preliminary experiments of ATR – FTIR performed on APTES treated silicon surfaces using a diamond crystal resulted in a spectrum with characteristic peaks of several bonds in the polymer (**Figure 5.3**). The peak at ~1195 cm^{-1} corresponding to ethoxy groups implies that there are some residual ethoxy groups that were not hydrolyzed during APTES treatment to form Si – O bond.[302] These would later hydrolyze and supply a site for Si – O bond formation and crosslinking

during LPTEM experiments as well as supply ethylene groups in the vicinity for C – C or C – N bond formation. The intensity variation of bonds before and after irradiation would give an idea on which bonds were favored during polymer reactions. Whether the peaks corresponding to C – N bonds become more pronounced or not after irradiation would determine whether siloxane polymerization or chain scission occurred through C – N bond. Disappearance of peaks corresponding to alkyl groups would suggest that polymer radical reactions proceeded through radical sites produced on carbon atoms by hydrogen abstraction. Also in the experiments, we include MES buffer, NHS and EDC which are also organic molecules that could participate in radical reactions. We could factor in the contribution of these chemical species by irradiating a set of control samples submerged in only water, in an aqueous solution of MES and NHS, and finally to reproduce the LPTEM experiments conditions by submerging within an aqueous solution of MES and NHS with varying EDC concentration. Subsequently, we could do solid state NMR to find more accurate estimate of concentration of each type of bond, hence establishing the most probable polymer crosslinking or chain scission reaction pathways that we could use to refine the proposed reaction – diffusion model.

Appendices

A1. Estimating the Debye length using solution conductivity measurements

There were multiple types of ions present during dissipative assembly of the colloids, making determination of the ionic strength and Debye parameter challenging. Instead, we utilized experimental measurements of the solution conductivity before and after addition of EDC to obtain estimates for the ionic strength and Debye length. The conductivity of a dilute electrolyte solution can be determined by summing the limiting molar conductivities of the constituent ions multiplied by their relative concentrations[304]:

$$\sigma = \sum_i \Lambda_{m,i}^0 c_i. \tag{A1}$$

Here σ is the solution conductivity, $\Lambda_{m,i}^0$ is the limiting molar conductivity of a cation or anion, and c_i is the concentration of each ion. The limiting molar conductivity of an ion is determined from the diffusion coefficient,

$$\Lambda_{\mathrm{m,i}}^0 = \frac{z_i^2 F^2}{RT} D_i, \tag{A2}$$

where F is Faraday's constant and D_i is the diffusion coefficient of the ion i. The buffer solution contains sodium cations and 2-(N-morpholino)ethane sulfonate anions (MES). Sodium has a diffusion coefficient of $D_{Na^+} = 1.33 \times 10^{-9}\, m^2/s$ while the diffusion coefficient of the MES anion is $D_{MES} = 1.13 \times 10^{-9}\, m^2/s$.[305] For an ionic strength of $I = \frac{1}{2}\sum_i z_i^2 c_i$, the MES buffer solution prior to adding EDC has the following relation between solution conductivity and ionic strength,

$$I_{MES} = \frac{\sigma}{D_{Na^+} + D_{MES}} \frac{RT}{z^2 F^2}. \tag{A3}$$

The MES buffer solution had an initial solution conductivity of 1540 μS/cm, yielding an approximate ionic strength of 16.7 mM and a Debye length of $\kappa^{-1} \approx 2.4$ nm.

After addition of EDC the conductivity of the solution increased to 1843 μS/cm, 2294 μS/cm, and 2647 μS/cm for initial EDC concentrations of 5 mM, 10 mM, and 15 mM, respectively. EDC reacts to form 1-(3-dimethylamino)propyl-3-ethylurea (EDU), where both species are monovalent cations with unknown diffusion coefficients. The EDC and EDU cations are balanced by chloride anions with a diffusion coefficient of $D_{Cl} = 1.97 \times 10^{-9}\ m^2/s$. The ionic strength of the mixture after adding EDC, which contains a mixture of MES, chloride, EDU, and sodium ions is

$$I_{EDU+MES} = \frac{RT\sigma + F^2 c_{EDC} D_{Na} + F^2 c_{EDC}(D_{MES} - D_{EDU} - D_{Cl})}{F^2(D_{MES} + D_{Na})}. \quad \text{(A4)}$$

The diffusion coefficient of the EDU cation is estimated as $D_{EDU} = 1 \times 10^{-9}\ m^2/s$. The concentration of EDU cations and chloride anions is equal to the initial concentration of EDC added to the solution, c_{EDC}, because all the dimethylamine groups in EDU carry a positive charge due their large pKa of 10.7. The estimated ionic strengths and Debye lengths calculated from equation (1.7) for EDC concentrations of 5 mM, 10 mM, and 15 mM are 18 mM, 23 mM, and 27 mM and 2.3 nm, 2.0 nm, and 1.8 nm, respectively. The initial Debye length of the MES buffer prior to EDC addition (2.4 nm) was used to calculate the electrostatic interactions (Φ_{elect}, equation (1.8)) prior to fuel addition in **Figure 2.6** and **Figure 2.7**, while the EDC concentration dependent Debye lengths were used to calculate the electrostatic interactions for all times after EDC addition. Measurements showed no change in the solution conductivity, and therefore the Debye length, after fuel addition.

A2. Hydra parameter estimation using ANS binding to hydrophobic groups.

8-anilino-1-naphthalenesulfonic acid (ANS) binds to hydrophobic regions of molecules and surfaces. Here, ANS binds to non – polar NHS ester groups on polystyrene during dissipative assembly following the ligand-receptor binding equilibrium,[59]

$$ANS + NHS \overset{K_B}{\leftrightarrow} ANS - NHS, \tag{A5}$$

where K_B is the equilibrium constant of binding:

$$K_B = \frac{c_{ANS-NHS}}{c_{ANS}c_{NHS}}. \tag{A6}$$

ANS has a fluorescence quantum yield of 0.003 in water and 0.4 in ethanol,[207] indicating it emits essentially no photons upon excitation in water compared to when it is bound to a non-polar molecule. Assuming that each NHS group binds the same number of ANS molecules and that the quantum yield of each ANS-NHS complex is identical, the fluorescence emission intensity from a solution of ANS and polystyrene is proportional to the number of ANS groups bound to nonpolar molecules in the solution. We believe these are reasonable assumptions given the uniformity of each particle surface and the presence of only one binding site on each ANS molecule. Further, ANS quantum yield is not sensitive to other factors such as solution pH. Subtracting the value of emission intensity prior to addition of EDC, I^0_{ANS}, from that at any time after EDC addition (I_{ANS}) removes any effects of the buffer and organic solutions on the emission intensity and yields a quantity that is proportional to the concentration of ANS-NHS complexes,

$$I_{ANS} - I^0_{ANS} \propto c_{ANS-NHS}. \tag{A7}$$

Rearranging equation (A6) and substituting equation (A7) yields,

$$I_{ANS} - I^0_{ANS} \propto K_B c_{ANS} c_{NHS}. \tag{A8}$$

ANS is in excess of total NHS groups on the polystyrene particles so c_{ANS} is constant, as is the equilibrium binding constant. Therefore, $K_B c_{ANS} = constant$ and the above expression reduces to

$$I_{ANS} - I_{ANS}^0 \propto c_{NHS}, \quad \text{(A9)}$$

showing that ANS fluorescence intensity is proportional to the number of NHS ester groups in the solution at a given time. Using this proportionality together with calibration experiments described in **Figure 2.5**, the Hydra parameter can be quantified from ANS binding experiments.

A3. Supplementary figures and data for Chapter 2

Table A1. Interaction potential model parameters used in **Figure 2.6** and **Figure 2.7**.

Hamaker constant (J)[306]	1.37×10^{-20}
Polymer thickness (nm)*	4.5
Polymer diameter (nm)*	4
D_0 (nm)*[63]	1.1
Surface energy (mJ/m^2)[307]	42
Solvent viscosity (mPa s)	0.894
Relative permittivity of water	80

*Estimated parameter

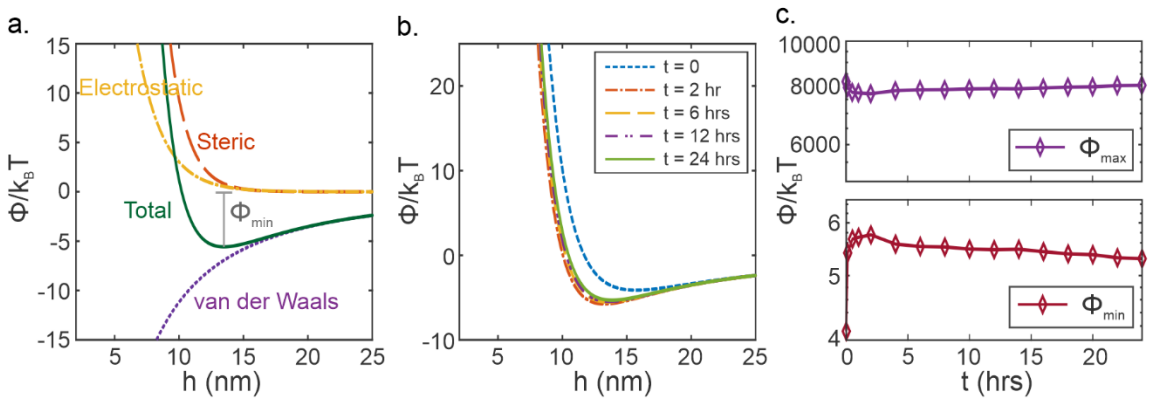

Figure A1. Interaction potential of 1 µm polystyrene particles without including hydrophobic forces at different time points after addition of 10 mM EDC. (a) Contribution of electrostatic, van der Waals and steric interactions to the total pairwise interaction potential 4 hours after adding EDC. (b) Total interaction potential curve at different times during the dissipative assembly cycle. (c) Primary maximum height (top) and secondary minimum depth (bottom) as a function of time. This plot is equivalent to **Figure 2.6** in chapter 2, but with hydrophobic forces removed.

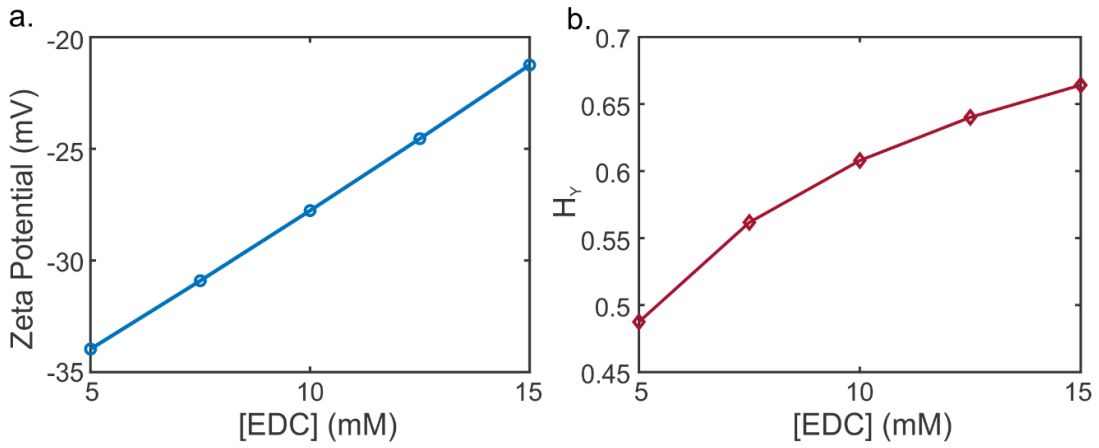

Figure A2. Fuel dependent change of (a) zeta potential and (b) Hydra parameter of 500 nm polystyrene particles when the particles were the most unstable after addition of EDC. These values were used to generate interaction potential models in **Figure 2.7**.

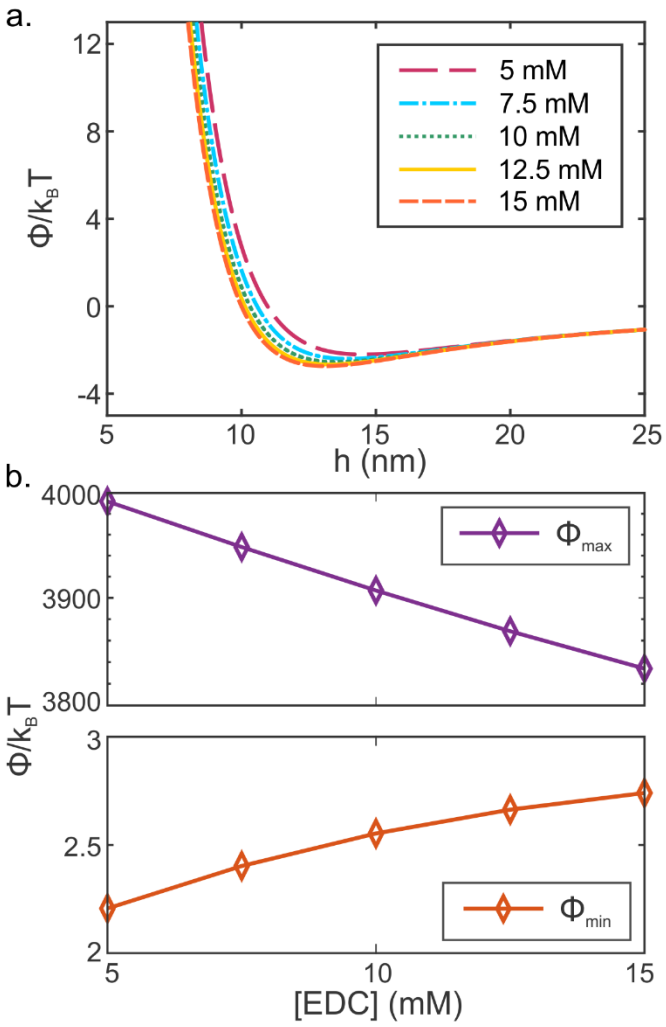

Figure A3. Interaction potential of 500 nm polystyrene excluding hydrophobic interactions when the particles are most colloidally unstable during dissipative assembly. This figure is equivalent to **Figure 2.7** with hydrophobic interactions removed from the model. (a) Interaction potential as a function of fuel concentration. (b) The primary maximum height and secondary minimum depth as a function of EDC concentration.

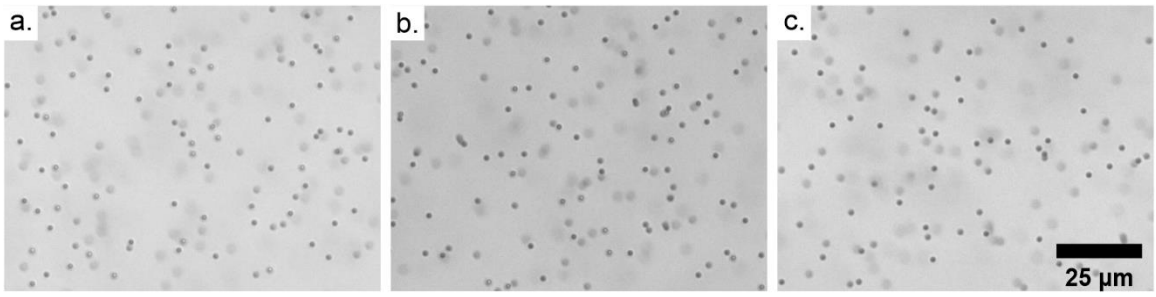

Figure A4. 1 µm polystyrene particles showed no assembly for an initial EDC concentration of 15 mM when polysorbate 20 was added to the buffer at a concentration of 0.1 mM. Particles (a) before adding EDC, (b) 6 hours after adding EDC and (c) 24 hours after adding EDC.

A4. Supplementary figures for Chapter 3

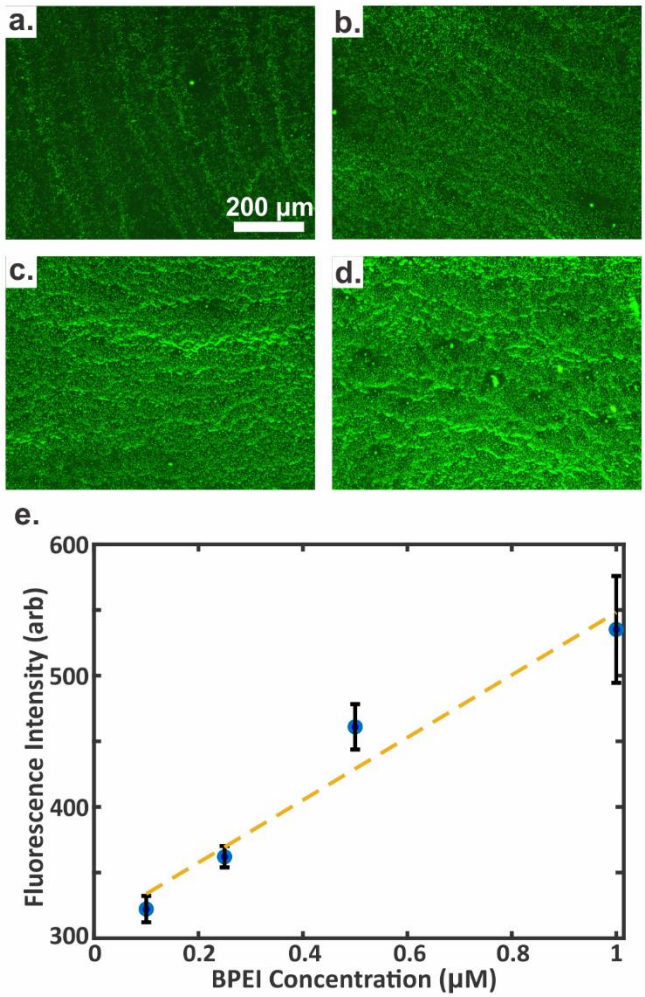

Figure A5. The change of fluorescence intensity with BPEI concentration / thickness. (a) – (d) FM images of (a) 0.1 µM (b) 0.25 µM (c) 0.5 µM and (d) 1 µM solutions of BPEI labeled with fluorescein and then dried on polished silicon. (e) The average fluorescence intensity for different concentrations of fluorescently labelled BPEI measured from FM images of the silicon chips. Error bars denote the standard deviation of the mean of three ± 1 measurements. The dashed yellow line is least squares fit to the data.

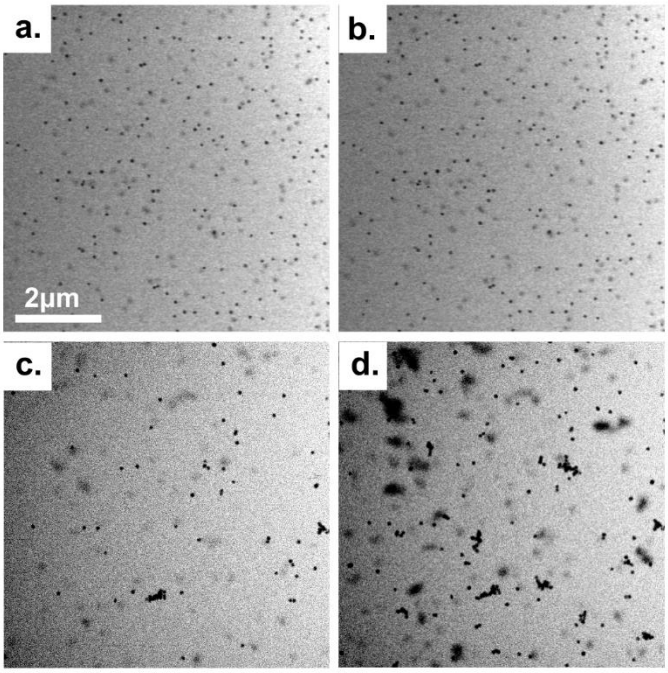

Figure A6. Nanoparticle mobility during LP-TEM imaging. (a) – (b) The region irradiated at 0.274 MGy/s for 5 minutes at (a) t = 0 and at (b) t = 5 minutes showed no nanoparticle mobility or aggregation with time. (c) – (d) The region irradiated at 0.616 MGy/s for 5 minutes at (a) t = 0 and at (b) t = 5 minutes showed some nanoparticle movement into the image area within the first few seconds.

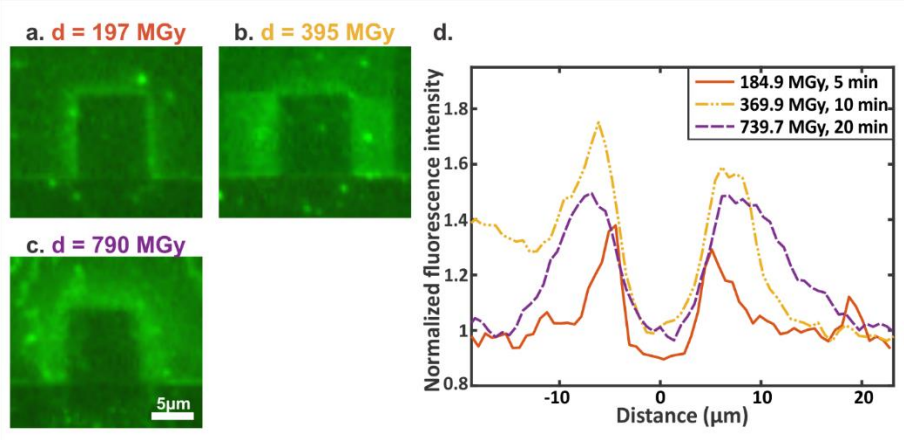

Figure A7. Effect of LP-TEM imaging time and cumulative dose on the fluorescence intensity of the labeled silicon nitride membrane for a dose rate of 0.616 MGy/s. (a) – (d)

FM images corresponding to LP-TEM images areas irradiated for times of (a) 5 minutes, (b) 10 minutes, and (c) 20 minutes. (d) Fluorescence intensity measured along a horizontal line drawn across each FM image. The fluorescence intensity for each irradiated region was normalized to the local background intensity.

Bibliography

(1) Bishop, K. J. M.; Wilmer, C. E.; Soh, S.; Grzybowski, B. A. Nanoscale Forces and Their Uses in Self-Assembly. *Small* **2009**, *5* (14), 1600–1630. https://doi.org/10.1002/smll.200900358.

(2) Whitesides, G. M.; Kriebel, J. K.; Mayers, B. T. Self-Assembly and Nanostructured Materials. In *Nanoscale Assembly: Chemical Techniques*; Huck, W. T. S., Ed.; Nanostructure Science and Technology; Springer US: Boston, MA, 2005; pp 217–239. https://doi.org/10.1007/0-387-25656-3_9.

(3) Nie, Z.; Petukhova, A.; Kumacheva, E. Properties and Emerging Applications of Self-Assembled Structures Made from Inorganic Nanoparticles. *Nature Nanotech* **2010**, *5* (1), 15–25. https://doi.org/10.1038/nnano.2009.453.

(4) Jain, P. K.; Eustis, S.; El-Sayed, M. A. Plasmon Coupling in Nanorod Assemblies: Optical Absorption, Discrete Dipole Approximation Simulation, and Exciton-Coupling Model. *J. Phys. Chem. B* **2006**, *110* (37), 18243–18253. https://doi.org/10.1021/jp063879z.

(5) Amir Parviz, B.; Ryan, D.; Whitesides, G. M. Using Self-Assembly for the Fabrication of Nano-Scale Electronic and Photonic Devices. *IEEE Transactions on Advanced Packaging* **2003**, *26* (3), 233–241. https://doi.org/10.1109/TADVP.2003.817971.

(6) Talapin, D. V.; Lee, J.-S.; Kovalenko, M. V.; Shevchenko, E. V. Prospects of Colloidal Nanocrystals for Electronic and Optoelectronic Applications. *Chem. Rev.* **2010**, *110* (1), 389–458. https://doi.org/10.1021/cr900137k.

(7) Karg, M.; König, T. A. F.; Retsch, M.; Stelling, C.; Reichstein, P. M.; Honold, T.; Thelakkat, M.; Fery, A. Colloidal Self-Assembly Concepts for Light Management in Photovoltaics. *Materials Today* **2015**, *18* (4), 185–205. https://doi.org/10.1016/j.mattod.2014.10.036.

(8) Colvin, V. L. From Opals to Optics: Colloidal Photonic Crystals. *MRS Bulletin* **2001**, *26* (8), 637–641. https://doi.org/10.1557/mrs2001.159.

(9) Himmelhaus, M.; Takei, H. Cap-Shaped Gold Nanoparticles for an Optical Biosensor. *Sensors and Actuators B: Chemical* **2000**, *63* (1), 24–30. https://doi.org/10.1016/S0925-4005(99)00393-7.

(10) Saha, K.; Agasti, S. S.; Kim, C.; Li, X.; Rotello, V. M. Gold Nanoparticles in Chemical and Biological Sensing. *Chem. Rev.* **2012**, *112* (5), 2739–2779. https://doi.org/10.1021/cr2001178.

(11) Hang, L.; Zhao, Y.; Zhang, H.; Liu, G.; Cai, W.; Li, Y.; Qu, L. Copper Nanoparticle@graphene Composite Arrays and Their Enhanced Catalytic

Performance. *Acta Materialia* **2016**, *105*, 59–67. https://doi.org/10.1016/j.actamat.2015.12.029.

(12) Zhou, J.; Duan, B.; Fang, Z.; Song, J.; Wang, C.; Messersmith, P. B.; Duan, H. Interfacial Assembly of Mussel-Inspired Au@Ag@ Polydopamine Core–Shell Nanoparticles for Recyclable Nanocatalysts. *Advanced Materials* **2014**, *26* (5), 701–705. https://doi.org/10.1002/adma.201303032.

(13) Doane, T. L.; Burda, C. The Unique Role of Nanoparticles in Nanomedicine: Imaging, Drug Delivery and Therapy. *Chem. Soc. Rev.* **2012**, *41* (7), 2885–2911. https://doi.org/10.1039/C2CS15260F.

(14) Kim, B.; Han, G.; Toley, B. J.; Kim, C.; Rotello, V. M.; Forbes, N. S. Tuning Payload Delivery in Tumour Cylindroids Using Gold Nanoparticles. *Nature Nanotech* **2010**, *5* (6), 465–472. https://doi.org/10.1038/nnano.2010.58.

(15) Grzelczak, M.; Vermant, J.; Furst, E. M.; Liz-Marzán, L. M. Directed Self-Assembly of Nanoparticles. *ACS Nano* **2010**, *4* (7), 3591–3605. https://doi.org/10.1021/nn100869j.

(16) Whitesides, G. M.; Grzybowski, B. Self-Assembly at All Scales. *Science* **2002**, *295* (5564), 2418–2421. https://doi.org/10.1126/science.1070821.

(17) Grzybowski, B. A.; Wilmer, C. E.; Kim, J.; Browne, K. P.; Bishop, K. J. M. Self-Assembly: From Crystals to Cells. *Soft Matter* **2009**, *5* (6), 1110–1128. https://doi.org/10.1039/B819321P.

(18) Merindol, R.; Walther, A. Materials Learning from Life: Concepts for Active, Adaptive and Autonomous Molecular Systems. *Chem. Soc. Rev.* **2017**, *46* (18), 5588–5619. https://doi.org/10.1039/C6CS00738D.

(19) Rossum, S. A. P. van; Tena-Solsona, M.; Esch, J. H. van; Eelkema, R.; Boekhoven, J. Dissipative Out-of-Equilibrium Assembly of Man-Made Supramolecular Materials. *Chem. Soc. Rev.* **2017**, *46* (18), 5519–5535. https://doi.org/10.1039/C7CS00246G.

(20) Arango-Restrepo, A.; Barragán, D.; Rubi, J. M. Self-Assembling Outside Equilibrium: Emergence of Structures Mediated by Dissipation. *Phys. Chem. Chem. Phys.* **2019**, *21* (32), 17475–17493. https://doi.org/10.1039/C9CP01088B.

(21) Grzybowski, B. A.; Huck, W. T. S. The Nanotechnology of Life-Inspired Systems. *Nature Nanotech* **2016**, *11* (7), 585–592. https://doi.org/10.1038/nnano.2016.116.

(22) Nozakura, T.; Ikeuchi, S. Formation of Dissipative Structures in Galaxies. *The Astrophysical Journal* **1984**, *279*, 40–52. https://doi.org/10.1086/161863.

(23) Cooper, G. M. Microtubules. In *The Cell: A Molecular Approach. 2nd edition*; Sinauer Associates, 2000.

(24) Horio, T.; Murata, T. The Role of Dynamic Instability in Microtubule Organization. *Frontiers in Plant Science* **2014**, *5*.

(25) Wang, Q.; Qi, Z.; Chen, M.; Qu, D.-H. Out-of-Equilibrium Supramolecular Self-Assembling Systems Driven by Chemical Fuel. *Aggregate* **2021**, *2* (5), e110. https://doi.org/10.1002/agt2.110.

(26) van Ravensteijn, B. G. P.; Voets, I. K.; Kegel, W. K.; Eelkema, R. Out-of-Equilibrium Colloidal Assembly Driven by Chemical Reaction Networks. *Langmuir* **2020**, *36* (36), 10639–10656. https://doi.org/10.1021/acs.langmuir.0c01763.

(27) Boekhoven, J.; Hendriksen, W. E.; Koper, G. J. M.; Eelkema, R.; van Esch, J. H. Transient Assembly of Active Materials Fueled by a Chemical Reaction. *Science* **2015**, *349* (6252), 1075–1079. https://doi.org/10.1126/science.aac6103.

(28) Dai, K.; Fores, J. R.; Wanzke, C.; Winkeljann, B.; Bergmann, A. M.; Lieleg, O.; Boekhoven, J. Regulating Chemically Fueled Peptide Assemblies by Molecular Design. *J. Am. Chem. Soc.* **2020**, *142* (33), 14142–14149. https://doi.org/10.1021/jacs.0c04203.

(29) Kriebisch, B. A. K.; Jussupow, A.; Bergmann, A. M.; Kohler, F.; Dietz, H.; Kaila, V. R. I.; Boekhoven, J. Reciprocal Coupling in Chemically Fueled Assembly: A Reaction Cycle Regulates Self-Assembly and Vice Versa. *J. Am. Chem. Soc.* **2020**, *142* (49), 20837–20844. https://doi.org/10.1021/jacs.0c10486.

(30) Nikfarjam, S.; Gibbons, R.; Burni, F.; Raghavan, S. R.; Anisimov, M. A.; Woehl, T. J. Chemically Fueled Dissipative Cross-Linking of Protein Hydrogels Mediated by Protein Unfolding. *Biomacromolecules* **2023**, *24* (3), 1131–1140. https://doi.org/10.1021/acs.biomac.2c01186.

(31) Morrow, S. M.; Colomer, I.; Fletcher, S. P. A Chemically Fuelled Self-Replicator. *Nat Commun* **2019**, *10* (1), 1011. https://doi.org/10.1038/s41467-019-08885-9.

(32) Würbser, M. A.; Schwarz, P. S.; Heckel, J.; Bergmann, A. M.; Walther, A.; Boekhoven, J. Chemically Fueled Block Copolymer Self-Assembly into Transient Nanoreactors**. *ChemSystemsChem* **2021**, *3* (5), e2100015. https://doi.org/10.1002/syst.202100015.

(33) Maiti, S.; Fortunati, I.; Ferrante, C.; Scrimin, P.; Prins, L. J. Dissipative Self-Assembly of Vesicular Nanoreactors. *Nature Chem* **2016**, *8* (7), 725–731. https://doi.org/10.1038/nchem.2511.

(34) Tena-Solsona, M.; Rieß, B.; Grötsch, R. K.; Löhrer, F. C.; Wanzke, C.; Käsdorf, B.; Bausch, A. R.; Müller-Buschbaum, P.; Lieleg, O.; Boekhoven, J. Non-Equilibrium Dissipative Supramolecular Materials with a Tunable Lifetime. *Nat Commun* **2017**, *8* (1), 15895. https://doi.org/10.1038/ncomms15895.

(35) Wanzke, C.; Tena-Solsona, M.; Rieß, B.; Tebcharani, L.; Boekhoven, J. Active Droplets in a Hydrogel Release Drugs with a Constant and Tunable Rate. *Mater. Horiz.* **2020**, *7* (5), 1397–1403. https://doi.org/10.1039/C9MH01822K.

(36) Donau, C.; Späth, F.; Sosson, M.; Kriebisch, B. A. K.; Schnitter, F.; Tena-Solsona, M.; Kang, H.-S.; Salibi, E.; Sattler, M.; Mutschler, H.; Boekhoven, J. Active Coacervate Droplets as a Model for Membraneless Organelles and Protocells. *Nat Commun* **2020**, *11* (1), 5167. https://doi.org/10.1038/s41467-020-18815-9.

(37) van Ravensteijn, B. G. P.; Hendriksen, W. E.; Eelkema, R.; van Esch, J. H.; Kegel, W. K. Fuel-Mediated Transient Clustering of Colloidal Building Blocks. *J. Am. Chem. Soc.* **2017**, *139* (29), 9763–9766. https://doi.org/10.1021/jacs.7b03263.

(38) Heuser, T.; Steppert, A.-K.; Molano Lopez, C.; Zhu, B.; Walther, A. Generic Concept to Program the Time Domain of Self-Assemblies with a Self-Regulation Mechanism. *Nano Lett.* **2015**, *15* (4), 2213–2219. https://doi.org/10.1021/nl5039506.

(39) Dehne, H.; Reitenbach, A.; Bausch, A. R. Transient Self-Organisation of DNA Coated Colloids Directed by Enzymatic Reactions. *Sci Rep* **2019**, *9* (1), 7350. https://doi.org/10.1038/s41598-019-43720-7.

(40) Grötsch, R. K.; Angı, A.; Mideksa, Y. G.; Wanzke, C.; Tena-Solsona, M.; Feige, M. J.; Rieger, B.; Boekhoven, J. Dissipative Self-Assembly of Photoluminescent Silicon Nanocrystals. *Angewandte Chemie International Edition* **2018**, *57* (44), 14608–14612. https://doi.org/10.1002/anie.201807937.

(41) Grötsch, R. K.; Wanzke, C.; Speckbacher, M.; Angı, A.; Rieger, B.; Boekhoven, J. Pathway Dependence in the Fuel-Driven Dissipative Self-Assembly of Nanoparticles. *J. Am. Chem. Soc.* **2019**, *141* (25), 9872–9878. https://doi.org/10.1021/jacs.9b02004.

(42) Ouyang, Y.; Zhang, P.; Manis-Levy, H.; Paltiel, Y.; Willner, I. Transient Dissipative Optical Properties of Aggregated Au Nanoparticles, CdSe/ZnS Quantum Dots, and Supramolecular Nucleic Acid-Stabilized Ag Nanoclusters. *J. Am. Chem. Soc.* **2021**, *143* (42), 17622–17632. https://doi.org/10.1021/jacs.1c07895.

(43) Bian, T.; Gardin, A.; Gemen, J.; Houben, L.; Perego, C.; Lee, B.; Elad, N.; Chu, Z.; Pavan, G. M.; Klajn, R. Electrostatic Co-Assembly of Nanoparticles with Oppositely Charged Small Molecules into Static and Dynamic Superstructures. *Nat. Chem.* **2021**, *13* (10), 940–949. https://doi.org/10.1038/s41557-021-00752-9.

(44) Klajn, R.; Wesson, P. J.; Bishop, K. J. M.; Grzybowski, B. A. Writing Self-Erasing Images Using Metastable Nanoparticle "Inks." *Angewandte Chemie International Edition* **2009**, *48* (38), 7035–7039. https://doi.org/10.1002/anie.200901119.

(45) Samanta, D.; Klajn, R. Aqueous Light-Controlled Self-Assembly of Nanoparticles. *Advanced Optical Materials* **2016**, *4* (9), 1373–1377. https://doi.org/10.1002/adom.201600364.

(46) Wei, Y.; Han, S.; Kim, J.; Soh, S.; Grzybowski, B. A. Photoswitchable Catalysis Mediated by Dynamic Aggregation of Nanoparticles. *J. Am. Chem. Soc.* **2010**, *132* (32), 11018–11020. https://doi.org/10.1021/ja104260n.

(47) Chovnik, O.; Balgley, R.; Goldman, J. R.; Klajn, R. Dynamically Self-Assembling Carriers Enable Guiding of Diamagnetic Particles by Weak Magnets. *J. Am. Chem. Soc.* **2012**, *134* (48), 19564–19567. https://doi.org/10.1021/ja309633v.

(48) Zhao, H.; Sen, S.; Udayabhaskararao, T.; Sawczyk, M.; Kučanda, K.; Manna, D.; Kundu, P. K.; Lee, J.-W.; Král, P.; Klajn, R. Reversible Trapping and Reaction Acceleration within Dynamically Self-Assembling Nanoflasks. *Nature Nanotech* **2016**, *11* (1), 82–88. https://doi.org/10.1038/nnano.2015.256.

(49) Vialetto, J.; Anyfantakis, M.; Rudiuk, S.; Morel, M.; Baigl, D. Photoswitchable Dissipative Two-Dimensional Colloidal Crystals. *Angewandte Chemie International Edition* **2019**, *58* (27), 9145–9149. https://doi.org/10.1002/anie.201904093.

(50) Berg, J. C. *An Introduction to Interfaces & Colloids: The Bridge to Nanoscience*; World Scientific, 2010.

(51) Israelachvili, J. N. *Intermolecular and Surface Forces*; Academic Press, 2011.

(52) Behrens, S. H.; Borkovec, M. Influence of the Secondary Interaction Energy Minimum on the Early Stages of Colloidal Aggregation. *Journal of Colloid and Interface Science* **2000**, *225* (2), 460–465. https://doi.org/10.1006/jcis.2000.6780.

(53) Buhmann, S. Y.; Welsch, D.-G. Dispersion Forces in Macroscopic Quantum Electrodynamics. *Progress in Quantum Electronics* **2007**, *31* (2), 51–130. https://doi.org/10.1016/j.pquantelec.2007.03.001.

(54) Parsegian, V. A. *Van Der Waals Forces: A Handbook for Biologists, Chemists, Engineers, and Physicists*; Cambridge University Press: New York, 2006.

(55) Russel, W. B.; Saville, D. A.; Schowalter, W. R. *Colloidal Dispersions*; Cambridge Monographs on Mechanics; Cambridge University Press: Cambridge, 1989. https://doi.org/10.1017/CBO9780511608810.

(56) Hunter, R. J. *Foundations of Colloid Science*, 2nd ed.; Oxford University Press: Oxford ; New York, 2001.

(57) Fritz, G.; Schädler, V.; Willenbacher, N.; Wagner, N. J. Electrosteric Stabilization of Colloidal Dispersions. *Langmuir* **2002**, *18* (16), 6381–6390. https://doi.org/10.1021/la015734j.

(58) de Gennes, P. G. Polymers at an Interface; a Simplified View. *Advances in Colloid and Interface Science* **1987**, *27* (3), 189–209. https://doi.org/10.1016/0001-8686(87)85003-0.

(59) Sánchez-Iglesias, A.; Grzelczak, M.; Altantzis, T.; Goris, B.; Pérez-Juste, J.; Bals, S.; Van Tendeloo, G.; Donaldson, S. H. Jr.; Chmelka, B. F.; Israelachvili, J. N.; Liz-Marzán, L. M. Hydrophobic Interactions Modulate Self-Assembly of Nanoparticles. *ACS Nano* **2012**, *6* (12), 11059–11065. https://doi.org/10.1021/nn3047605.

(60) Israelachvili, J.; Wennerström, H. Role of Hydration and Water Structure in Biological and Colloidal Interactions. *Nature* **1996**, *379* (6562), 219–225. https://doi.org/10.1038/379219a0.

(61) Liang, Y.; Hilal, N.; Langston, P.; Starov, V. Interaction Forces between Colloidal Particles in Liquid: Theory and Experiment. *Advances in Colloid and Interface Science* **2007**, *134–135*, 151–166. https://doi.org/10.1016/j.cis.2007.04.003.

(62) Southall, N. T.; Dill, K. A.; Haymet, A. D. J. A View of the Hydrophobic Effect. *J. Phys. Chem. B* **2002**, *106* (3), 521–533. https://doi.org/10.1021/jp015514e.

(63) Donaldson, S. H. Jr.; Røyne, A.; Kristiansen, K.; Rapp, M. V.; Das, S.; Gebbie, M. A.; Lee, D. W.; Stock, P.; Valtiner, M.; Israelachvili, J. Developing a General Interaction Potential for Hydrophobic and Hydrophilic Interactions. *Langmuir* **2015**, *31* (7), 2051–2064. https://doi.org/10.1021/la502115g.

(64) Meyer, E. E.; Rosenberg, K. J.; Israelachvili, J. Recent Progress in Understanding Hydrophobic Interactions. *Proceedings of the National Academy of Sciences* **2006**, *103* (43), 15739–15746. https://doi.org/10.1073/pnas.0606422103.

(65) Tabor, R. F.; Grieser, F.; Dagastine, R. R.; Chan, D. Y. C. The Hydrophobic Force: Measurements and Methods. *Phys. Chem. Chem. Phys.* **2014**, *16* (34), 18065–18075. https://doi.org/10.1039/C4CP01410C.

(66) Donaldson, S. H. Jr.; Das, S.; Gebbie, M. A.; Rapp, M.; Jones, L. C.; Roiter, Y.; Koenig, P. H.; Gizaw, Y.; Israelachvili, J. N. Asymmetric Electrostatic and Hydrophobic–Hydrophilic Interaction Forces between Mica Surfaces and Silicone Polymer Thin Films. *ACS Nano* **2013**, *7* (11), 10094–10104. https://doi.org/10.1021/nn4050112.

(67) Alessio, B. M.; Gupta, A. Diffusiophoresis-Enhanced Turing Patterns. May 19, 2023. https://doi.org/10.48550/arXiv.2305.11372.

(68) Vadde, B. V. L.; Roeder, A. H. K. Can the French Flag and Reaction–Diffusion Models Explain Flower Patterning? Celebrating the 50th Anniversary of the French Flag Model. *Journal of Experimental Botany* **2020**, *71* (10), 2886–2897. https://doi.org/10.1093/jxb/eraa065.

(69) Fowler, D. R.; Meinhardt, H.; Prusinkiewicz, P. Modeling Seashells. *SIGGRAPH Comput. Graph.* **1992**, *26* (2), 379–387. https://doi.org/10.1145/142920.134096.

(70) Kondo, S. The Reaction-Diffusion System: A Mechanism for Autonomous Pattern Formation in the Animal Skin. *Genes to Cells* **2002**, *7* (6), 535–541. https://doi.org/10.1046/j.1365-2443.2002.00543.x.

(71) Prum, R. O.; Williamson, S. Reaction-Diffusion Models of within-Feather Pigmentation Patterning. *Proceedings: Biological Sciences* **2002**, *269* (1493), 781–792.

(72) Halatek, J.; Brauns, F.; Frey, E. Self-Organization Principles of Intracellular Pattern Formation. *Philosophical Transactions of the Royal Society B: Biological Sciences* **2018**, *373* (1747), 20170107. https://doi.org/10.1098/rstb.2017.0107.

(73) Soh, S.; Byrska, M.; Kandere-Grzybowska, K.; Grzybowski, B. A. Reaction - Diffusion Systems in Intracellular Molecular Transport and Control. *Angew Chem Int Ed Engl* **2010**, *49* (25), 4170–4198. https://doi.org/10.1002/anie.200905513.

(74) Turing, A. M. The Chemical Basis of Morphogenesis. *Philosophical Transactions of the Royal Society of London. Series B, Biological Sciences* **1952**, *237* (641), 37–72. https://doi.org/10.1098/rstb.1952.0012.

(75) Gierer, A.; Meinhardt, H. A Theory of Biological Pattern Formation. *Kybernetik* **1972**, *12* (1), 30–39. https://doi.org/10.1007/BF00289234.

(76) Cooper, R. L.; Thiery, A. P.; Fletcher, A. G.; Delbarre, D. J.; Rasch, L. J.; Fraser, G. J. An Ancient Turing-like Patterning Mechanism Regulates Skin Denticle Development in Sharks. *Science Advances* **2018**, *4* (11), eaau5484. https://doi.org/10.1126/sciadv.aau5484.

(77) Konow, C.; Li, Z.; Shepherd, S.; Bullara, D.; Epstein, I. R. Influence of Survival, Promotion, and Growth on Pattern Formation in Zebrafish Skin. *Sci Rep* **2021**, *11* (1), 9864. https://doi.org/10.1038/s41598-021-89116-4.

(78) Mahalwar, P.; Walderich, B.; Singh, A. P.; Nüsslein-Volhard, C. Local Reorganization of Xanthophores Fine-Tunes and Colors the Striped Pattern of Zebrafish. *Science* **2014**, *345* (6202), 1362–1364. https://doi.org/10.1126/science.1254837.

(79) Ishida, T. A Model of Octopus Epidermis Pattern Mimicry Mechanisms Using Inverse Operation of the Turing Reaction Model. *PLOS ONE* **2021**, *16* (8), e0256025. https://doi.org/10.1371/journal.pone.0256025.

(80) Meinhardt, H. *The Algorithmic Beauty of Sea Shells*; Prusinkiewicz, P., Series Ed.; The Virtual Laboratory; Springer: Berlin, Heidelberg, 1995. https://doi.org/10.1007/978-3-662-13135-0.

(81) Haupaix, N.; Curantz, C.; Bailleul, R.; Beck, S.; Robic, A.; Manceau, M. The Periodic Coloration in Birds Forms through a Prepattern of Somite Origin. *Science* **2018**, *361* (6408), eaar4777. https://doi.org/10.1126/science.aar4777.

(82) Onimaru, K.; Marcon, L.; Musy, M.; Tanaka, M.; Sharpe, J. The Fin-to-Limb Transition as the Re-Organization of a Turing Pattern. *Nat Commun* **2016**, *7* (1), 11582. https://doi.org/10.1038/ncomms11582.

(83) Harris, M. P.; Williamson, S.; Fallon, J. F.; Meinhardt, H.; Prum, R. O. Molecular Evidence for an Activator–Inhibitor Mechanism in Development of Embryonic Feather Branching. *Proceedings of the National Academy of Sciences* **2005**, *102* (33), 11734–11739. https://doi.org/10.1073/pnas.0500781102.

(84) Hearn, D. J. Turing-like Mechanism in a Stochastic Reaction-Diffusion Model Recreates Three Dimensional Vascular Patterning of Plant Stems. *PLOS ONE* **2019**, *14* (7), e0219055. https://doi.org/10.1371/journal.pone.0219055.

(85) Badugu, A.; Kraemer, C.; Germann, P.; Menshykau, D.; Iber, D. Digit Patterning during Limb Development as a Result of the BMP-Receptor Interaction. *Sci Rep* **2012**, *2* (1), 991. https://doi.org/10.1038/srep00991.

(86) Weber, E. L.; Woolley, T. E.; Yeh, C.-Y.; Ou, K.-L.; Maini, P. K.; Chuong, C.-M. Self-Organizing Hair Peg-like Structures from Dissociated Skin Progenitor Cells: New Insights for Human Hair Follicle Organoid Engineering and Turing Patterning in an Asymmetric Morphogenetic Field. *Experimental Dermatology* **2019**, *28* (4), 355–366. https://doi.org/10.1111/exd.13891.

(87) Ball, P. In Retrospect: The Physics of Sand Dunes. *Nature* **2009**, *457* (7233), 1084–1085. https://doi.org/10.1038/4571084a.

(88) Zincenko, A.; Petrovskii, S.; Volpert, V.; Banerjee, M. Turing Instability in an Economic–Demographic Dynamical System May Lead to Pattern Formation on a Geographical Scale. *Journal of The Royal Society Interface* **2021**, *18* (177), 20210034. https://doi.org/10.1098/rsif.2021.0034.

(89) Duran-Nebreda, S.; Pla, J.; Vidiella, B.; Piñero, J.; Conde-Pueyo, N.; Solé, R. Synthetic Lateral Inhibition in Periodic Pattern Forming Microbial Colonies. *ACS Synth. Biol.* **2021**, *10* (2), 277–285. https://doi.org/10.1021/acssynbio.0c00318.

(90) Karig, D.; Martini, K. M.; Lu, T.; DeLateur, N. A.; Goldenfeld, N.; Weiss, R. Stochastic Turing Patterns in a Synthetic Bacterial Population. *Proceedings of the National Academy of Sciences* **2018**, *115* (26), 6572–6577. https://doi.org/10.1073/pnas.1720770115.

(91) Rosemeier, J.; Spichtinger, P. Pattern Formation in Clouds via Turing Instabilities. *Mathematics of Climate and Weather Forecasting* **2020**, *6* (1), 75–96. https://doi.org/10.1515/mcwf-2020-0104.

(92) Nguindjel, A.-D. C.; Visser, P. J. de; Winkens, M.; Korevaar, P. A. Spatial Programming of Self-Organizing Chemical Systems Using Sustained Physicochemical Gradients from Reaction, Diffusion and Hydrodynamics. *Phys.*

Chem. Chem. Phys. **2022**, *24* (39), 23980–24001. https://doi.org/10.1039/D2CP02542F.

(93) Crampin, E.; Maini, P. Reaction-Diffusion Models for Biological Pattern Formation. **2001**.

(94) Marciniak-Czochra, A. 8.1 Reaction-Diffusion Models of Pattern Formation in Developmental Biology. In *8.1 Reaction-Diffusion Models of Pattern Formation in Developmental Biology*; De Gruyter, 2012; pp 191–212. https://doi.org/10.1515/9783110288537.191.

(95) Ruuth, S. J. Implicit-Explicit Methods for Reaction-Diffusion Problems in Pattern Formation. *J. Math. Biol.* **1995**, *34* (2), 148–176. https://doi.org/10.1007/BF00178771.

(96) Yang, L.; Dolnik, M.; Zhabotinsky, A. M.; Epstein, I. R. Turing Patterns beyond Hexagons and Stripes. *Chaos: An Interdisciplinary Journal of Nonlinear Science* **2006**, *16* (3), 037114. https://doi.org/10.1063/1.2214167.

(97) Castets, V.; Dulos, E.; Boissonade, J.; De Kepper, P. Experimental Evidence of a Sustained Standing Turing-Type Nonequilibrium Chemical Pattern. *Phys. Rev. Lett.* **1990**, *64* (24), 2953–2956. https://doi.org/10.1103/PhysRevLett.64.2953.

(98) Noszticzius, Z.; Qi, O.; McCormick, W. D.; Swinney, H. L. Effect of Turing Pattern Indicators on CIMA Oscillators. *J. Phys. Chem.* **1992**, *96* (15), 6302–6307. https://doi.org/10.1021/j100194a038.

(99) Lee, K. J.; McCormick, W. D.; Swinney, H. L.; Noszticzius, Z. Turing Patterns Visualized by Index of Refraction Variations. *The Journal of Chemical Physics* **1992**, *96* (5), 4048–4049. https://doi.org/10.1063/1.461860.

(100) Asakura, K.; Konishi, R.; Nakatani, T.; Nakano, T.; Kamata, M. Turing Pattern Formation by the CIMA Reaction in a Chemical System Consisting of Quaternary Alkyl Ammonium Cationic Groups. *J. Phys. Chem. B* **2011**, *115* (14), 3959–3963. https://doi.org/10.1021/jp111584u.

(101) Bánsági, T.; Vanag, V. K.; Epstein, I. R. Tomography of Reaction-Diffusion Microemulsions Reveals Three-Dimensional Turing Patterns. *Science* **2011**, *331* (6022), 1309–1312. https://doi.org/10.1126/science.1200815.

(102) Szalai, I.; De Kepper, P. Pattern Formation in the Ferrocyanide-Iodate-Sulfite Reaction: The Control of Space Scale Separation. *Chaos: An Interdisciplinary Journal of Nonlinear Science* **2008**, *18* (2), 026105. https://doi.org/10.1063/1.2912719.

(103) Horváth, J.; Szalai, I.; De Kepper, P. An Experimental Design Method Leading to Chemical Turing Patterns. *Science* **2009**, *324* (5928), 772–775. https://doi.org/10.1126/science.1169973.

(104) Tan, Z.; Chen, S.; Peng, X.; Zhang, L.; Gao, C. Polyamide Membranes with Nanoscale Turing Structures for Water Purification. *Science* **2018**, *360* (6388), 518–521. https://doi.org/10.1126/science.aar6308.

(105) Fang, A.; Adamo, C.; Jia, S.; Cava, R. J.; Wu, S.-C.; Felser, C.; Kapitulnik, A. Bursting at the Seams: Rippled Monolayer Bismuth on NbSe2. *Science Advances* **2018**, *4* (4), eaaq0330. https://doi.org/10.1126/sciadv.aaq0330.

(106) Fuseya, Y.; Katsuno, H.; Behnia, K.; Kapitulnik, A. Nanoscale Turing Patterns in a Bismuth Monolayer. *Nat. Phys.* **2021**, *17* (9), 1031–1036. https://doi.org/10.1038/s41567-021-01288-y.

(107) Andrade-Silva, I.; Bortolozzo, U.; Clerc, M. G.; González-Cortés, G.; Residori, S.; Wilson, M. Spontaneous Light-Induced Turing Patterns in a Dye-Doped Twisted Nematic Layer. *Sci Rep* **2018**, *8* (1), 12867. https://doi.org/10.1038/s41598-018-31206-x.

(108) An, H.; Smith, J. W.; Ji, B.; Cotty, S.; Zhou, S.; Yao, L.; Kalutantirige, F. C.; Chen, W.; Ou, Z.; Su, X.; Feng, J.; Chen, Q. Mechanism and Performance Relevance of Nanomorphogenesis in Polyamide Films Revealed by Quantitative 3D Imaging and Machine Learning. *Science Advances* **2022**, *8* (8), eabk1888. https://doi.org/10.1126/sciadv.abk1888.

(109) Jiao, C.; Song, X.; Zhang, X.; Sun, L.; Jiang, H. MOF-Mediated Interfacial Polymerization to Fabricate Polyamide Membranes with a Homogeneous Nanoscale Striped Turing Structure for CO2/CH4 Separation. *ACS Appl. Mater. Interfaces* **2021**, *13* (15), 18380–18388. https://doi.org/10.1021/acsami.1c03737.

(110) Tang, M.-J.; Liu, M.-L.; Wang, D.-A.; Shao, D.-D.; Wang, H.-J.; Cui, Z.; Cao, X.-L.; Sun, S.-P. Precisely Patterned Nanostrand Surface of Cucurbituril[n]-Based Nanofiltration Membranes for Effective Alcohol–Water Condensation. *Nano Lett.* **2020**, *20* (4), 2717–2723. https://doi.org/10.1021/acs.nanolett.0c00344.

(111) de Jonge, N.; Ross, F. M. Electron Microscopy of Specimens in Liquid. *Nature Nanotech* **2011**, *6* (11), 695–704. https://doi.org/10.1038/nnano.2011.161.

(112) Ross, F. M. Opportunities and Challenges in Liquid Cell Electron Microscopy. *Science* **2015**, *350* (6267), aaa9886. https://doi.org/10.1126/science.aaa9886.

(113) Wang, M.; Park, C.; Woehl, T. J. Quantifying the Nucleation and Growth Kinetics of Electron Beam Nanochemistry with Liquid Cell Scanning Transmission Electron Microscopy. *Chem. Mater.* **2018**, *30* (21), 7727–7736. https://doi.org/10.1021/acs.chemmater.8b03050.

(114) Nielsen, M. H.; Aloni, S.; De Yoreo, J. J. In Situ TEM Imaging of CaCO3 Nucleation Reveals Coexistence of Direct and Indirect Pathways. *Science* **2014**, *345* (6201), 1158–1162. https://doi.org/10.1126/science.1254051.

(115) Smith, B. J.; Parent, L. R.; Overholts, A. C.; Beaucage, P. A.; Bisbey, R. P.; Chavez, A. D.; Hwang, N.; Park, C.; Evans, A. M.; Gianneschi, N. C.; Dichtel, W. R. Colloidal Covalent Organic Frameworks. *ACS Cent. Sci.* **2017**, *3* (1), 58–65. https://doi.org/10.1021/acscentsci.6b00331.

(116) Tan, S. F.; Bisht, G.; Anand, U.; Bosman, M.; Yong, X. E.; Mirsaidov, U. In Situ Kinetic and Thermodynamic Growth Control of Au–Pd Core–Shell Nanoparticles. *J. Am. Chem. Soc.* **2018**, *140* (37), 11680–11685. https://doi.org/10.1021/jacs.8b05217.

(117) Scheutz, G. M.; Touve, M. A.; Carlini, A. S.; Garrison, J. B.; Gnanasekaran, K.; Sumerlin, B. S.; Gianneschi, N. C. Probing Thermoresponsive Polymerization-Induced Self-Assembly with Variable-Temperature Liquid-Cell Transmission Electron Microscopy. *Matter* **2021**, *4* (2), 722–736. https://doi.org/10.1016/j.matt.2020.11.017.

(118) Korpanty, J.; Parent, L. R.; Hampu, N.; Weigand, S.; Gianneschi, N. C. Thermoresponsive Polymer Assemblies via Variable Temperature Liquid-Phase Transmission Electron Microscopy and Small Angle X-Ray Scattering. *Nat Commun* **2021**, *12* (1), 6568. https://doi.org/10.1038/s41467-021-26773-z.

(119) Mehdi, B. L.; Qian, J.; Nasybulin, E.; Park, C.; Welch, D. A.; Faller, R.; Mehta, H.; Henderson, W. A.; Xu, W.; Wang, C. M.; Evans, J. E.; Liu, J.; Zhang, J.-G.; Mueller, K. T.; Browning, N. D. Observation and Quantification of Nanoscale Processes in Lithium Batteries by Operando Electrochemical (S)TEM. *Nano Lett.* **2015**, *15* (3), 2168–2173. https://doi.org/10.1021/acs.nanolett.5b00175.

(120) Lee, S.-Y.; Shangguan, J.; Alvarado, J.; Betzler, S.; Harris, S. J.; Doeff, M. M.; Zheng, H. Unveiling the Mechanisms of Lithium Dendrite Suppression by Cationic Polymer Film Induced Solid–Electrolyte Interphase Modification. *Energy Environ. Sci.* **2020**, *13* (6), 1832–1842. https://doi.org/10.1039/D0EE00518E.

(121) Yang, R.; Mei, L.; Fan, Y.; Zhang, Q.; Liao, H.-G.; Yang, J.; Li, J.; Zeng, Z. Fabrication of Liquid Cell for in Situ Transmission Electron Microscopy of Electrochemical Processes. *Nat Protoc* **2023**, *18* (2), 555–578. https://doi.org/10.1038/s41596-022-00762-y.

(122) Lee, J.; Nakouzi, E.; Song, M.; Wang, B.; Chun, J.; Li, D. Mechanistic Understanding of the Growth Kinetics and Dynamics of Nanoparticle Superlattices by Coupling Interparticle Forces from Real-Time Measurements. *ACS Nano* **2018**, *12* (12), 12778–12787. https://doi.org/10.1021/acsnano.8b07880.

(123) Chen, Q.; Smith, J. M.; Park, J.; Kim, K.; Ho, D.; Rasool, H. I.; Zettl, A.; Alivisatos, A. P. 3D Motion of DNA-Au Nanoconjugates in Graphene Liquid Cell Electron Microscopy. *Nano Lett.* **2013**, *13* (9), 4556–4561. https://doi.org/10.1021/nl402694n.

(124) de Jonge, N. Theory of the Spatial Resolution of (Scanning) Transmission Electron Microscopy in Liquid Water or Ice Layers. *Ultramicroscopy* **2018**, *187*, 113–125. https://doi.org/10.1016/j.ultramic.2018.01.007.

(125) Park, J.; Koo, K.; Noh, N.; Chang, J. H.; Cheong, J. Y.; Dae, K. S.; Park, J. S.; Ji, S.; Kim, I.-D.; Yuk, J. M. Graphene Liquid Cell Electron Microscopy: Progress, Applications, and Perspectives. *ACS Nano* **2021**, *15* (1), 288–308. https://doi.org/10.1021/acsnano.0c10229.

(126) Yuk, J. M.; Park, J.; Ercius, P.; Kim, K.; Hellebusch, D. J.; Crommie, M. F.; Lee, J. Y.; Zettl, A.; Alivisatos, A. P. High-Resolution EM of Colloidal Nanocrystal Growth Using Graphene Liquid Cells. *Science* **2012**, *336* (6077), 61–64. https://doi.org/10.1126/science.1217654.

(127) Textor, M.; de Jonge, N. Strategies for Preparing Graphene Liquid Cells for Transmission Electron Microscopy. *Nano Lett.* **2018**, *18* (6), 3313–3321. https://doi.org/10.1021/acs.nanolett.8b01366.

(128) Jokisaari, J. R.; Hachtel, J. A.; Hu, X.; Mukherjee, A.; Wang, C.; Konecna, A.; Lovejoy, T. C.; Dellby, N.; Aizpurua, J.; Krivanek, O. L.; Idrobo, J.-C.; Klie, R. F. Vibrational Spectroscopy of Water with High Spatial Resolution. *Advanced Materials* **2018**, *30* (36), 1802702. https://doi.org/10.1002/adma.201802702.

(129) Yang, J.; Choi, M. K.; Sheng, Y.; Jung, J.; Bustillo, K.; Chen, T.; Lee, S.-W.; Ercius, P.; Kim, J. H.; Warner, J. H.; Chan, E. M.; Zheng, H. MoS2 Liquid Cell Electron Microscopy Through Clean and Fast Polymer-Free MoS2 Transfer. *Nano Lett.* **2019**, *19* (3), 1788–1795. https://doi.org/10.1021/acs.nanolett.8b04821.

(130) Rasool, H.; Dunn, G.; Fathalizadeh, A.; Zettl, A. Graphene-Sealed Si/SiN Cavities for High-Resolution in Situ Electron Microscopy of Nano-Confined Solutions. *physica status solidi (b)* **2016**, *253* (12), 2351–2354. https://doi.org/10.1002/pssb.201600232.

(131) Kelly, D. J.; Zhou, M.; Clark, N.; Hamer, M. J.; Lewis, E. A.; Rakowski, A. M.; Haigh, S. J.; Gorbachev, R. V. Nanometer Resolution Elemental Mapping in Graphene-Based TEM Liquid Cells. *Nano Lett.* **2018**, *18* (2), 1168–1174. https://doi.org/10.1021/acs.nanolett.7b04713.

(132) Noh, N.; Park, J.; Park, J. S.; Koo, K.; Park, J. Y.; Yuk, J. M. Lithographically Patterned Well-Type Graphene Liquid Cells with Rational Designs. *Lab Chip* **2020**, *20* (15), 2796–2803. https://doi.org/10.1039/D0LC00440E.

(133) Koo, K.; Park, J.; Ji, S.; Toleukhanova, S.; Yuk, J. M. Liquid-Flowing Graphene Chip-Based High-Resolution Electron Microscopy. *Advanced Materials* **2021**, *33* (2), 2005468. https://doi.org/10.1002/adma.202005468.

(134) Chen, L.; Leonardi, A.; Chen, J.; Cao, M.; Li, N.; Su, D.; Zhang, Q.; Engel, M.; Ye, X. Imaging the Kinetics of Anisotropic Dissolution of Bimetallic Core–Shell Nanocubes Using Graphene Liquid Cells. *Nat Commun* **2020**, *11* (1), 3041. https://doi.org/10.1038/s41467-020-16645-3.

(135) Woehl, T. J.; Prozorov, T. The Mechanisms for Nanoparticle Surface Diffusion and Chain Self-Assembly Determined from Real-Time Nanoscale Kinetics in Liquid. *J. Phys. Chem. C* **2015**, *119* (36), 21261–21269. https://doi.org/10.1021/acs.jpcc.5b07164.

(136) Cepeda-Pérez, E.; de Jonge, N. Dynamics of Gold Nanoparticle Clusters Observed with Liquid-Phase Electron Microscopy. *Micron* **2019**, *117*, 68–75. https://doi.org/10.1016/j.micron.2018.11.006.

(137) Kim, J.; Ou, Z.; Jones, M. R.; Song, X.; Chen, Q. Imaging the Polymerization of Multivalent Nanoparticles in Solution. *Nat Commun* **2017**, *8* (1), 761. https://doi.org/10.1038/s41467-017-00857-1.

(138) Sutter, E.; Sutter, P.; Tkachenko, A. V.; Krahne, R.; de Graaf, J.; Arciniegas, M.; Manna, L. In Situ Microscopy of the Self-Assembly of Branched Nanocrystals in Solution. *Nat Commun* **2016**, *7* (1), 11213. https://doi.org/10.1038/ncomms11213.

(139) Liu, Y.; Lin, X.-M.; Sun, Y.; Rajh, T. In Situ Visualization of Self-Assembly of Charged Gold Nanoparticles. *J. Am. Chem. Soc.* **2013**, *135* (10), 3764–3767. https://doi.org/10.1021/ja312620e.

(140) Zhu, C.; Liang, S.; Song, E.; Zhou, Y.; Wang, W.; Shan, F.; Shi, Y.; Hao, C.; Yin, K.; Zhang, T.; Liu, J.; Zheng, H.; Sun, L. In-Situ Liquid Cell Transmission Electron Microscopy Investigation on Oriented Attachment of Gold Nanoparticles. *Nat Commun* **2018**, *9* (1), 421. https://doi.org/10.1038/s41467-018-02925-6.

(141) Park, J.; Zheng, H.; Lee, W. C.; Geissler, P. L.; Rabani, E.; Alivisatos, A. P. Direct Observation of Nanoparticle Superlattice Formation by Using Liquid Cell Transmission Electron Microscopy. *ACS Nano* **2012**, *6* (3), 2078–2085. https://doi.org/10.1021/nn203837m.

(142) Yang, J.; Andrei, C. M.; Chan, Y.; Mehdi, B. L.; Browning, N. D.; Botton, G. A.; Soleymani, L. Liquid Cell Transmission Electron Microscopy Sheds Light on The Mechanism of Palladium Electrodeposition. *Langmuir* **2019**, *35* (4), 862–869. https://doi.org/10.1021/acs.langmuir.8b02846.

(143) Yang, J.; Alam, S. B.; Yu, L.; Chan, E.; Zheng, H. Dynamic Behavior of Nanoscale Liquids in Graphene Liquid Cells Revealed by in Situ Transmission Electron Microscopy. *Micron* **2019**, *116*, 22–29. https://doi.org/10.1016/j.micron.2018.09.009.

(144) Wang, X.; Yang, J.; Andrei, C. M.; Soleymani, L.; Grandfield, K. Biomineralization of Calcium Phosphate Revealed by in Situ Liquid-Phase Electron Microscopy. *Commun Chem* **2018**, *1* (1), 1–7. https://doi.org/10.1038/s42004-018-0081-4.

(145) Touve, M. A.; Figg, C. A.; Wright, D. B.; Park, C.; Cantlon, J.; Sumerlin, B. S.; Gianneschi, N. C. Polymerization-Induced Self-Assembly of Micelles Observed by

Liquid Cell Transmission Electron Microscopy. *ACS Cent. Sci.* **2018**, *4* (5), 543–547. https://doi.org/10.1021/acscentsci.8b00148.

(146) Wang, H.; Nagamanasa, K. H.; Kim, Y.-J.; Kwon, O.-H.; Granick, S. Longer-Lasting Electron-Based Microscopy of Single Molecules in Aqueous Medium. *ACS Nano* **2018**, *12* (8), 8572–8578. https://doi.org/10.1021/acsnano.8b04190.

(147) Wang, H.; Li, B.; Kim, Y.-J.; Kwon, O.-H.; Granick, S. Intermediate States of Molecular Self-Assembly from Liquid-Cell Electron Microscopy. *Proceedings of the National Academy of Sciences* **2020**, *117* (3), 1283–1292. https://doi.org/10.1073/pnas.1916065117.

(148) Keskin, S.; de Jonge, N. Reduced Radiation Damage in Transmission Electron Microscopy of Proteins in Graphene Liquid Cells. *Nano Lett.* **2018**, *18* (12), 7435–7440. https://doi.org/10.1021/acs.nanolett.8b02490.

(149) Prozorov, T.; Almeida, T. P.; Kovács, A.; Dunin-Borkowski, R. E. Off-Axis Electron Holography of Bacterial Cells and Magnetic Nanoparticles in Liquid. *Journal of The Royal Society Interface* **2017**, *14* (135), 20170464. https://doi.org/10.1098/rsif.2017.0464.

(150) Tan, S. F.; Anand, U.; Mirsaidov, U. Interactions and Attachment Pathways between Functionalized Gold Nanorods. *ACS Nano* **2017**, *11* (2), 1633–1640. https://doi.org/10.1021/acsnano.6b07398.

(151) Luo, B.; Smith, J. W.; Ou, Z.; Chen, Q. Quantifying the Self-Assembly Behavior of Anisotropic Nanoparticles Using Liquid-Phase Transmission Electron Microscopy. *Acc. Chem. Res.* **2017**, *50* (5), 1125–1133. https://doi.org/10.1021/acs.accounts.7b00048.

(152) Wang, Y.; Peng, X.; Abelson, A.; Xiao, P.; Qian, C.; Yu, L.; Ophus, C.; Ercius, P.; Wang, L.-W.; Law, M.; Zheng, H. Dynamic Deformability of Individual PbSe Nanocrystals during Superlattice Phase Transitions. *Science Advances* **2019**, *5* (6), eaaw5623. https://doi.org/10.1126/sciadv.aaw5623.

(153) Liu, C.; Ou, Z.; Guo, F.; Luo, B.; Chen, W.; Qi, L.; Chen, Q. "Colloid–Atom Duality" in the Assembly Dynamics of Concave Gold Nanoarrows. *J. Am. Chem. Soc.* **2020**, *142* (27), 11669–11673. https://doi.org/10.1021/jacs.0c04444.

(154) Zhou, S.; Li, J.; Lu, J.; Liu, H.; Kim, J.-Y.; Kim, A.; Yao, L.; Liu, C.; Qian, C.; Hood, Z. D.; Lin, X.; Chen, W.; Gage, T. E.; Arslan, I.; Travesset, A.; Sun, K.; Kotov, N. A.; Chen, Q. Chiral Assemblies of Pinwheel Superlattices on Substrates. *Nature* **2022**, *612* (7939), 259–265. https://doi.org/10.1038/s41586-022-05384-8.

(155) Liu, C.; Yao, L.; Chen, Q. Machine Learning Based Tracking of Single Nanoparticle Vibrations from a Projected 3D Moiré Lattice. *Microscopy and Microanalysis* **2022**, *28* (S1), 94–95. https://doi.org/10.1017/S1431927622001283.

(156) Zheng, H.; Claridge, S. A.; Minor, A. M.; Alivisatos, A. P.; Dahmen, U. Nanocrystal Diffusion in a Liquid Thin Film Observed by in Situ Transmission Electron Microscopy. *Nano Lett.* **2009**, *9* (6), 2460–2465. https://doi.org/10.1021/nl9012369.

(157) Miele, E.; Raj, S.; Baraissov, Z.; Král, P.; Mirsaidov, U. Dynamics of Templated Assembly of Nanoparticle Filaments within Nanochannels. *Advanced Materials* **2017**, *29* (37), 1702682. https://doi.org/10.1002/adma.201702682.

(158) Lin, G.; Chee, S. W.; Raj, S.; Král, P.; Mirsaidov, U. Linker-Mediated Self-Assembly Dynamics of Charged Nanoparticles. *ACS Nano* **2016**, *10* (8), 7443–7450. https://doi.org/10.1021/acsnano.6b01721.

(159) Powers, A. S.; Liao, H.-G.; Raja, S. N.; Bronstein, N. D.; Alivisatos, A. P.; Zheng, H. Tracking Nanoparticle Diffusion and Interaction during Self-Assembly in a Liquid Cell. *Nano Lett.* **2017**, *17* (1), 15–20. https://doi.org/10.1021/acs.nanolett.6b02972.

(160) White, E. R.; Mecklenburg, M.; Shevitski, B.; Singer, S. B.; Regan, B. C. Charged Nanoparticle Dynamics in Water Induced by Scanning Transmission Electron Microscopy. *Langmuir* **2012**, *28* (8), 3695–3698. https://doi.org/10.1021/la2048486.

(161) Chee, S. W.; Baraissov, Z.; Loh, N. D.; Matsudaira, P. T.; Mirsaidov, U. Desorption-Mediated Motion of Nanoparticles at the Liquid–Solid Interface. *J. Phys. Chem. C* **2016**, *120* (36), 20462–20470. https://doi.org/10.1021/acs.jpcc.6b07983.

(162) Verch, A.; Pfaff, M.; de Jonge, N. Exceptionally Slow Movement of Gold Nanoparticles at a Solid/Liquid Interface Investigated by Scanning Transmission Electron Microscopy. *Langmuir* **2015**, *31* (25), 6956–6964. https://doi.org/10.1021/acs.langmuir.5b00150.

(163) Tian, X.; Zheng, H.; Mirsaidov, U. Aggregation Dynamics of Nanoparticles at Solid–Liquid Interfaces. *Nanoscale* **2017**, *9* (28), 10044–10050. https://doi.org/10.1039/C7NR01985H.

(164) Yesibolati, M. N.; Mortensen, K. I.; Sun, H.; Brostrøm, A.; Tidemand-Lichtenberg, S.; Mølhave, K. Unhindered Brownian Motion of Individual Nanoparticles in Liquid-Phase Scanning Transmission Electron Microscopy. *Nano Lett.* **2020**, *20* (10), 7108–7115. https://doi.org/10.1021/acs.nanolett.0c02352.

(165) Schneider, N. M.; Norton, M. M.; Mendel, B. J.; Grogan, J. M.; Ross, F. M.; Bau, H. H. Electron–Water Interactions and Implications for Liquid Cell Electron Microscopy. *J. Phys. Chem. C* **2014**, *118* (38), 22373–22382. https://doi.org/10.1021/jp507400n.

(166) Woehl, T. j.; Abellan, P. Defining the radiation chemistry during liquid cell electron microscopy to enable visualization of nanomaterial growth and degradation dynamics. *Journal of Microscopy* **2017**, *265* (2), 135–147. https://doi.org/10.1111/jmi.12508.

(167) Wang, M.; Leff, A. C.; Li, Y.; Woehl, T. J. Visualizing Ligand-Mediated Bimetallic Nanocrystal Formation Pathways with in Situ Liquid-Phase Transmission Electron Microscopy Synthesis. *ACS Nano* **2021**, *15* (2), 2578–2588. https://doi.org/10.1021/acsnano.0c07131.

(168) Matusiak, M.; Kadlubowski, S.; Rosiak, J. M. Nanogels Synthesized by Radiation-Induced Intramolecular Crosslinking of Water-Soluble Polymers. *Radiation Physics and Chemistry* **2020**, *169*, 108099. https://doi.org/10.1016/j.radphyschem.2018.12.019.

(169) Woehl, T. J.; Moser, T.; Evans, J. E.; Ross, F. M. Electron-Beam-Driven Chemical Processes during Liquid Phase Transmission Electron Microscopy. *MRS Bulletin* **2020**, *45* (9), 746–753. https://doi.org/10.1557/mrs.2020.227.

(170) Nagamanasa, K. H.; Wang, H.; Granick, S. Liquid-Cell Electron Microscopy of Adsorbed Polymers. *Advanced Materials* **2017**, *29* (41), 1703555. https://doi.org/10.1002/adma.201703555.

(171) Carlier, M.-F.; Pernier, J.; Montaville, P.; Shekhar, S.; Kühn, S. Control of Polarized Assembly of Actin Filaments in Cell Motility. *Cell Mol Life Sci* **2015**, *72* (16), 3051–3067. https://doi.org/10.1007/s00018-015-1914-2.

(172) Engelborghs, Y. Microtubules: Dissipative Structures Formed by Self-Assembly. *Biosensors and Bioelectronics* **1994**, *9* (9), 685–689. https://doi.org/10.1016/0956-5663(94)80066-9.

(173) Hess, H.; Ross, J. L. Non-Equilibrium Assembly of Microtubules: From Molecules to Autonomous Chemical Robots. *Chem Soc Rev* **2017**, *46* (18), 5570–5587. https://doi.org/10.1039/c7cs00030h.

(174) Ragazzon, G.; Prins, L. J. Energy Consumption in Chemical Fuel-Driven Self-Assembly. *Nature Nanotech* **2018**, *13* (10), 882–889. https://doi.org/10.1038/s41565-018-0250-8.

(175) Debnath, S.; Roy, S.; Ulijn, R. V. Peptide Nanofibers with Dynamic Instability through Nonequilibrium Biocatalytic Assembly. *J. Am. Chem. Soc.* **2013**, *135* (45), 16789–16792. https://doi.org/10.1021/ja4086353.

(176) Rajawasam, C. W. H.; Tran, C.; Weeks, M.; McCoy, K. S.; Ross-Shannon, R.; Dodo, O. J.; Sparks, J. L.; Hartley, C. S.; Konkolewicz, D. Chemically Fueled Reinforcement of Polymer Hydrogels. *J. Am. Chem. Soc.* **2023**, *145* (9), 5553–5560. https://doi.org/10.1021/jacs.3c00668.

(177) Deng, J.; Liu, W.; Sun, M.; Walther, A. Dissipative Organization of DNA Oligomers for Transient Catalytic Function. *Angewandte Chemie* **2022**, *134* (10), e202113477. https://doi.org/10.1002/ange.202113477.

(178) Zhou, Z.; Ouyang, Y.; Wang, J.; Willner, I. Dissipative Gated and Cascaded DNA Networks. *J. Am. Chem. Soc.* **2021**, *143* (13), 5071–5079. https://doi.org/10.1021/jacs.1c00486.

(179) J. Post, E. A.; P. Fletcher, S. Dissipative Self-Assembly, Competition and Inhibition in a Self-Reproducing Protocell Model. *Chemical Science* **2020**, *11* (35), 9434–9442. https://doi.org/10.1039/D0SC02768E.

(180) Wanzke, C.; Jussupow, A.; Kohler, F.; Dietz, H.; Kaila, V. R. I.; Boekhoven, J. Dynamic Vesicles Formed By Dissipative Self-Assembly. *ChemSystemsChem* **2020**, *2* (1), e1900044. https://doi.org/10.1002/syst.201900044.

(181) Sorrenti, A.; Leira-Iglesias, J.; Sato, A.; Hermans, T. M. Non-Equilibrium Steady States in Supramolecular Polymerization. *Nat Commun* **2017**, *8* (1), 15899. https://doi.org/10.1038/ncomms15899.

(182) Singh, N.; Formon, G. J. M.; De Piccoli, S.; Hermans, T. M. Devising Synthetic Reaction Cycles for Dissipative Nonequilibrium Self-Assembly. *Advanced Materials* **2020**, *32* (20), 1906834. https://doi.org/10.1002/adma.201906834.

(183) Roy, S.; Gravener, L.; Philp, D.; Kay, E. A Dissipative Reaction Network Drives Transient Solid-Liquid and Liquid-Liquid Phase Cycling of Nanoparticles. *Angewandte Chemie International Edition* **2023**, *n/a* (n/a), e202217613. https://doi.org/10.1002/anie.202217613.

(184) Ogden, W. A.; Guan, Z. Redox Chemical-Fueled Dissipative Self-Assembly of Active Materials. *ChemSystemsChem* **2020**, *2* (4), e1900030. https://doi.org/10.1002/syst.201900030.

(185) Li, Q.; Jonas, U.; Zhao, X. S.; Kappl, M. The forces at work in colloidal self-assembly: a review on fundamental interactions between colloidal particles. *Asia-Pacific Journal of Chemical Engineering* **2008**, *3* (3), 255–268. https://doi.org/10.1002/apj.144.

(186) Rieß, B.; Wanzke, C.; Tena-Solsona, M.; K. Grötsch, R.; Maity, C.; Boekhoven, J. Dissipative Assemblies That Inhibit Their Deactivation. *Soft Matter* **2018**, *14* (23), 4852–4859. https://doi.org/10.1039/C8SM00822A.

(187) Macfarlane, R. J.; Lee, B.; Jones, M. R.; Harris, N.; Schatz, G. C.; Mirkin, C. A. Nanoparticle Superlattice Engineering with DNA. *Science* **2011**, *334* (6053), 204–208. https://doi.org/10.1126/science.1210493.

(188) He, M.; Gales, J. P.; Ducrot, É.; Gong, Z.; Yi, G.-R.; Sacanna, S.; Pine, D. J. Colloidal Diamond. *Nature* **2020**, *585* (7826), 524–529. https://doi.org/10.1038/s41586-020-2718-6.

(189) Toso, S.; Baranov, D.; Altamura, D.; Scattarella, F.; Dahl, J.; Wang, X.; Marras, S.; Alivisatos, A. P.; Singer, A.; Giannini, C.; Manna, L. Multilayer Diffraction Reveals

That Colloidal Superlattices Approach the Structural Perfection of Single Crystals. *ACS Nano* **2021**, *15* (4), 6243–6256. https://doi.org/10.1021/acsnano.0c08929.

(190) Swinkels, P. J. M.; Stuij, S. G.; Gong, Z.; Jonas, H.; Ruffino, N.; Linden, B. van der; Bolhuis, P. G.; Sacanna, S.; Woutersen, S.; Schall, P. Revealing Pseudorotation and Ring-Opening Reactions in Colloidal Organic Molecules. *Nat Commun* **2021**, *12* (1), 2810. https://doi.org/10.1038/s41467-021-23144-6.

(191) Kim, Y.-J.; Kim, J.-H.; Jo, I.-S.; Pine, D. J.; Sacanna, S.; Yi, G.-R. Patchy Colloidal Clusters with Broken Symmetry. *J. Am. Chem. Soc.* **2021**, *143* (33), 13175–13183. https://doi.org/10.1021/jacs.1c05123.

(192) Ma, F.; Wu, D. T.; Wu, N. Formation of Colloidal Molecules Induced by Alternating-Current Electric Fields. *J. Am. Chem. Soc.* **2013**, *135* (21), 7839–7842. https://doi.org/10.1021/ja403172p.

(193) McMullen, A.; Hilgenfeldt, S.; Brujic, J. DNA Self-Organization Controls Valence in Programmable Colloid Design. *Proceedings of the National Academy of Sciences* **2021**, *118* (46), e2112604118. https://doi.org/10.1073/pnas.2112604118.

(194) Del Grosso, E.; Amodio, A.; Ragazzon, G.; Prins, L. J.; Ricci, F. Dissipative Synthetic DNA-Based Receptors for the Transient Loading and Release of Molecular Cargo. *Angewandte Chemie International Edition* **2018**, *57* (33), 10489–10493. https://doi.org/10.1002/anie.201801318.

(195) Moisy, F. Boxcount, 2023. https://www.mathworks.com/matlabcentral/fileexchange/13063-boxcount (accessed 2023-09-07).

(196) Lin, M. Y.; Lindsay, H. M.; Weitz, D. A.; Ball, R. C.; Klein, R.; Meakin, P. Universality in Colloid Aggregation. *Nature* **1989**, *339* (6223), 360–362. https://doi.org/10.1038/339360a0.

(197) Tenti, J. M.; Hernández Guiance, S. N.; Irurzun, I. M. Fractal Dimension of Diffusion-Limited Aggregation Clusters Grown on Spherical Surfaces. *Phys. Rev. E* **2021**, *103* (1), 012138. https://doi.org/10.1103/PhysRevE.103.012138.

(198) Satzer, P.; Burgstaller, D.; Krepper, W.; Jungbauer, A. Fractal Dimension of Antibody-PEG Precipitate: Light Microscopy for the Reconstruction of 3D Precipitate Structures. *Engineering in Life Sciences* **2020**, *20* (3–4), 67–78. https://doi.org/10.1002/elsc.201900110.

(199) McMullen, A.; Holmes-Cerfon, M.; Sciortino, F.; Grosberg, A. Y.; Brujic, J. Freely Jointed Polymers Made of Droplets. *Phys. Rev. Lett.* **2018**, *121* (13), 138002. https://doi.org/10.1103/PhysRevLett.121.138002.

(200) van Ravensteijn, B. G. P.; Hendriksen, W. E.; Eelkema, R.; van Esch, J. H.; Kegel, W. K. Fuel-Mediated Transient Clustering of Colloidal Building Blocks. *J. Am. Chem. Soc.* **2017**, *139* (29), 9763–9766. https://doi.org/10.1021/jacs.7b03263.

(201) Semisotnov, G. V.; Rodionova, N. A.; Razgulyaev, O. I.; Uversky, V. N.; Gripas', A. F.; Gilmanshin, R. I. Study of the "Molten Globule" Intermediate State in Protein Folding by a Hydrophobic Fluorescent Probe. *Biopolymers* **1991**, *31* (1), 119–128. https://doi.org/10.1002/bip.360310111.

(202) Taylor, I. A.; Kneale, G. G. A Competition Assay for DNA Binding Using the Fluorescent Probe ANS. *DNA-Protein Interactions* **2001**, 265–274. https://doi.org/10.1385/1-59259-208-2:265.

(203) Schönbrunn, E.; Eschenburg, S.; Luger, K.; Kabsch, W.; Amrhein, N. Structural Basis for the Interaction of the Fluorescence Probe 8-Anilino-1-Naphthalene Sulfonate (ANS) with the Antibiotic Target MurA. *Proceedings of the National Academy of Sciences* **2000**, *97* (12), 6345–6349. https://doi.org/10.1073/pnas.120120397.

(204) Zhang, X.; Dong, Y.; Yu, J.; Tu, X. Effects of Environmental Factors on MSP21–25 Aggregation Indicate the Roles of Hydrophobic and Electrostatic Interactions in the Aggregation Process. *Eur Biophys J* **2014**, *43* (1), 1–9. https://doi.org/10.1007/s00249-013-0934-9.

(205) Halets-Bui, I.; Dzmitruk, V.; Abashkin, V.; Loznikova, S.; Acet, Ö.; Önal, B.; Özdemir, N.; Bryszewska, M.; Odabaşı, M.; Shcharbin, D. Differences between Cu- and Fe–Cu Nanoflowers in Their Interactions with Fluorescent Probes ANS and Fura-2 and Proteins Albumin and Thrombin. *Polym. Bull.* **2022**, *79* (7), 5247–5259. https://doi.org/10.1007/s00289-021-03773-z.

(206) Matulis, D.; Baumann, C. G.; Bloomfield, V. A.; Lovrien, R. E. 1-Anilino-8-Naphthalene Sulfonate as a Protein Conformational Tightening Agent. *Biopolymers* **1999**, *49* (6), 451–458. https://doi.org/10.1002/(SICI)1097-0282(199905)49:6<451::AID-BIP3>3.0.CO;2-6.

(207) Robinson, G. W.; Robbins, R. J.; Fleming, G. R.; Morris, J. M.; Knight, A. E. W.; Morrison, R. J. S. Picosecond Studies of the Fluorescence Probe Molecule 8-Anilino-1-Naphthalenesulfonic Acid. *J. Am. Chem. Soc.* **1978**, *100* (23), 7145–7150. https://doi.org/10.1021/ja00491a003.

(208) Kobayashi, M.; Juillerat, F.; Galletto, P.; Bowen, P.; Borkovec, M. Aggregation and Charging of Colloidal Silica Particles: Effect of Particle Size. *Langmuir* **2005**, *21* (13), 5761–5769. https://doi.org/10.1021/la046829z.

(209) Yotsumoto, H.; Yoon, R.-H. Application of Extended DLVO Theory: II. Stability of Silica Suspensions. *Journal of Colloid and Interface Science* **1993**, *157* (2), 434–441. https://doi.org/10.1006/jcis.1993.1206.

(210) Suresh, L.; Walz, J. Y. Effect of Surface Roughness on the Interaction Energy between a Colloidal Sphere and a Flat Plate. *Journal of Colloid and Interface Science* **1996**, *183* (1), 199–213. https://doi.org/10.1006/jcis.1996.0535.

(211) Salipante, P. F.; Hudson, S. D. Reversible Adsorption Kinetics of Near Surface Dimer Colloids. *Langmuir* **2016**, *32* (34), 8565–8573. https://doi.org/10.1021/acs.langmuir.6b02019.

(212) Han, K.; Shields IV, C. W.; Velev, O. D. Engineering of Self-Propelling Microbots and Microdevices Powered by Magnetic and Electric Fields. *Advanced Functional Materials* **2018**, *28* (25), 1705953. https://doi.org/10.1002/adfm.201705953.

(213) Shevchenko, E. V.; Talapin, D. V.; Kotov, N. A.; O'Brien, S.; Murray, C. B. Structural Diversity in Binary Nanoparticle Superlattices. *Nature* **2006**, *439* (7072), 55–59. https://doi.org/10.1038/nature04414.

(214) Boles, M. A.; Engel, M.; Talapin, D. V. Self-Assembly of Colloidal Nanocrystals: From Intricate Structures to Functional Materials. *Chem. Rev.* **2016**, *116* (18), 11220–11289. https://doi.org/10.1021/acs.chemrev.6b00196.

(215) Cademartiri, L.; Bishop, K. J. M. Programmable Self-Assembly. *Nature Mater* **2015**, *14* (1), 2–9. https://doi.org/10.1038/nmat4184.

(216) Whitelam, S.; Jack, R. L. The Statistical Mechanics of Dynamic Pathways to Self-Assembly. *Annu. Rev. Phys. Chem.* **2015**, *66* (1), 143–163. https://doi.org/10.1146/annurev-physchem-040214-121215.

(217) Jungjohann, K. L.; Wheeler, D. R.; Polsky, R.; Brozik, S. M.; Brozik, J. A.; Rudolph, A. R. Liquid-Cell Scanning Transmission Electron Microscopy and Fluorescence Correlation Spectroscopy of DNA-Directed Gold Nanoparticle Assemblies. *Micron* **2019**, *119*, 54–63. https://doi.org/10.1016/j.micron.2018.11.004.

(218) Keskin, S.; Besztejan, S.; Kassier, G.; Manz, S.; Bücker, R.; Riekeberg, S.; Trieu, H. K.; Rentmeister, A.; Miller, R. J. D. Visualization of Multimerization and Self-Assembly of DNA-Functionalized Gold Nanoparticles Using In-Liquid Transmission Electron Microscopy. *J. Phys. Chem. Lett.* **2015**, *6* (22), 4487–4492. https://doi.org/10.1021/acs.jpclett.5b02075.

(219) Ou, Z.; Wang, Z.; Luo, B.; Luijten, E.; Chen, Q. Kinetic Pathways of Crystallization at the Nanoscale. *Nat. Mater.* **2020**, *19* (4), 450–455. https://doi.org/10.1038/s41563-019-0514-1.

(220) Tan, S. F.; Raj, S.; Bisht, G.; Annadata, H. V.; Nijhuis, C. A.; Král, P.; Mirsaidov, U. Nanoparticle Interactions Guided by Shape-Dependent Hydrophobic Forces. *Advanced Materials* **2018**, *30* (16), 1707077. https://doi.org/10.1002/adma.201707077.

(221) Cookman, J.; Hamilton, V.; Price, L. S.; Hall, S. R.; Bangert, U. Visualising Early-Stage Liquid Phase Organic Crystal Growth via Liquid Cell Electron Microscopy. *Nanoscale* **2020**, *12* (7), 4636–4644. https://doi.org/10.1039/C9NR08126G.

(222) Park, J. H.; Schneider, N. M.; Grogan, J. M.; Reuter, M. C.; Bau, H. H.; Kodambaka, S.; Ross, F. M. Control of Electron Beam-Induced Au Nanocrystal Growth Kinetics through Solution Chemistry. *Nano Lett.* **2015**, *15* (8), 5314–5320. https://doi.org/10.1021/acs.nanolett.5b01677.

(223) Francis, S.; Varshney, L.; Tirumalesh, K. Studies on Radiation Synthesis of Polyethyleneimine/Acrylamide Hydrogels. *Radiation Physics and Chemistry* **2006**, *75* (7), 747–754. https://doi.org/10.1016/j.radphyschem.2005.12.038.

(224) Garrison, W. M. Reaction Mechanisms in the Radiolysis of Peptides, Polypeptides, and Proteins. *Chem. Rev.* **1987**, *87* (2), 381–398. https://doi.org/10.1021/cr00078a006.

(225) SHADYRO, O. I.; SOSNOVSKAYA, A. A.; VRUBLEVSKAYA, O. N. C-N Bond Cleavage Reactions on the Radiolysis of Amino-Containing Organic Compounds and Their Derivatives in Aqueous Solutions. *International Journal of Radiation Biology* **2003**, *79* (4), 269–279. https://doi.org/10.1080/0955300031000085902.

(226) Roder, M.; Wojnárovits, L.; Földiák, G. Pulse Radiolysis of Aqueous Solutions of Aromatic Hydrocarbons in the Presence of Oxygen. *International Journal of Radiation Applications and Instrumentation. Part C. Radiation Physics and Chemistry* **1990**, *36* (2), 175–176. https://doi.org/10.1016/1359-0197(90)90236-B.

(227) Delaire, J. A.; Bazouin, J. R. Primary Mechanisms in the Radiolysis of Amines: Pulse and γ-Radiolysis of Neutral and Acidic Ethylamine, n-Propylamine and Ethylenediamine. *Can. J. Chem.* **1979**, *57* (15), 2013–2021. https://doi.org/10.1139/v79-323.

(228) Neta, P.; Simic, M.; Hayon, E. Pulse Radiolysis of Aliphatic Acids in Aqueous Solutions. I. Simple Monocarboxylic Acids. *J. Phys. Chem.* **1969**, *73* (12), 4207–4213. https://doi.org/10.1021/j100846a029.

(229) Ulanski, P.; Bothe, E.; Hildenbrand, K.; Rosiak, J. M.; von Sonntag, C. Radiolysis of Poly(Acrylic Acid) in Aqueous Solution. *Radiation Physics and Chemistry* **1995**, *46* (4, Part 1), 909–912. https://doi.org/10.1016/0969-806X(95)00290-E.

(230) Ulański, P.; Janik, I.; Rosiak, J. M. Radiation Formation of Polymeric Nanogels. *Radiation Physics and Chemistry* **1998**, *52* (1), 289–294. https://doi.org/10.1016/S0969-806X(98)00155-8.

(231) Ulański, P.; Kadłubowski, S.; Rosiak, J. M. Synthesis of Poly(Acrylic Acid) Nanogels by Preparative Pulse Radiolysis. *Radiation Physics and Chemistry* **2002**, *63* (3), 533–537. https://doi.org/10.1016/S0969-806X(01)00549-7.

(232) Ulański, P.; Zainuddin; Rosiak, J. M. Pulse Radiolysis of Poly(Ethylene Oxide) in Aqueous Solution. II. Decay of Macroradicals. *Radiation Physics and Chemistry* **1995**, *46* (4, Part 1), 917–920. https://doi.org/10.1016/0969-806X(95)00292-6.

(233) Hauwiller, M. R.; Ondry, J. C.; Chan, C. M.; Khandekar, P.; Yu, J.; Alivisatos, A. P. Gold Nanocrystal Etching as a Means of Probing the Dynamic Chemical Environment in Graphene Liquid Cell Electron Microscopy. *J. Am. Chem. Soc.* **2019**, *141* (10), 4428–4437. https://doi.org/10.1021/jacs.9b00082.

(234) Weiner, R. G.; Chen, D. P.; Unocic, R. R.; Skrabalak, S. E. Impact of Membrane-Induced Particle Immobilization on Seeded Growth Monitored by In Situ Liquid Scanning Transmission Electron Microscopy. *Small* **2016**, *12* (20), 2701–2706. https://doi.org/10.1002/smll.201502974.

(235) Woehl, T. J.; Evans, J. E.; Arslan, I.; Ristenpart, W. D.; Browning, N. D. Direct in Situ Determination of the Mechanisms Controlling Nanoparticle Nucleation and Growth. *ACS Nano* **2012**, *6* (10), 8599–8610. https://doi.org/10.1021/nn303371y.

(236) Wu, J.; Gao, W.; Yang, H.; Zuo, J.-M. Dissolution Kinetics of Oxidative Etching of Cubic and Icosahedral Platinum Nanoparticles Revealed by in Situ Liquid Transmission Electron Microscopy. *ACS Nano* **2017**, *11* (2), 1696–1703. https://doi.org/10.1021/acsnano.6b07541.

(237) Ye, X.; Jones, M. R.; Frechette, L. B.; Chen, Q.; Powers, A. S.; Ercius, P.; Dunn, G.; Rotskoff, G. M.; Nguyen, S. C.; Adiga, V. P.; Zettl, A.; Rabani, E.; Geissler, P. L.; Alivisatos, A. P. Single-Particle Mapping of Nonequilibrium Nanocrystal Transformations. *Science* **2016**, *354* (6314), 874–877. https://doi.org/10.1126/science.aah4434.

(238) Zečević, J.; Hermannsdörfer, J.; Schuh, T.; de Jong, K. P.; de Jonge, N. Anisotropic Shape Changes of Silica Nanoparticles Induced in Liquid with Scanning Transmission Electron Microscopy. *Small* **2017**, *13* (1), 1602466. https://doi.org/10.1002/smll.201602466.

(239) Patterson, J. P.; Abellan, P.; Denny, M. S. Jr.; Park, C.; Browning, N. D.; Cohen, S. M.; Evans, J. E.; Gianneschi, N. C. Observing the Growth of Metal–Organic Frameworks by in Situ Liquid Cell Transmission Electron Microscopy. *J. Am. Chem. Soc.* **2015**, *137* (23), 7322–7328. https://doi.org/10.1021/jacs.5b00817.

(240) Elgrabli, D.; Dachraoui, W.; Ménard-Moyon, C.; Liu, X. J.; Bégin, D.; Bégin-Colin, S.; Bianco, A.; Gazeau, F.; Alloyeau, D. Carbon Nanotube Degradation in Macrophages: Live Nanoscale Monitoring and Understanding of Biological Pathway. *ACS Nano* **2015**, *9* (10), 10113–10124. https://doi.org/10.1021/acsnano.5b03708.

(241) Woehl, T. J.; Kashyap, S.; Firlar, E.; Perez-Gonzalez, T.; Faivre, D.; Trubitsyn, D.; Bazylinski, D. A.; Prozorov, T. Correlative Electron and Fluorescence Microscopy of Magnetotactic Bacteria in Liquid: Toward In Vivo Imaging. *Microscopy and*

Microanalysis **2015**, *21* (S3), 1499–1500. https://doi.org/10.1017/S1431927615008272.

(242) Korpanty, J.; Parent, L. R.; Gianneschi, N. C. Enhancing and Mitigating Radiolytic Damage to Soft Matter in Aqueous Phase Liquid-Cell Transmission Electron Microscopy in the Presence of Gold Nanoparticle Sensitizers or Isopropanol Scavengers. *Nano Lett.* **2021**, *21* (2), 1141–1149. https://doi.org/10.1021/acs.nanolett.0c04636.

(243) Schneider, C. A.; Rasband, W. S.; Eliceiri, K. W. NIH Image to ImageJ: 25 Years of Image Analysis. *Nat Methods* **2012**, *9* (7), 671–675. https://doi.org/10.1038/nmeth.2089.

(244) Wu, H.; Friedrich, H.; Patterson, J. P.; Sommerdijk, N. A. J. M.; de Jonge, N. Liquid-Phase Electron Microscopy for Soft Matter Science and Biology. *Advanced Materials* **2020**, *32* (25), 2001582. https://doi.org/10.1002/adma.202001582.

(245) Woehl, T. J.; Kashyap, S.; Firlar, E.; Perez-Gonzalez, T.; Faivre, D.; Trubitsyn, D.; Bazylinski, D. A.; Prozorov, T. Correlative Electron and Fluorescence Microscopy of Magnetotactic Bacteria in Liquid: Toward In Vivo Imaging. *Sci Rep* **2014**, *4* (1), 6854. https://doi.org/10.1038/srep06854.

(246) Cho, H.; Jones, M. R.; Nguyen, S. C.; Hauwiller, M. R.; Zettl, A.; Alivisatos, A. P. The Use of Graphene and Its Derivatives for Liquid-Phase Transmission Electron Microscopy of Radiation-Sensitive Specimens. *Nano Lett.* **2017**, *17* (1), 414–420. https://doi.org/10.1021/acs.nanolett.6b04383.

(247) Chapiro, A. Radiation Induced Polymerization. *Radiation Physics and Chemistry (1977)* **1979**, *14* (1), 101–116. https://doi.org/10.1016/0146-5724(79)90015-3.

(248) Cleland, M. R.; Parks, L. A.; Cheng, S. Applications for Radiation Processing of Materials. *Nuclear Instruments and Methods in Physics Research Section B: Beam Interactions with Materials and Atoms* **2003**, *208*, 66–73. https://doi.org/10.1016/S0168-583X(03)00655-4.

(249) Gibson, W.; Patterson, J. P. Liquid Phase Electron Microscopy Provides Opportunities in Polymer Synthesis and Manufacturing. *Macromolecules* **2021**, *54* (11), 4986–4996. https://doi.org/10.1021/acs.macromol.0c02710.

(250) Jiang, N. Note on in Situ (Scanning) Transmission Electron Microscopy Study of Liquid Samples. *Ultramicroscopy* **2017**, *179*, 81–83. https://doi.org/10.1016/j.ultramic.2017.04.012.

(251) Mehdi, B. L.; Stevens, A.; Kovarik, L.; Jiang, N.; Mehta, H.; Liyu, A.; Reehl, S.; Stanfill, B.; Luzi, L.; Hao, W.; Bramer, L.; Browning, N. D. Controlling the Spatio-Temporal Dose Distribution during STEM Imaging by Subsampled Acquisition: In-Situ Observations of Kinetic Processes in Liquids. *Appl. Phys. Lett.* **2019**, *115* (6), 063102. https://doi.org/10.1063/1.5096595.

(252) Gupta, T.; Schneider, N. M.; Park, J. H.; Steingart, D.; Ross, F. M. Spatially Dependent Dose Rate in Liquid Cell Transmission Electron Microscopy. *Nanoscale* **2018**, *10* (16), 7702–7710. https://doi.org/10.1039/C8NR01935E.

(253) Ulanski, P.; Bothe, E.; Hildenbrand, K.; von Sonntag, C. Free-Radical-Induced Chain Breakage and Depolymerization of Poly(Methacrylic Acid): Equilibrium Polymerization in Aqueous Solution at Room Temperature. *Chemistry – A European Journal* **2000**, *6* (21), 3922–3934. https://doi.org/10.1002/1521-3765(20001103)6:21<3922::AID-CHEM3922>3.0.CO;2-2.

(254) Ulanski, P.; Sonntag, C. von. OH-Radical-Induced Chain Scission of Chitosan in the Absence and Presence of Dioxygen. *J. Chem. Soc., Perkin Trans. 2* **2000**, No. 10, 2022–2028. https://doi.org/10.1039/B003952G.

(255) Gröllmann, U.; Schnabel, W. On the Kinetics of Polymer Degradation in Solution, 9. Pulse Radiolysis of Poly(Ethylene Oxide). *Die Makromolekulare Chemie* **1980**, *181* (6), 1215–1226. https://doi.org/10.1002/macp.1980.021810606.

(256) Gröllmann, U.; Schnabel, W. Free Radical-Induced Oxidative Degradation of Polyacrylamide in Aqueous Solution. *Polymer Degradation and Stability* **1982**, *4* (3), 203–212. https://doi.org/10.1016/0141-3910(82)90027-1.

(257) Shahmoon, A.; Limon, O.; Girshevitz, O.; Zalevsky, Z. Self Assembly of Nano Metric Metallic Particles for Realization of Photonic and Electronic Nano Transistors. *International Journal of Molecular Sciences* **2010**, *11* (5), 2241–2252. https://doi.org/10.3390/ijms11052242.

(258) Korotkov, A. N. Wireless Single-electron Logic Biased by Alternating Electric Field. *Applied Physics Letters* **1995**, *67* (16), 2412–2414. https://doi.org/10.1063/1.114564.

(259) Herbert, R.; Mishra, S.; Lim, H.-R.; Yoo, H.; Yeo, W.-H. Fully Printed, Wireless, Stretchable Implantable Biosystem toward Batteryless, Real-Time Monitoring of Cerebral Aneurysm Hemodynamics. *Advanced Science* **2019**, *6* (18), 1901034. https://doi.org/10.1002/advs.201901034.

(260) Chen, T.; Wang, Y.; Yang, Y.; Huang, F.; Zhu, M.; Ang, B. T. W.; Xue, J. M. Heterometallic Seed-Mediated Zinc Deposition on Inkjet Printed Silver Nanoparticles Toward Foldable and Heat-Resistant Zinc Batteries. *Advanced Functional Materials* **2021**, *31* (24), 2101607. https://doi.org/10.1002/adfm.202101607.

(261) Shahmoon, A.; Limon, O.; Girshevitz, O.; Fleger, Y.; Demir, H. V.; Zalevsky, Z. Tunable Nano Devices Fabricated by Controlled Deposition of Gold Nanoparticles via Focused Ion Beam. *Microelectronic Engineering* **2010**, *87* (5), 1363–1366. https://doi.org/10.1016/j.mee.2009.12.031.

(262) Yoshida, T.; Yamada, Y.; Orii, T. Electroluminescence of Silicon Nanocrystallites Prepared by Pulsed Laser Ablation in Reduced Pressure Inert Gas. *Journal of Applied Physics* **1998**, *83* (10), 5427–5432. https://doi.org/10.1063/1.367373.

(263) Raj, C. R.; Okajima, T.; Ohsaka, T. Gold Nanoparticle Arrays for the Voltammetric Sensing of Dopamine. *Journal of Electroanalytical Chemistry* **2003**, *543* (2), 127–133. https://doi.org/10.1016/S0022-0728(02)01481-X.

(264) Segev-Bar, M.; Landman, A.; Nir-Shapira, M.; Shuster, G.; Haick, H. Tunable Touch Sensor and Combined Sensing Platform: Toward Nanoparticle-Based Electronic Skin. *ACS Appl. Mater. Interfaces* **2013**, *5* (12), 5531–5541. https://doi.org/10.1021/am400757q.

(265) Wohltjen, H.; Snow, A. W. Colloidal Metal−Insulator−Metal Ensemble Chemiresistor Sensor. *Anal. Chem.* **1998**, *70* (14), 2856–2859. https://doi.org/10.1021/ac9713464.

(266) Liang, J.; Tian, B.; Li, S.; Jiang, C.; Wu, W. All-Printed MnHCF-MnOx-Based High-Performance Flexible Supercapacitors. *Advanced Energy Materials* **2020**, *10* (12), 2000022. https://doi.org/10.1002/aenm.202000022.

(267) Taguchi, T.; Isozaki, K.; Miki, K. Enhanced Catalytic Activity of Self-Assembled-Monolayer-Capped Gold Nanoparticles. *Advanced Materials* **2012**, *24* (48), 6462–6467. https://doi.org/10.1002/adma.201202979.

(268) Mi Kim, S.; Ho Mun, J.; Woo Lee, S.; An, H.; You Kim, H.; Ouk Kim, S.; Young Park, J. Compositional Effect of Two-Dimensional Monodisperse AuPd Bimetallic Nanoparticle Arrays Fabricated by Block Copolymer Nanopatterning on Catalytic Activity of CO Oxidation. *Chemical Communications* **2018**, *54* (97), 13734–13737. https://doi.org/10.1039/C8CC07963C.

(269) Shah, P. s.; Sigman Jr., M. b.; Stowell, C. a.; Lim, K. t.; Johnston, K. p.; Korgel, B. a. Single-Step Self-Organization of Ordered Macroporous Nanocrystal Thin Films. *Advanced Materials* **2003**, *15* (12), 971–974. https://doi.org/10.1002/adma.200304903.

(270) Pumera, M.; Wang, J.; Grushka, E.; Polsky, R. Gold Nanoparticle-Enhanced Microchip Capillary Electrophoresis. *Anal. Chem.* **2001**, *73* (22), 5625–5628. https://doi.org/10.1021/ac015589e.

(271) Checco, A.; Rahman, A.; Black, C. T. Robust Superhydrophobicity in Large-Area Nanostructured Surfaces Defined by Block-Copolymer Self Assembly. *Advanced Materials* **2014**, *26* (6), 886–891. https://doi.org/10.1002/adma.201304006.

(272) Zafri, H.; Azougi, J.; Girshevitz, O.; Zalevsky, Z.; Zitoun, D. Electron Beam Patterning for Writing of Positively Charged Gold Colloidal Nanoparticles. *J Nanopart Res* **2018**, *20* (2), 34. https://doi.org/10.1007/s11051-018-4129-2.

(273) Griffith, S.; Mondol, M.; Kong, D. S.; Jacobson, J. M. Nanostructure Fabrication by Direct Electron-Beam Writing of Nanoparticles. *Journal of Vacuum Science & Technology B: Microelectronics and Nanometer Structures Processing, Measurement, and Phenomena* **2002**, *20* (6), 2768–2772. https://doi.org/10.1116/1.1526697.

(274) Kong, D. S.; Varsanik, J. S.; Griffith, S.; Jacobson, J. M. Conductive Nanostructure Fabrication by Focused Ion Beam Direct-Writing of Silver Nanoparticles. *Journal of Vacuum Science & Technology B: Microelectronics and Nanometer Structures Processing, Measurement, and Phenomena* **2004**, *22* (6), 2987–2991. https://doi.org/10.1116/1.1825015.

(275) Rosa, L.; Sun, K.; Szymanska, J.; Hudson, F. E.; Dzurak, A.; Linden, A.; Bauerdick, S.; Peto, L.; Juodkazis, S. Tailoring Spectral Position and Width of Field Enhancement by Focused Ion-Beam Patterning of Plasmonic Nanoparticles. *physica status solidi (RRL) – Rapid Research Letters* **2010**, *4* (10), 262–264. https://doi.org/10.1002/pssr.201004239.

(276) Seniutinas, G.; Balčytis, A.; Nishijima, Y.; Nadzeyka, A.; Bauerdick, S.; Juodkazis, S. Ion Beam Lithography with Gold and Silicon Ions. *Appl. Phys. A* **2016**, *122* (4), 383. https://doi.org/10.1007/s00339-016-9866-4.

(277) Salaita, K.; Wang, Y.; Mirkin, C. A. Applications of Dip-Pen Nanolithography. *Nature Nanotech* **2007**, *2* (3), 145–155. https://doi.org/10.1038/nnano.2007.39.

(278) Liu, G.; Hirtz, M.; Fuchs, H.; Zheng, Z. Development of Dip-Pen Nanolithography (DPN) and Its Derivatives. *Small* **2019**, *15* (21), 1900564. https://doi.org/10.1002/smll.201900564.

(279) Barad, H.-N.; Kwon, H.; Alarcón-Correa, M.; Fischer, P. Large Area Patterning of Nanoparticles and Nanostructures: Current Status and Future Prospects. *ACS Nano* **2021**, *15* (4), 5861–5875. https://doi.org/10.1021/acsnano.0c09999.

(280) Hummel, M. E. J.; Stelling, C.; Kopera, B. A. F.; Nutz, F. A.; Karg, M.; Retsch, M.; Förster, S. Ordered Particle Arrays via a Langmuir Transfer Process: Access to Any Two-Dimensional Bravais Lattice. *Langmuir* **2019**, *35* (4), 973–979. https://doi.org/10.1021/acs.langmuir.8b03047.

(281) Stannard, A. Dewetting-Mediated Pattern Formation in Nanoparticle Assemblies. *J. Phys.: Condens. Matter* **2011**, *23* (8), 083001. https://doi.org/10.1088/0953-8984/23/8/083001.

(282) Kim, H. S.; Lee, C. H.; Sudeep, P. K.; Emrick, T.; Crosby, A. J. Nanoparticle Stripes, Grids, and Ribbons Produced by Flow Coating. *Advanced Materials* **2010**, *22* (41), 4600–4604. https://doi.org/10.1002/adma.201001892.

(283) Kwon, S.; Kim, W.; Kim, H.; Choi, S.; Park, B.-C.; Kang, S.-H.; Choi, K. C. High Luminance Fiber-Based Polymer Light-Emitting Devices by a Dip-Coating Method.

Advanced Electronic Materials **2015**, *1* (9), 1500103. https://doi.org/10.1002/aelm.201500103.

(284) Glass, R.; Möller, M.; Spatz, J. P. Block Copolymer Micelle Nanolithography. *Nanotechnology* **2003**, *14* (10), 1153. https://doi.org/10.1088/0957-4484/14/10/314.

(285) Bánsági, T.; Vanag, V. K.; Epstein, I. R. Tomography of Reaction-Diffusion Microemulsions Reveals Three-Dimensional Turing Patterns. *Science* **2011**, *331* (6022), 1309–1312. https://doi.org/10.1126/science.1200815.

(286) Ouyang, Q.; Swinney, H. L. Transition from a Uniform State to Hexagonal and Striped Turing Patterns. *Nature* **1991**, *352* (6336), 610–612. https://doi.org/10.1038/352610a0.

(287) Bauer, F.; Czihal, S.; Bertmer, M.; Decker, U.; Naumov, S.; Wassersleben, S.; Enke, D. Water-Based Functionalization of Mesoporous Siliceous Materials, Part 1: Morphology and Stability of Grafted 3-Aminopropyltriethoxysilane. *Microporous and Mesoporous Materials* **2017**, *250*, 221–231. https://doi.org/10.1016/j.micromeso.2016.01.046.

(288) Zhu, M.; Lerum, M. Z.; Chen, W. How To Prepare Reproducible, Homogeneous, and Hydrolytically Stable Aminosilane-Derived Layers on Silica. *Langmuir* **2012**, *28* (1), 416–423. https://doi.org/10.1021/la203638g.

(289) Zante, G.; Bouniol, V.; Sene, S.; Rey, C.; Causse, J.; Larionova, J.; Guari, Y.; Deschanels, X.; Le Caër, S. Grafted Mesoporous Silicas for Radionuclide Uptake: Radiolytic Stability under Electron Irradiation. *Microporous and Mesoporous Materials* **2022**, *336*, 111851. https://doi.org/10.1016/j.micromeso.2022.111851.

(290) Dissanayake, T. U.; Wang, M.; Woehl, T. J. Revealing Reactions between the Electron Beam and Nanoparticle Capping Ligands with Correlative Fluorescence and Liquid-Phase Electron Microscopy. *ACS Appl. Mater. Interfaces* **2021**, *13* (31), 37553–37562. https://doi.org/10.1021/acsami.1c10957.

(291) Robertson, A. W.; Zhu, G.; Mehdi, B. L.; Jacobs, R. M. J.; De Yoreo, J.; Browning, N. D. Nanoparticle Immobilization for Controllable Experiments in Liquid-Cell Transmission Electron Microscopy. *ACS Appl. Mater. Interfaces* **2018**, *10* (26), 22801–22808. https://doi.org/10.1021/acsami.8b03688.

(292) Sypabekova, M.; Hagemann, A.; Rho, D.; Kim, S. Review: 3-Aminopropyltriethoxysilane (APTES) Deposition Methods on Oxide Surfaces in Solution and Vapor Phases for Biosensing Applications. *Biosensors* **2023**, *13* (1), 36. https://doi.org/10.3390/bios13010036.

(293) Otalvaro, J. O.; Avena, M.; Brigante, M. Adsorption of Organic Pollutants by Amine Functionalized Mesoporous Silica in Aqueous Solution. Effects of pH, Ionic Strength and Some Consequences of APTES Stability. *Journal of Environmental*

Chemical Engineering **2019**, *7* (5), 103325. https://doi.org/10.1016/j.jece.2019.103325.

(294) Konecny, R. Reactivity of Hydroxyl Radicals on Hydroxylated Quartz Surface. 1. Cluster Model Calculations. *J. Phys. Chem. B* **2001**, *105* (26), 6221–6226. https://doi.org/10.1021/jp010752v.

(295) Tanny, G. B.; Pierre, L. E. S. Radiolytic Scissioning in Polydimethylsiloxane Networks. *International Journal of Polymeric Materials* **1972**. https://doi.org/10.1080/00914037208075290.

(296) T, M. S.; Mondal, T. Radiation Curable Polysiloxane: Synthesis to Applications. *Soft Matter* **2021**, *17* (26), 6284–6297. https://doi.org/10.1039/D1SM00269D.

(297) Le Caër, S.; Brunet, F.; Chatelain, C.; Durand, D.; Dauvois, V.; Charpentier, T.; Ph. Renault, J. Modifications under Irradiation of a Self-Assembled Monolayer Grafted on a Nanoporous Silica Glass: A Solid-State NMR Characterization. *J. Phys. Chem. C* **2012**, *116* (7), 4748–4759. https://doi.org/10.1021/jp211639u.

(298) Landge, A. N.; Jordan, B. M.; Diego, X.; Müller, P. Pattern Formation Mechanisms of Self-Organizing Reaction-Diffusion Systems. *Developmental Biology* **2020**, *460* (1), 2–11. https://doi.org/10.1016/j.ydbio.2019.10.031.

(299) Gierer, A. Generation of Biological Patterns and Form: Some Physical, Mathematical, and Logical Aspects. *Progress in Biophysics and Molecular Biology* **1981**, *37*, 1–47. https://doi.org/10.1016/0079-6107(82)90019-0.

(300) Hiscock, T. W.; Megason, S. G. Orientation of Turing-like Patterns by Morphogen Gradients and Tissue Anisotropies. *Cell Syst* **2015**, *1* (6), 408–416. https://doi.org/10.1016/j.cels.2015.12.001.

(301) Tan, G.; Zhang, L.; Ning, C.; Liu, X.; Liao, J. Preparation and Characterization of APTES Films on Modification Titanium by SAMs. *Thin Solid Films* **2011**, *519* (15), 4997–5001. https://doi.org/10.1016/j.tsf.2011.01.068.

(302) Kim, J.; Seidler, P.; Wan, L. S.; Fill, C. Formation, Structure, and Reactivity of Amino-Terminated Organic Films on Silicon Substrates. *Journal of Colloid and Interface Science* **2009**, *329* (1), 114–119. https://doi.org/10.1016/j.jcis.2008.09.031.

(303) Pasternack, R. M.; Rivillon Amy, S.; Chabal, Y. J. Attachment of 3-(Aminopropyl)Triethoxysilane on Silicon Oxide Surfaces: Dependence on Solution Temperature. *Langmuir* **2008**, *24* (22), 12963–12971. https://doi.org/10.1021/la8024827.

(304) McCleskey, R. B.; Nordstrom, D. K.; Ryan, J. N. Comparison of Electrical Conductivity Calculation Methods for Natural Waters. *Limnology and Oceanography: Methods* **2012**, *10* (11), 952–967. https://doi.org/10.4319/lom.2012.10.952.

(305) Winkelmann, J. Diffusion Coefficient of 2-Amino-Ethanesulfonic Acid Potassium Salt in Water at Infinite Dilution. In *Diffusion in Gases, Liquids and Electrolytes*; Lechner, M. D., Ed.; Springer Berlin Heidelberg: Berlin, Heidelberg, 2018; pp 2025–2025. https://doi.org/10.1007/978-3-662-54089-3_1445.

(306) Prieve, D. C.; Russel, W. B. Simplified Predictions of Hamaker Constants from Lifshitz Theory. *Journal of Colloid and Interface Science* **1988**, *125* (1), 1–13. https://doi.org/10.1016/0021-9797(88)90048-3.

(307) Good, R. J.; Kotsidas, E. D. Contact Angles on Swollen Polymers: The Surface Energy of Crosslinked Polystyrene. *The Journal of Adhesion* **1979**, *10* (1), 17–24. https://doi.org/10.1080/00218467908544608.

Publications and Presentations

Publications

1. Dissanayake, T. U.; Hughes, J.; Woehl, T. J. Dynamic Surface Chemistry and Interparticle Interactions Mediating Chemically Fueled Dissipative Assembly of Colloids. *Journal of Colloid and Interface Science.* **2023**. *650*, 972–982.

2. Dissanayake, T. U.; Wang, M.; Woehl, T. J. Revealing Reactions between the Electron Beam and Nanoparticle Capping Ligands with Correlative Fluorescence and Liquid-Phase Electron Microscopy. *ACS Appl. Mater. Interfaces.* **2021**. *13* (31), 37553–37562.

3. Chen, A.; Dissanayake, T. U.; Sun, J.; Woehl, T. J. Unraveling Chemical Processes during Nanoparticle Synthesis with Liquid Phase Electron Microscopy and Correlative Techniques. Chem. Commun. **2023**. https://doi.org/10.1039/D3CC03723A.

4. Wong, N. A.; Uchida, N. V.; Dissanayake, T. U.; Patel, M.; Iqbal, M.; Woehl, T. J. Detection and Sizing of Submicron Particles in Biologics with Interferometric Scattering Microscopy. *Journal of Pharmaceutical Sciences.* **2020**. *109* (1), 881–890.

5. Wang, M.; Dissanayake, T. U.; Park, C.; Gaskell, K.; Woehl, T. J. Nanoscale Mapping of Nonuniform Heterogeneous Nucleation Kinetics Mediated by Surface Chemistry. *J. Am. Chem. Soc.* **2019**. *141* (34), 13516–13524. https://doi.org/10.1021/jacs.9b05225.

6. Little, J. M.; Sun, J.; Kamali, A.; Chen, A.; Leff, A. C.; Li, Y.; Borden, L. K.; Dissanayake, T. U.; Essumang, D.; Oseleononmen, B. O.; Liu, D.; Woehl, T. J.; Chen, P.-Y. Noble Metal Ion-Directed Assembly of 2D Materials for Heterostructured Catalysts and

Metallic Micro-Texturing. *Adv. Funct. Mat*. **2023**. 33 (30), 2215222. https://doi.org/10.1002/adfm.202215222.

7. Ding, M.; Li, S.; Guo, L.; Jing, L.; Gao, S.-P.; Yang, H.; Little, J. M.; Dissanayake, T. U.; Li, K.; Yang, J.; Guo, Y.-X.; Yang, H. Y.; Woehl, T. J.; Chen, P.-Y. Metal Ion-Induced Assembly of MXene Aerogels via Biomimetic Microtextures for Electromagnetic Interference Shielding, Capacitive Deionization, and Microsupercapacitors. *Adv. En. Mat*. **2021**. 11 (35), 2101494. https://doi.org/10.1002/aenm.202101494.

Presentations

Oral presentations

1. Gordon Research Conference – Liquid Phase Electron Microscopy, 10/2022

Title: Visualizing Chemical Reaction Driven Assembly of Nanoparticles into Surface Patterns in LPEM.

2. Gordon Research Seminar – Liquid Phase Electron Microscopy, 10/2022

Title: Revealing Electron Beam Induced Reactions in Nanoparticle Capping Ligands and Nanoparticle – Polymer Systems During Liquid Phase Electron Microscopy.

3. Microscopy and Microanalysis Conference, 08/2022

Title: Liquid Phase Transmission Electron Microscopy Visualization of Surface Pattern Formation during Chemical Reaction Driven Assembly of Nanoparticles.

4. 96th ACS Colloids and Surface Science Symposium, 07/2022

Title: Visualizing Dynamics of Polymerization Induced Assembly of Nanoparticles into Turing Patterns.

5. CISCEM – In-Situ and Correlative Electron Microscopy (Virtual), 09/2021

Title: Probing Electron Beam – Nanoparticle Capping Ligand Interactions During Liquid Phase Transmission Electron Microscopy Using a Correlative Fluorescence Microscopy Assay

6. Microscopy and Microanalysis Conference, 08/2021

Title: Investigating electron beam interactions with nanoparticle capping ligands using correlative liquid phase transmission electron microscopy and fluorescence microscopy.

7. 95th ACS Colloids and Surface Science Symposium, (Virtual), 07/2022

Title: Probing interparticle interactions during formation of transient aggregates by chemical fuels

8. Spring MRS Conference (Virtual), 04/2021

Title: Investigating Interparticle Interactions Mediating Fuel Driven Dissipative Self-Assembly of Colloids

9. Microscopy and Microanalysis Conference, 08/2019

Title: A Fluorescence Microscopy Assay for Assessing Beam Damage to Nanoparticle Capping Ligands During Liquid Cell Electron Microscopy.

Poster Presentations

1. Gordon Research Conference – Liquid Phase Electron Microscopy, 10/2022

Title: Visualizing Chemical Reaction Driven Assembly of Nanoparticles into Surface Patterns in LPEM

2. CHBE Department showcase, University of Maryland, College Park, 04/2022

Title: Visualizing Chemical Reaction Driven Assembly of Nanoparticles into Surface Patterns in LPEM